McKelvey School of Engineering Theses & Dissertations

McKelvey School of Engineering

6-20-2024

Epigenetic Regulation of Skeletal Development

Austin Bell-Hensley
Washington University – McKelvey School of Engineering

Follow this and additional works at: https://openscholarship.wustl.edu/eng_etds

WASHINGTON UNIVERSITY IN ST. LOUIS

McKelvey School of Engineering
Department of Biomedical Engineering

Dissertation Examination Committee:
Audrey McAlinden, Chair
Farshid Guilak, Co-Chair
Jianjun Guan
David Ornitz
Simon Tang
Michael Vahey

Epigenetic Regulation of Skeletal Development
by
Austin Bell-Hensley

A dissertation presented to
the McKelvey School of Engineering
of Washington University in
partial fulfillment of the
requirements for the degree
of Doctor of Philosophy

August 2024
St. Louis, Missouri

Table of Contents

List of Figures

List of Tables

List of Abbreviations

AML	Acute Myeloid Leukemia
AQP9	Aquaporin-9
CG	Chondrogenic
COLII	Type II Collagen, isoform "B" secreted by differentiated chondrocytes
COLIIA	Type II Collagen, isoform "A" secreted by chondroprogenitors
Conn.D	Connective Density
CPC	Cartilage Progenitor Cells
Ct.Th	Cortical Bone Thickness
DAF	Differential Adhesion to Fibronectin
DMEM/F12	Dulbecco's Modified Eagle Medium, Nutrient Mixture F-12
DNMT3A	DNA Methyltransferase 3A
DOS	DNMT3A Overgrowth Syndrome
DPBS	Dulbecco's Phosphate-Buffered Saline
Ec.BFR	Endocortical Bone Formation Rate
Ec.MAR	Endocortical Mineral Apposition Rate
Ec.MS/BS	Endocortical Mineralizing Surface per Bone Surface
ECM	Extracellular Matrix
FDR	False Discovery Rate
GAGE	Generally Applicable Gene Expression Gene-set Analysis
GEO	Gene Expression Omnibus
GO	Gene Ontology
H&E	Hematoxylin & Eosin

HEK	Human Embryonic Kidney
IHC	Immunohistochemistry
LV-138	Lentivirus encoding the pre-miR-138 sequence
LV-181	Lentivirus encoding the pre-miR-181a/b-1 sequence
LV-NS	Lentivirus encoding a non-silencing RNA sequence
μCT	Micro-computed Tomography
MACI	Matrix-induced Autologous Chondrocyte Implantation
MF	Microfracture
miR	MicroRNA
miRNA	MicroRNA
MMA	Methyl Methacrylate
MOI	Multiplicity of Infection
MSC	Mesenchymal Stem/Stromal Cell
MUT	Mutant
MV	Marrow Volume
NBF	Neutral Buffered Formalin
NSAID	Non-steroidal Anti-inflammatory Drug
nt	Nucleotide
NT	Non-transduced
OA	Osteoarthritis
Oc.N/BS	Osteoclast Number per Bone Surface
Oc.S/BS	Osteoclast Surface per Bone Surface
OGID	Overgrowth and Intellectual Disability
OS	Osteogenic

PCL	Poly (ε-Caprolactone)
PCNA	Proliferating Cell Nuclear Antigen
Pre-miR	Precursor MicroRNA
Pri-miR	Primary MicroRNA
POC	Primary Ossification Center
Ps.BFR	Periosteal Bone Formation Rate
Ps.MAR	Periosteal Mineral Apposition Rate
Ps.MS/BS	Periosteal Mineralizing Surface per Bone Surface
RISC	RNA-induced Silencing Complex
RNA-Seq	RNA-Sequencing
Saf-O	Safranin-O
SMI	Structure Model Index
SOC	Secondary Ossification Center
Tb.N	Trabecular Number
Tb.Sp	Trabecular Spacing
Tb.Th	Trabecular Thickness
TBRS	Tatton-Brown-Rahman Syndrome
TGF-β	Transforming Growth Factor β
TMD	Tissue Mineral Density
TRAP	Tartrate-resistant Acid Phosphatase
vBMD	Volumetric Bone Mineral Density
WT	Wild-type

<u>Acknowledgments</u>

My sincerest gratitude goes out to my dissertation mentor, Dr. Audrey McAlinden, who offered me a position in her lab, encouraged me to ask questions, and guided my growth as a scientist and a professional. I brought energy, emotions, and ideas to the lab and she was always willing to listen and help me figure out my experimental plan of attack. When I joined the lab, I set out to become better at carrying out cell and molecular biology experiments and improve my grant writing skills, and Dr. McAlinden was intentional about making sure I achieved those goals. I will be eternally grateful for the team of scientists I worked alongside in Audrey's lab – Victor, Jin, Lei, Hongjun, and Katie – who inspired and uplifted me throughout my dissertation journey. Audrey's network of collaborators welcomed me with open arms and created space for me to join their ongoing projects and to develop my own ideas for future directions. Dr. Farshid Guilak supported my early research endeavors and was willing to share his expertise at a moment's notice. Dr. Harrison Gabel and Dr. Diana Beard allowed me to expand their project and were always gracious about my experimental ambitions. Dr. Matthew Silva and Dr. Simon Tang welcomed me into their biomechanics lab meetings and journal clubs gave me access to their expertise and helped me come up with mechanical approaches for my own project. Dr. Stephanie Bryant and Laurel Stefani invited me into their lab space to forge a new collaboration from across the country. Crystal Idleburg, Samantha Coleman, and Michael Brodt patiently listened to my experimental ideas and made sure to share their technical expertise to complete my projects.

While the PhD degree will have my name on it, there are many people who have "earned" this degree and I would not be here without them. First, I would like to offer the utmost appreciation to my wife, Alexis, who uprooted her life to help me pursue my goal of earning a PhD and provided me with tireless support. Next, a heartfelt thank you to my family who prepared me for this step in my educational journey. Mom and Dad – thank you for teaching me to persevere and think independently from a young age. Graycen – thank you for always listening and for reminding me to enjoy every day. To all of my grandparents – the dream of completing a PhD would not have been possible without your hard work and sacrifices; it brings me a tremendous amount of joy to celebrate this accomplishment with you. I would also like to express my sincere thanks to my friends who uplifted my spirits, even on my worst days, and were always ready to celebrate my wins. Finally, while I am grateful for all the educators and mentors I have had over the years, I owe a special debt of gratitude to Katie Barber, Mark Godwin, Valeria Canto-Soler, Fernando and Reuben Adler, Tony and Leslye Staub, Joseph Brzezinski, and Jeremy Mercuri. Without the support of everyone in this group and more, I would not be where I am today.

Austin Bell-Hensley

Washington University in St. Louis

August 2024

Dedicated to my wife, my parents, my sister, my grandparents, and my cat.

ABSTRACT OF THE DISSERTATION

Epigenetic Regulation of Skeletal Development

by

Austin Bell-Hensley

Doctor of Philosophy in Biomedical Engineering

Washington University in St. Louis, 2024

Professor Audrey McAlinden, Chair

Professor Farshid Guilak, Co-Chair

Treatment of disorders that disrupt homeostasis of skeletal tissues, such as osteoarthritis, and developmental skeletal diseases, such as overgrowth syndromes, requires a precise understanding of skeletal development. Osteoarthritis is a whole joint disorder that can be caused by articular cartilage defects that illicit an inflammatory immune response. Articular cartilage does not have intrinsic processes for repair or regeneration, so it is necessary to develop tissue constructs to repair the native tissue.

Since articular cartilage is not capable of repair, it is difficult to engraft cartilage tissue constructs. As such, it is necessary to develop a layered osteochondral construct that can integrate with the bone layer just beneath the articular cartilage. Generation of a layered tissue construct presents a major challenge because bone and cartilage differentiation require very different stimulating cues. Here, we attempted to develop a multi-compartmental "bi-culture" system to promote spatially restricted differentiation of an osteochondral tissue construct. We use a progenitor cell derived from articular cartilage called a cartilage progenitor cell which is capable of differentiating into articular-like chondrocytes, hypertrophic-like chondrocytes, or osteoblasts, all of which play important roles in osteochondral tissue development. We use a demineralized human cancellous bone scaffold which has demonstrated its propensity to support

bone and cartilage formation and success in engrafting with the host tissues. However, we find that the osteogenic and chondrogenic cues we use to develop the osteochondral tissue construct are insufficient, and we need to apply more native-like stimulation of tissue development to obtain an osteochondral construct.

Epigenetic regulation has steadily gained attention in the field of orthopaedics. It has become clear that a variety of epigenetic factors play important roles in the development and homeostasis of skeletal tissues. Among these epigenetic factors are microRNAs. MicroRNA profiling studies have identified many differentially expressed miRNAs in chondrocytes at distinct sites of developing limb growth plate. Among the top differentially expressed microRNAs are miR-181a-1 and miR-138.

miR-181a-1 is part of the miR-181a/b-1 cluster and has a reported pro-differentiation function in multiple *in vitro* differentiation assays. Here, we used lentiviral approaches to over-express this microRNA cluster during chondrogenesis of cartilage progenitor cells in micromass pellet cultures and report a pro-differentiation role. Using bulk RNA-sequencing, we identify a number of pro-anabolic genes and pathways upregulated by miR-181a/b-1 over-expression during cartilage progenitor cell chondrogenesis. The gene most downregulated by miR-181a/b-1 over-expression was aquaporin-9 which has not been studied extensively in cartilage development or homeostasis. We report that aquaporin-9 is expressed intracellularly during cartilage progenitor cell chondrogenesis and that it is not a direct target of miR-181a/b-1. The miR-181a/b-1 cluster appears to positively regulate chondrogenesis and chondrocyte anabolism, and one of the mechanisms for this effect may be indirect downregulation of aquaporin-9.

miR-138 has been identified as an anti-proliferation, anti-adhesion, anti-motility agent, primarily in the context of cancers. Here, we used lentiviral approaches to over-express miR-138 during cartilage progenitor cell micromass pellet chondrogenesis and report that it has limited impact on

differentiation. Bulk RNA-sequencing analysis detected only one significantly differentially expressed gene and minimal perturbation of chondrogenic-related signaling pathways. Our report adds to the ambiguous literature on the role of miR-138 in chondrogenesis.

Another class of epigenetic regulators that are known to regulate skeletal development is DNA methyltransferases. Mutations in one of member of this class, DNMT3A, are responsible for a skeletal overgrowth syndrome called Tatton-Brown-Rahman syndrome. Interestingly, Tatton-Brown-Rahman syndrome patients also have intellectual and behavioral disorders, so it falls under the umbrella of overgrowth and intellectual disability syndromes.

Recently, two different mouse models were generated with two distinct mutations in *Dnmt3a*, both of which are homologous to mutations found in human Tatton-Brown-Rahman syndrome patients. Here, we perform a thorough skeletal characterization on mice with either of the *Dnmt3a* mutations to assess the potential of these mice as an animal model for Tatton-Brown-Rahman syndrome. We report that these mice mimic some of the skeletal overgrowth phenotypes found in patients with these mutations. Investigating the cellular mechanism responsible for this overgrowth, we find that the growth plates in both *Dnmt3a* mutant mice are significantly thicker than their wild-type littermates during skeletal development. These findings indicate that both *Dnmt3a* mutant mice are good animal models for Tatton-Brown-Rahman syndrome.

Given that DNMT3A has been reported to have a pro-osteogenic and anti-osteoclastogenic function, we hypothesized that there may be additional skeletal phenotypes present in the *Dnmt3a* mutant mice. We expanded our skeletal characterization to include other skeletal parameters such as trabecular and cortical bone indices, bone mechanical properties, and bone marrow adipose tissue accumulation. We found reduced cortical bone thickness and impaired bone mechanical properties in both of the *Dnmt3a* mutants. We investigated osteoblast function and osteoclast number in the mice during development but did not identify a clear cellular

mechanism. We also report a sex-specific and mutation-specific upregulation of bone marrow adipose tissue in mice with one of the *Dnmt3a* mutations. These additional skeletal phenotypes represent opportunity to improve our understanding of Tatton-Brown-Rahman syndrome and, more broadly, overgrowth and intellectual disability syndromes.

These investigations of microRNAs and DNA methyltransferases during *in vitro* chondrogenesis and *in vivo* skeletal overgrowth add to the rapidly expanding body of literature on epigenetic regulators in skeletal development. As we learn more about the functional roles of epigenetic regulators, we can better use them as tools to treat diseases and improve human health.

<u>Preface</u>

Creating a treatment for articular cartilage injuries stems from a personal experience with joint injuries. I was diagnosed with an articular cartilage defect, Osgood-Schlatter's disease, and osteochondritis dissecans when I was 14 years old. By the time I graduated high school, I had already undergone three knee surgeries. Even after three surgeries, I know that it is a matter of when, not if, I will get osteoarthritis.

Ever since my first surgery, I have dedicated myself to finding a treatment for osteoarthritis that doesn't involve replacing my joints with metal and plastic.

This dissertation is a milestone in my lifelong goal of developing an osteoarthritis treatment.

Chapter 1: Background for MicroRNA-Mediated Osteochondral Tissue Engineering

1.1 Articular Cartilage

Articular cartilage serves a vital role in load-bearing joints like the knee, the hip, and the spine. It enables nearly frictionless articulation despite massive compressive forces being applied constantly. This unique function is made possible by the cells that make up articular cartilage (articular chondrocytes) and the extracellular matrix (ECM) they produce. As the human life span extends, cartilage is forced to support joint articulation for longer. Unfortunately, several proteins in the cartilage ECM have a half-life shorter than the modern average human lifespan so our cartilage breaks down and begins to degrade as we age. As aged population expands, the number patients worldwide who suffer from cartilage degenerative disorders, such as osteoarthritis (OA), grows. Recent reports suggest that roughly 595 million people worldwide suffer from OA and that number continues to rise[1]. Despite the massive health and economic burdens that these disorders cause, there are limited regenerative cartilage therapies available. To develop appropriate therapies, it is critical for the fields of cartilage regeneration and cartilage tissue engineering to cultivate biomimetic cartilage by using techniques inspired by natural cartilage developmental processes.

1.1.1 Development

Skeletal development occurs through a tightly regulated processes called endochondral ossification[2-4]. In mammals, this process begins with mesenchymal condensations made up of mesoderm-derived cells, known as mesenchymal stem/stromal cells (MSCs). Shortly after the condensation forms, the MSCs begin to express *SOX9,* committing to a chondrocyte lineage[5,6]. These $SOX9^+$ cells, or "resting chondrocytes," do not proliferate much but they do secrete a type

II collagen matrix comprised primarily of the type IIA collagen isoform – this isoform is unique to the embryonic cartilage matrix[7]. Resting chondrocytes near the center of the mesenchymal condensation begin to express transcription factors *SOX5* and *SOX6*, in tandem with *SOX9*, which matures these resting chondrocytes through proliferating and prehypertrophic chondrocyte stages, and eventually advances them into terminally differentiated hypertrophic chondrocytes. Expression of *SOX9* subsides in these hypertrophic chondrocytes while expression of the osteoblastic transcription factor *RUNX2* ramps up. The hypertrophic chondrocytes lay down a type X collagen matrix and then undergo apoptosis, creating an ECM scaffolding for osteoblasts to begin accumulating a mineralized matrix to form bone tissue. The site where these osteoblasts begin to deposit mineralized matrix is called the primary ossification center (POC). In long bones, the POC typically forms near the mid-point of the bone's diaphysis and growth occurs via interstitial growth. That is, bone begins to accumulate at the POC, dividing the center-most layers of hypertrophic chondrocytes and pushing the ends of the bone away from the center. Later in development, the ends of the bone widen through a second iteration of endochondral ossification at the secondary ossification center (SOC) which typically forms in the mid-epiphysis on either end of the bone[8]. The cartilaginous region between the POC and SOC is known as the growth plate, but it is eventually mineralized by the highly active osteoblast population.

However, the chondrocytes that undergo endochondral ossification are distinct from chondrocytes that give rise to articular cartilage[9-11]. Layers of articular chondrocytes are added to the ends of long bones via an appositional growth mechanism. These cells are derived from the *SOX9*+ resting chondrocytes near the "interzone" – the space that forms between long bones during a process known as joint cavitation. These resting chondrocytes begin expressing *GDF5*

and lineage tracing studies in *Gdf5*-Cre mice have shown that these cells become articular chondrocytes[12,13]. These *GDF5*^{+} interzone cells also have high levels of canonical Wnt signaling which induces expression of one of the most important proteins expressed in the superficial zone of articular cartilage: lubricin[11,14,15]. Lubricin, encoded by the *PRG4* gene, is responsible for "lubricating" the superficial zone of articular cartilage, enabling frictionless movement in articular joints. *PRG4*^{+} cells serve as a progenitor population for chondrocytes in all four zones of articular cartilage: the superficial, middle, deep, and calcified cartilage zones[16].

1.1.2 Layers of Articular Cartilage

The superficial zone of human articular cartilage is about 2 mm thick and is comprised of chondrocytes that are stretched into an elongated shape parallel to the surface of the articular joint. There is a relatively high cell density in this zone and the ECM fibers are tangentially aligned to the joint surface. These characteristics make the superficial zone ideal for enduring shear loading typical of articular joints. Going slightly deeper, the middle zone is made up of relatively small, rounded chondrocytes and a disorganized matrix that is not aligned with the joint surface. This zone serves as a transition between the superficial and deep zones. Finally, the deep zone of cartilage contains stacked columns of relatively large chondrocytes with a lower cell density. The ECM fibers in this zone are aligned perpendicularly to the joint surface, ideal for resisting compressive loading. Beneath the deep zone, the cartilage transitions into bone tissue at a natural demarcation called the tidemark. This zone, called the calcified cartilage zone, is made up of a thin layer of hypertrophic chondrocytes that are left over from the SOC. The calcified cartilage zone serves as an important intermediary between cartilage and subchondral bone[17,18].

1.1.3 Extracellular Matrix Components

The mechanical properties of articular cartilage are facilitated by the ECM proteins secreted and maintained by articular chondrocytes. The proteoglycan lubricin allows superficial zone chondrocytes to have frictionless articulation[11,14,15]. The main structural protein in healthy cartilage is type II collagen (COLII), which serves as a backbone for the collagen network which includes type IX and XI collagens (COLIX and COLXI, respectively)[19,20]. Of note, the COLII matrix secreted by mature differentiated chondrocytes secrete a COLII matrix from *COL2A1* transcripts spliced to exclude exon 2 ("COLIIB") while embryonic chondroprogenitors translate their COLII from alternatively spliced *COL2A1* transcripts that contain exon 2 ("COLIIA")[21,22]. These isoforms of COLII can be used to distinguish chondroprogenitors from differentiated chondrocytes. In either case, resident proteoglycans – primarily aggrecan – interweave the collagen network and provide the tensile strength of cartilage. Other proteoglycans (biglycan, decorin, and perlecan) present in the cartilage ECM bind to each other and their presence bolsters the mechanical strength of the tissue. Importantly, this collagen-proteoglycan matrix is highly porous and can be filled with water which supports the biomechanical properties of the tissue. Other molecules are also present in healthy cartilage to aid with signal transduction, cell-ECM interactions, cell adhesion, and matrix maintenance including asporin, cartilage oligomeric matrix protein (COMP), cartilage intermediate layer protein (CILP), elastin, fibromodulin, fibronectin, fibulin, hyaluronic acid, laminin, matrilins, and nidogen.

1.1.4 Osteoarthritis

While healthy articular cartilage has ideal properties for joint articulation, it is highly susceptible to "wear and tear" injuries because it endures such repetitive loading. As the human lifespan has extended, cartilage defects caused by overuse have become more prevalent. When a defect occurs in articular cartilage, the tissue is unable to repair itself because it lacks vascularization

and has low cell count[23,24]. As a result, articular cartilage defects propagate and contribute to whole joint diseases like OA. Clinical studies have shown that patients are nearly three times more likely to suffer from OA after experiencing an articular cartilage defect[25]. Originally deemed a degenerative, "wear and tear" joint disorder, OA is now recognized as a multifactorial inflammatory disease that dysregulates remodeling and homeostasis throughout the joint[26]. While cartilage defects represent just one way to induce inflammatory OA, developing a regenerative or reparative solution for cartilage defects would substantially impact the lives of hundreds of millions of patients worldwide.

1.1.5 Articular Cartilage Treatments and Therapies

When an articular cartilage defect or OA is diagnosed, the first line of defense is palliative care in the form of non-steroidal anti-inflammatory drugs (NSAIDs) and corticosteroid injections[27]. When these pain-relieving modalities are rendered ineffective, several treatment options are available such as microfracture (MF), osteochondral autograft transfer, osteochondral allograft transplantation, matrix-induced autologous chondrocyte implantation (MACI), and processed allograft cartilage implantation[28-32]. Unfortunately, these remedies offer a temporary solution, require creation of a secondary defect to harvest graft tissue, or have low donor availability. Ultimately, a majority of OA patients are forced to undergo invasive joint replacements where the native joint tissue is replaced with an artificial joint. There Is a clinical need for regenerative or reparative cartilage therapies that treat the underlying cause(s) of OA and improve patient outcomes. One of the major focuses of this dissertation will be development of an osteochondral construct capable of repairing cartilage defects typical of OA.

1.2 Osteochondral Tissue Engineering

Developing a biomimetic osteochondral tissue construct has proven challenging because of the structural and functional intricacies of the native tissue. There has been great success in developing cartilage and bone tissue constructs separately, and several groups have engineered methods for combining cartilage and bone tissue constructs[33-35]. However, this creates an unnatural disconnect during the development of each of these two tissues. There are several factors that must be considered for the creation of an optimal osteochondral construct: progenitor cell type, scaffold biomaterial, and biochemical/biophysical cues[36].

1.2.1 Cartilage Progenitor Cells

Identifying a cell source for osteochondral tissue engineering can be challenging. The objective of creating a tissue construct with distinct layers of tissue means that there will be divided layers of cells. This can be done by seeding multiple types of cells onto multiple scaffolds and then joining the scaffolds together with spatially tailored cell layers, or by seeding a single type of progenitor cell that is capable of differentiating into all of the cell types necessary in the final osteochondral construct. Given that bone and cartilage tissue are both derived from MSCs, it is logical to begin with MSCs, and indeed many studies have attempted to develop osteochondral constructs from MSCs. However, MSCs undergo an endochondral ossification-like process that results in bone and hypertrophic chondrocytes, but no stable articular-like chondrocytes[37]. Alternatively, chondrocytes can be seeded onto the cartilaginous phase while preosteoblasts are seeded onto the bone zone[38]. Unfortunately, it is difficult to consistently obtain enough chondrocytes to fill a three-dimensional scaffold due to their low cell density in cartilage tissue and low proliferation rate, creating a manufacturing bottleneck. Fortunately, there is a small population of resident progenitor cells in mature articular cartilage that differentiate down mesenchymal lineages[39,40]. Moreover, these cells are capable of producing stable articular-like

6

cartilage[41] and bone[42,43] in three-dimensional culture systems. These cells will be discussed in more detail in Chapter 2.

1.2.2 Demineralized Bone Scaffold

There are a vast number of three-dimensional scaffolds that have been developed and tested for osteochondral tissue engineering. To loosely outline the many designs, there are natural and synthetic, monophasic and multiphasic, and cellular and acellular osteochondral scaffolds[36]. However, there are a few central dogmas that serve as a basis for osteochondral scaffold design. The scaffold material must be biocompatible and biodegradable for successful implantation. The scaffold structure must be conducive to cellular attachment, host tissue integration, and natural cell functions such as differentiation and maturation, nutrient delivery, waste removal, matrix deposition, and communication and interaction with their environment. The material properties of the scaffold must withstand the rigorous loading present in the joint environment while communicating mechanical signals to its cellular inhabitants. One scaffold that is ideally suited to support osteochondral tissue growth and integration is the native tissue that osteochondral tissue is built on: cancellous bone. Once demineralized, cancellous bone essentially becomes a porous sponge made up of type I collagen. The McAlinden group has previously reported the CPCs can undergo osteogenesis on cancellous bone scaffolds[42,43] while other have demonstrated that MSCs can form cartilage tissue in this biomaterial[44,45]. The enhanced chondrogenic potential of CPCs, relative to MSCs, suggests that they should also be able to generate cartilage in this scaffold system.

1.2.3 Biochemical/Biophysical Cues

The native processes of endochondral ossification, joint cavitation, and articular cartilage formation are highly complex based on the large number of signaling molecules and pathways that are involved and the tight spatiotemporal regulation of those signals. Among the most

prevalent molecular mechanisms are signals related to transforming growth factor (TGF)-β

family members, bone morphogenetic proteins (BMPs), insulin growth factors (IGF), and

fibroblast growth factors (FGFs)[46,47]. Considering that different cues are necessary for bone and

cartilage formation, coated scaffolds have been developed that allow lentivirus particles to

adhere to the scaffold in a spatially restricted manner[48]. This technique can be used to transduce

cells with chondrogenic or osteogenic signals with a spatially sensitive approach. It has also been

demonstrated that mimicking physiological oxygen levels is important for generating native-like

cartilage tissue[41,49]. While "physoxia" can be achieved for chondrogenic or osteogenic cultures, it

is difficult to compartmentalize oxygen levels for osteochondral engineering. Biomimetic,

dynamic mechanical stimulation during *in vitro* differentiation has also proven beneficial for

osteochondral tissue engineering[36,50]. However, it is challenging to simultaneously balance all of

these physical and chemical cues during *in vitro* differentiation assays and additional regulation

of endogenous signaling pathways is necessary. Epigenetic control of cartilage development and

homeostasis has gained interest over recent years[51-60].

1.3 MicroRNAs

Section 1.3 and its subsections have been adapted from a review article from Hensley and

McAlinden[57], a review article by Bell-Hensley et al[61], and a research article from Bell-Hensley

et al submitted to the "Osteoarthritis and Cartilage Open" journal.

Among the epigenetic regulators that have important functions in skeletal biology are

microRNAs. MicroRNAs (miRNAs) are small, non-coding RNAs that can translationally repress

target mRNAs or induce target mRNA degradation[62-65]. This targeting is achieved via binding of

the short (6-8 nucleotide) seed sequence in the functional miRNA strand to a complementary

region of the 3'-UTR of the target mRNA. Given the short length of the seed sequence, miRNAs

have the potential to target tens to hundreds of mRNAs in a single cell type, thereby affecting many cellular pathways and networks[63,64].

1.3.1 Biogenesis

Mature non-coding miRNAs are commonly 19-24 nucleotides (nt) in length and are derived from larger precursor RNAs. Genes encoding miRNAs (predominantly located in intergenic regions or within introns of protein-coding genes) are first transcribed as large primary precursors (pri-miRNAs). In some cases, miRNA-encoding genes may be clustered (i.e. adjacently located within 10 Kb of each other as per miRBase definition) and transcribed in a polycistronic manner. Primary miRNA transcripts are processed in the nucleus by a Drosha-containing complex and the resulting precursor miRNAs (pre-miRNA) are transported to the cytoplasm and processed further by a Dicer-containing complex to form a short, mature miRNA duplex containing a 5p and 3p strand[66]. Commonly, only one of these strands is functional, meaning it will bind via its seed sequence (positions 2-8 of the mature miRNA strand) to a complementary region within the 3'UTR of a target mRNA. This interaction occurs within the RNA-induced silencing complex (RISC), the end result being either degradation of the target mRNA or inhibition of mRNA translation[67,68].

1.3.2 Therapeutic Opportunities

Their small size and high conservation between species render miRNAs as attractive therapeutic targets[65]. A phase II clinical trial was recently completed to test the effects of a miR-29 mimic drug (MRG-201; remlarsen) keloid prevention[69]. In addition, Phase 1 and 1b clinical trials have been carried out to test the effects of a miR-92a antagomir (MRG-110) in wound healing and a miR-21 antagomir (CDR132L) to treat the effects of heart failure[70]. Ongoing trials feature anti-miR-21 (RG-012; lademirsen) for Alport syndrome (Phase II) and an artificial engineered miR (AMT-130) for Huntington's Disease (Phase I/II)[71]. In addition, a vast number of active and

9

recruiting studies on http://clinicaltrials.gov/ include outcome measures for a range of miRNAs in various human diseases. Clinical studies for additional miRNAs, such as anti-miR-122 drug miravirsen and miR-34 mimic drug MRX34, have recently been halted due to limited efficacy and immune-related patient deaths, respectively. Findings from these clinical studies may lead to identification of new miRNA therapeutic targets and disease biomarkers.

1.3.3 Role in Skeletal Tissues

The myriad of targets that can be downregulated by a single miRNA make them an attractive candidate for a multifactorial disease like O. As such, many pre-clinical studies have investigated the role of miRNAs in cartilage development and homeostasis. One of the most studied miRNAs in cartilage is miR-140, whose expression is correlated with chondrocyte phenotype[72,73]. Genetic mouse models with deletion or over-expression of this miRNA further support an important function for this miRNA in regulating cartilage development and homeostasis[74,75]. A recent clinical study identified a miR-140 mutation that resulted in skeletal defects[76]. While a number of other miRNAs have been reported to regulate cartilage development and/or homeostasis, McAlinden *et al* was the first to report on miRNA expression profiling in chondrocytes of the developing human embryonic limb[77]. In this study, miR-140 was one of the most highly expressed miRNAs in chondrocytes throughout the developing growth plate, which validated the screen. Analysis of differentially expressed miRNAs revealed miR-138 and miR-181a-1 as significantly upregulated in hypertrophic chondrocytes compared to proliferating and progenitor cells, thereby suggesting that they may regulate chondrocyte differentiation as well as endochondral bone formation. The roles of these miRNAs in chondrogenesis will be a major focus of this dissertation.

1.4 Summary of Aims

This project aims to develop a native-like osteochondral tissue construct using a biomimetic differentiation scheme in a clinically relevant cell type and a natural biomaterial scaffold. This will first require innovation of a novel cell culture system capable of spatially regulating cell differentiation in a three-dimensional scaffold (Chapter 2). Next, it will require a progenitor cell that is capable of both endochondral ossification and articular chondrocyte-like differentiation schemes, such as cartilage progenitor cells (Chapter 2-4). Finally, it will require manipulation of biological pathways using novel endogenous cues such as miR-181a/b-1 and miR-138 (Chapter 3-4). The ideas and knowledge gained from these studies will inform future osteochondral tissue engineering studies and highlight the value that miRNAs can bring to the field of orthopaedics.

1.5 References

1   Collaborators, G. O. Global, regional, and national burden of osteoarthritis, 1990-2020 and projections to 2050: a systematic analysis for the Global Burden of Disease Study 2021. *Lancet Rheumatol* **5**, e508-e522 (2023). https://doi.org/10.1016/S2665-9913(23)00163-7

2   Karsenty, G. & Wagner, E. F. Reaching a genetic and molecular understanding of skeletal development. *Dev Cell* **2**, 389-406 (2002). https://doi.org/10.1016/s1534-5807(02)00157-0

3   Long, F. & Ornitz, D. M. Development of the endochondral skeleton. *Cold Spring Harb Perspect Biol* **5**, a008334 (2013). https://doi.org/10.1101/cshperspect.a008334

4   Galea, G. L., Zein, M. R., Allen, S. & Francis-West, P. Making and shaping endochondral and intramembranous bones. *Dev Dyn* **250**, 414-449 (2021). https://doi.org/10.1002/dvdy.278

5   Kozhemyakina, E., Lassar, A. B. & Zelzer, E. A pathway to bone: signaling molecules and transcription factors involved in chondrocyte development and maturation. *Development* **142**, 817-831 (2015).

6   Liu, C. F., Angelozzi, M., Haseeb, A. & Lefebvre, V. SOX9 is dispensable for the initiation of epigenetic remodeling and the activation of marker genes at the onset of chondrogenesis. *Development* **145** (2018). https://doi.org/10.1242/dev.164459

7   McAlinden, A. Alternative splicing of type II procollagen: IIB or not IIB? *Connect Tissue Res* **55**, 165-176 (2014). https://doi.org/10.3109/03008207.2014.908860

8   Aghajanian, P. & Mohan, S. The art of building bone: emerging role of chondrocyte-to-osteoblast transdifferentiation in endochondral ossification. *Bone Res* **6**, 19 (2018). https://doi.org/10.1038/s41413-018-0021-z

9   Archer, C. W., Morrison, H. & Pitsillides, A. A. Cellular aspects of the development of diarthrodial joints and articular cartilage. *J Anat* **184 (Pt 3)**, 447-456 (1994).

10   Decker, R. S., Koyama, E. & Pacifici, M. Genesis and morphogenesis of limb synovial joints and articular cartilage. *Matrix Biol* **39**, 5-10 (2014). https://doi.org/10.1016/j.matbio.2014.08.006

11   Chijimatsu, R. & Saito, T. Mechanisms of synovial joint and articular cartilage development. *Cell Mol Life Sci* **76**, 3939-3952 (2019). https://doi.org/10.1007/s00018-019-03191-5

12   Shwartz, Y., Viukov, S., Krief, S. & Zelzer, E. Joint Development Involves a Continuous Influx of Gdf5-Positive Cells. *Cell Rep* **15**, 2577-2587 (2016). https://doi.org/10.1016/j.celrep.2016.05.055

13   Rountree, R. B. *et al.* BMP receptor signaling is required for postnatal maintenance of articular cartilage. *PloS Biol* **2**, e355 (2004). https://doi.org/10.1371/journal.pbio.0020355

14   Rhee, D. K. *et al.* The secreted glycoprotein lubricin protects cartilage surfaces and inhibits synovial cell overgrowth. *J Clin Invest* **115**, 622-631 (2005). https://doi.org/10.1172/JCI22263

15   Xuan, F. *et al.* Wnt/β-catenin signaling contributes to articular cartilage homeostasis through lubricin induction in the superficial zone. *Arthritis Res Ther* **21**, 247 (2019). https://doi.org/10.1186/s13075-019-2041-5

16   Kozhemyakina, E. *et al.* Identification of a Prg4-expressing articular cartilage progenitor cell population in mice. *Arthritis Rheumatol* **67**, 1261-1273 (2015). https://doi.org/10.1002/art.39030

17   Oegema, T. R., Carpenter, R. J., Hofmeister, F. & Thompson, R. C. The interaction of the zone of calcified cartilage and subchondral bone in osteoarthritis. *Microsc Res Tech* **37**, 324-332 (1997). https://doi.org/10.1002/(SICI)1097-0029(19970515)37:4<324::AID-JEMT7>3.0.CO;2-K

18   Arkill, K. P. & Winlove, C. P. Solute transport in the deep and calcified zones of articular cartilage. *Osteoarthritis Cartilage* **16**, 708-714 (2008). https://doi.org/10.1016/j.joca.2007.10.001

19   Peng, Z. *et al.* The regulation of cartilage extracellular matrix homeostasis in joint cartilage degeneration and regeneration. *Biomaterials* **268**, 120555 (2021). https://doi.org/10.1016/j.biomaterials.2020.120555

20   Goldring, M. B. & Marcu, K. B. Cartilage homeostasis in health and rheumatic diseases. *Arthritis Res Ther* **11**, 224 (2009). https://doi.org/10.1186/ar2592

21   McAlinden, A., Johnstone, B., Kollar, J., Kazmi, N. & Hering, T. M. Expression of two novel alternatively spliced COL2A1 isoforms during chondrocyte differentiation. *Matrix Biol* **27**, 254-266 (2008). https://doi.org/10.1016/j.matbio.2007.10.002

22   Ryan, M. C. & Sandell, L. J. Differential expression of a cysteine-rich domain in the amino-terminal propeptide of type II (cartilage) procollagen by alternative splicing of mRNA. *J Biol Chem* **265**, 10334-10339 (1990).

23   Mankin, H. J. The response of articular cartilage to mechanical injury. *J Bone Joint Surg Am* **64**, 460-466 (1982).

24   Sandell, L. J. Etiology of osteoarthritis: genetics and synovial joint development. *Nat Rev Rheumatol* **8**, 77-89 (2012). https://doi.org/10.1038/nrrheum.2011.199

25   Everhart, J. S., Abouljoud, M. M., Kirven, J. C. & Flanigan, D. C. Full-Thickness Cartilage Defects Are Important Independent Predictive Factors for Progression to Total Knee Arthroplasty in Older Adults with Minimal to Moderate Osteoarthritis: Data from the Osteoarthritis Initiative. *J Bone Joint Surg Am* **101**, 56-63 (2019). https://doi.org/10.2106/JBJS.17.01657

26   Loeser, R. F., Goldring, S. R., Scanzello, C. R. & Goldring, M. B. Osteoarthritis: a disease of the joint as an organ. *Arthritis Rheum* **64**, 1697-1707 (2012). https://doi.org/10.1002/art.34453

27   Jüni, P. *et al.* Intra-articular corticosteroid for knee osteoarthritis. *Cochrane Database Syst Rev* **2015**, CD005328 (2015). https://doi.org/10.1002/14651858.CD005328.pub3

28   Gobbi, A., Karnatzikos, G. & Kumar, A. Long-term results after microfracture treatment for full-thickness knee chondral lesions in athletes. *Knee Surg Sports Traumatol Arthrosc* **22**, 1986-1996 (2014). https://doi.org/10.1007/s00167-013-2676-8

29   Solheim, E., Hegna, J. & Inderhaug, E. Long-term clinical follow-up of microfracture versus mosaicplasty in articular cartilage defects of medial femoral condyle. *Knee* **24**, 1402-1407 (2017). https://doi.org/10.1016/j.knee.2017.08.061

30   Dean, C. S., Chahla, J., Serra Cruz, R. & LaPrade, R. F. Fresh Osteochondral Allograft Transplantation for Treatment of Articular Cartilage Defects of the Knee. *Arthrosc Tech* **5**, e157-161 (2016). https://doi.org/10.1016/j.eats.2015.10.015

31   Andriolo, L., Merli, G., Filardo, G., Marcacci, M. & Kon, E. Failure of Autologous Chondrocyte Implantation. *Sports Med Arthrosc Rev* **25**, 10-18 (2017). https://doi.org/10.1097/JSA.0000000000000137

32   Kwon, H. *et al.* Surgical and tissue engineering strategies for articular cartilage and meniscus repair. *Nat Rev Rheumatol* **15**, 550-570 (2019). https://doi.org/10.1038/s41584-019-0255-1

33   Brown, W. E., Huey, D. J., Hu, J. C. & Athanasiou, K. A. Functional self-assembled neocartilage as part of a biphasic osteochondral construct. *PloS One* **13**, e0195261 (2018). https://doi.org/10.1371/journal.pone.0195261

34   Critchley, S. *et al.* 3D printing of fibre-reinforced cartilaginous templates for the regeneration of osteochondral defects. *Acta Biomater* **113**, 130-143 (2020). https://doi.org/10.1016/j.actbio.2020.05.040

35   Gong, L. *et al.* An interleukin-4-loaded bi-layer 3D printed scaffold promotes osteochondral regeneration. *Acta Biomater* **117**, 246-260 (2020). https://doi.org/10.1016/j.actbio.2020.09.039

36   Wei, W. & Dai, H. Articular cartilage and osteochondral tissue engineering techniques: Recent advances and challenges. *Bioact Mater* **6**, 4830-4855 (2021). https://doi.org/10.1016/j.bioactmat.2021.05.011

37   Dickhut, A. *et al.* Calcification or dedifferentiation: requirement to lock mesenchymal stem cells in a desired differentiation stage. *J Cell Physiol* **219**, 219-226 (2009). https://doi.org/10.1002/jcp.21673

38   Korpayev, S. *et al.* Chitosan/collagen based biomimetic osteochondral tissue constructs: A growth factor-free approach. *Int J Biol Macromol* **156**, 681-690 (2020). https://doi.org/10.1016/j.ijbiomac.2020.04.109

39   Barbero, A., Ploegert, S., Heberer, M. & Martin, I. Plasticity of clonal populations of dedifferentiated adult human articular chondrocytes. *Arthritis Rheum* **48**, 1315-1325 (2003). https://doi.org/10.1002/art.10950

40   Dowthwaite, G. P. *et al.* The surface of articular cartilage contains a progenitor cell population. *J Cell Sci* **117**, 889-897 (2004). https://doi.org/10.1242/jcs.00912

41   Anderson, D. E., Markway, B. D., Weekes, K. J., McCarthy, H. E. & Johnstone, B. Physioxia Promotes the Articular Chondrocyte-Like Phenotype in Human Chondroprogenitor-Derived Self-Organized Tissue. *Tissue Eng Part A* **24**, 264-274 (2018). https://doi.org/10.1089/ten.TEA.2016.0510

42   Zheng, H. *et al.* MicroRNA-138 Inhibits Osteogenic Differentiation and Mineralization of Human Dedifferentiated Chondrocytes by Regulating RhoC and the Actin Cytoskeleton. *JBMR Plus* **3**, e10071 (2019). https://doi.org/10.1002/jbm4.10071

43   Zheng, H., Liu, J., Tycksen, E., Nunley, R. & McAlinden, A. MicroRNA-181a/b-1 over-expression enhances osteogenesis by modulating PTEN/PI3K/AKT signaling and mitochondrial metabolism. *Bone* **123**, 92-102 (2019). https://doi.org/10.1016/j.bone.2019.03.020

44   Shahmoradi, S. R. *et al.* Induction of Chondrogenic Differentiation in Human Mesenchymal Stem Cells Cultured on Human Demineralized Bone Matrix Scaffold under Hydrostatic Pressure. *Tissue Eng Regen Med* **16**, 69-80 (2019). https://doi.org/10.1007/s13770-018-0164-4

45   Wang, X. *et al.* Demineralized bone matrix combined bone marrow mesenchymal stem cells, bone morphogenetic protein-2 and transforming growth factor-β3 gene promoted

pig cartilage defect repair. *PloS One* **9**, e116061 (2014). https://doi.org/10.1371/journal.pone.0116061

46   Mendes, L. F. *et al.* Advancing osteochondral tissue engineering: bone morphogenetic protein, transforming growth factor, and fibroblast growth factor signaling drive ordered differentiation of periosteal cells resulting in stable cartilage and bone formation in vivo. *Stem Cell Res Ther* **9**, 42 (2018). https://doi.org/10.1186/s13287-018-0787-3

47   Danišovič, L., Varga, I. & Polák, S. Growth factors and chondrogenic differentiation of mesenchymal stem cells. *Tissue Cell* **44**, 69-73 (2012). https://doi.org/10.1016/j.tice.2011.11.005

48   Brunger, J. M. *et al.* Scaffold-mediated lentiviral transduction for functional tissue engineering of cartilage. *Proc Natl Acad Sci U S A* **111**, E798-806 (2014). https://doi.org/10.1073/pnas.1321744111

49   Anderson, D. E., Markway, B. D., Bond, D., McCarthy, H. E. & Johnstone, B. Responses to altered oxygen tension are distinct between human stem cells of high and low chondrogenic capacity. *Stem Cell Res Ther* **7**, 154 (2016). https://doi.org/10.1186/s13287-016-0419-8

50   Steinmetz, N. J., Aisenbrey, E. A., Westbrook, K. K., Qi, H. J. & Bryant, S. J. Mechanical loading regulates human MSC differentiation in a multi-layer hydrogel for osteochondral tissue engineering. *Acta Biomater* **21**, 142-153 (2015). https://doi.org/10.1016/j.actbio.2015.04.015

51   Goldring, M. B. & Marcu, K. B. Epigenomic and microRNA-mediated regulation in cartilage development, homeostasis, and osteoarthritis. *Trends Mol Med* **18**, 109-118 (2012). https://doi.org/10.1016/j.molmed.2011.11.005

52   Barter, M. J., Bui, C. & Young, D. A. Epigenetic mechanisms in cartilage and osteoarthritis: DNA methylation, histone modifications and microRNAs. *Osteoarthritis Cartilage* **20**, 339-349 (2012). https://doi.org/10.1016/j.joca.2011.12.012

53   Lian, J. B. *et al.* MicroRNA control of bone formation and homeostasis. *Nat Rev Endocrinol* **8**, 212-227 (2012). https://doi.org/10.1038/nrendo.2011.234

54   Hassan, M. Q., Tye, C. E., Stein, G. S. & Lian, J. B. Non-coding RNAs: Epigenetic regulators of bone development and homeostasis. *Bone* **81**, 746-756 (2015). https://doi.org/10.1016/j.bone.2015.05.026

55   McAlinden, A. & Im, G. I. MicroRNAs in orthopaedic research: Disease associations, potential therapeutic applications, and perspectives. *J Orthop Res* **36**, 33-51 (2018). https://doi.org/10.1002/jor.23822

56   Allas, L., Boumédiene, K. & Baugé, C. Epigenetic dynamic during endochondral ossification and articular cartilage development. *Bone* **120**, 523-532 (2019). https://doi.org/10.1016/j.bone.2018.10.004

57   Hensley, A. P. & McAlinden, A. The role of microRNAs in bone development. *Bone* **143**, 115760 (2021). https://doi.org/10.1016/j.bone.2020.115760

58   Gámez, B., Rodriguez-Carballo, E. & Ventura, F. MicroRNAs and post-transcriptional regulation of skeletal development. *J Mol Endocrinol* **52**, R179-197 (2014). https://doi.org/10.1530/JME-13-0294

59   Sera, S. R. & Zur Nieden, N. I. microRNA Regulation of Skeletal Development. *Curr Osteoporos Rep* **15**, 353-366 (2017). https://doi.org/10.1007/s11914-017-0379-7

60   Gordon, J. A. *et al.* Epigenetic pathways regulating bone homeostasis: potential targeting for intervention of skeletal disorders. *Curr Osteoporos Rep* **12**, 496-506 (2014). https://doi.org/10.1007/s11914-014-0240-1

61   Bell-Hensley, A., Das, S. & McAlinden, A. The miR-181 family: Wide-ranging pathophysiological effects on cell fate and function. *J Cell Physiol* **238**, 698-713 (2023). https://doi.org/10.1002/jcp.30969

62   Ambros, V. The functions of animal microRNAs. *Nature* **431**, 350-355 (2004). https://doi.org/10.1038/nature02871

63   Bartel, D. P. MicroRNAs: genomics, biogenesis, mechanism, and function. *Cell* **116**, 281-297 (2004). https://doi.org/10.1016/s0092-8674(04)00045-5

64   Bartel, D. P. MicroRNAs: target recognition and regulatory functions. *Cell* **136**, 215-233 (2009). https://doi.org/10.1016/j.cell.2009.01.002

65   Diener, C., Keller, A. & Meese, E. Emerging concepts of miRNA therapeutics: from cells to clinic. *Trends Genet* (2022). https://doi.org/10.1016/j.tig.2022.02.006

66   Ha, M. & Kim, V. N. Regulation of microRNA biogenesis. *Nature reviews Molecular cell biology* **15**, 509-524 (2014).

67   Eulalio, A., Huntzinger, E. & Izaurralde, E. Getting to the root of miRNA-mediated gene silencing. *Cell* **132**, 9-14 (2008). https://doi.org/10.1016/j.cell.2007.12.024

68   Djuranovic, S., Nahvi, A. & Green, R. miRNA-mediated gene silencing by translational repression followed by mRNA deadenylation and decay. *Science* **336**, 237-240 (2012). https://doi.org/10.1126/science.1215691

69   Gallant-Behm, C. L. *et al.* A MicroRNA-29 Mimic (Remlarsen) Represses Extracellular Matrix Expression and Fibroplasia in the Skin. *J Invest Dermatol* **139**, 1073-1081 (2019). https://doi.org/10.1016/j.jid.2018.11.007

70   Täubel, J. *et al.* Novel antisense therapy targeting microRNA-132 in patients with heart failure: results of a first-in-human Phase 1b randomized, double-blind, placebo-controlled study. *Eur Heart J* **42**, 178-188 (2021). https://doi.org/10.1093/eurheartj/ehaa898

71   Rodrigues, F. B. & Wild, E. J. Huntington's Disease Clinical Trials Corner: April 2020. *J Huntingtons Dis* **9**, 185-197 (2020). https://doi.org/10.3233/JHD-200002

72   Zhang, R., Ma, J. & Yao, J. Molecular mechanisms of the cartilage-specific microRNA-140 in osteoarthritis. *Inflamm Res* **62**, 871-877 (2013). https://doi.org/10.1007/s00011-013-0654-8

73   Duan, L., Liang, Y., Xu, X., Xiao, Y. & Wang, D. Recent progress on the role of miR-140 in cartilage matrix remodelling and its implications for osteoarthritis treatment. *Arthritis Res Ther* **22**, 194 (2020). https://doi.org/10.1186/s13075-020-02290-0

74   Miyaki, S. *et al.* MicroRNA-140 plays dual roles in both cartilage development and homeostasis. *Genes Dev* **24**, 1173-1185 (2010). https://doi.org/10.1101/gad.1915510

75   Nakamura, Y., Inloes, J. B., Katagiri, T. & Kobayashi, T. Chondrocyte-specific microRNA-140 regulates endochondral bone development and targets Dnpep to modulate bone morphogenetic protein signaling. *Mol Cell Biol* **31**, 3019-3028 (2011). https://doi.org/10.1128/MCB.05178-11

76   Grigelioniene, G. *et al.* Gain-of-function mutation of microRNA-140 in human skeletal dysplasia. *Nat Med* **25**, 583-590 (2019). https://doi.org/10.1038/s41591-019-0353-2

77   McAlinden, A., Varghese, N., Wirthlin, L. & Chang, L. W. Differentially expressed microRNAs in chondrocytes from distinct regions of developing human cartilage. *PloS One* **8**, e75012 (2013). https://doi.org/10.1371/journal.pone.0075012

Chapter 2: Cartilage Progenitor Cells for Osteochondral Engineering

2.1 Abstract

Cartilage degenerative diseases result in damage to both cartilage and subchondral bone tissues. While bone is a dynamic tissue that is capable of self-repair, cartilage cannot repair itself and can be challenging to repair even with surgical interventions. As such, it is necessary to develop osteochondral constructs that can integrate with subchondral bone and functionally replace or regenerate the degenerated cartilage tissue. The challenge with creating an osteochondral construct *in vitro* is guiding spatially regulated cell differentiation in a single tissue construct. Here, we design a novel "bi-culture system" that can overcome the obstacle of spatially regulated differentiation. The bi-culture system was used with a cartilage progenitor cell-seeded demineralized bone scaffold. Our group has previously achieved bone formation in this system using osteogenic induction media, but cartilage formation with this combination of cells and biomaterial had not previously been reported. We report that the bi-culture system can spatially restrict osteogenic differentiation but fails to induce chondrogenic differentiation. We confirmed that our seeding technique and biomaterial supported adhesion of viable cartilage progenitor cells in our scaffold but learned that there is high variability in the multilineage differentiation potential of cartilage progenitor cells from different donors. Ultimately, we need to improve chondrogenic induction of cartilage progenitor cells to develop an osteochondral construct. However, the bi-culture system described herein shows promise for *in vitro* development of layered tissue constructs.

2.2 Introduction

Many bodily tissues are capable of self-repair or self-regeneration. Cartilage, however, is not capable of either. This attribute is a result of the avascular nature of cartilage which prevents delivery of key nutrients and cells that would be necessary to facilitate the native healing process. However, there is a resident population of stem-like cells in articular cartilage tissues that have been understudied and underutilized in regenerative therapies. This population has cycled through several names but will be called cartilage progenitor cells (CPCs) for the remainder of this dissertation.

The cells now known as CPCs were first detected in the early 2000s when Barbero *et al* identified cells derived from adult human articular cartilage that could proliferate into clonal colonies, be expanded in monolayer, then re-differentiate down mesenchymal lineages (chondrogenic, osteogenic, or adipogenic)[1]. Soon thereafter, Alsalamah *et al* identified a small population of cells in healthy articular cartilage, comprising about 3.5% of the total number of cells, that expressed mesenchymal stem cell (MSC) markers CD105 and CD166[2]. These cells were also capable of mesenchymal lineage differentiation. Several groups have performed more extensive characterization of CPCs[3-9], though the precise surface marker profile of CPCs is still debated[10,11].

A major advance in the field occurred when Charlie Archer's group applied an easily repeatable technique that consistently and efficiently isolated CPCs. The publication by Douthwaite *et al* describes use of differential adhesion to fibronectin (DAF) assays to select CPCs from a broader population of chondrocytes[12]. This technique was originally applied by Jones and Watt to isolate stem-like cells from the epidermis in skin tissue[13]. The concept underlying this technique is that stem-like cells express higher levels of α5β1 integrin and rapidly adhere to fibronectin, an ECM protein. In a later report from the Archer group, Williams *et al* showed that the DAF technique

could be used to isolate colony-forming, multipotent CPCs from donors of varying ages[14]. Moreover, multiple reports indicated that CPCs could be isolated from normal or osteoarthritic tissue[2,3,5,7]. For the field of cartilage tissue engineering, this created a low-cost opportunity to obtain stem-like cells that were primed for chondrogenic differentiation.

One of the key advantages to using CPCs is their ability to undergo chondrogenic differentiation that doesn't result in hypertrophic chondrocytes. Mesenchymal stem/stromal cells (MSCs) were the standard cell type for cartilage tissue engineering and *in vitro* chondrogenesis, but their popularity has faded in the last decade because of their high tendency to undergo hypertrophic differentiation[15,16]. Multiple groups have shown that CPCs can differentiate into non-hypertrophic chondrocytes more consistently than MSCs[11,17-20]. The research article from Brian Johnstone's lab by Anderson *et al* highlighted the importance of utilizing "physoxia" – oxygen levels reflective of the *in vivo* cartilage development environment – to promote CPC chondrogenesis into native-like chondrocytes[17,21]. Combining a physoxic environment with a cocktail of pro-chondrogenic molecules, CPC chondrogenesis can closely mimic natural cartilage development. This chondrogenicity has made CPCs the cell of choice for many cartilage tissue engineering constructs, including one construct that has achieved clinical success[8].

However, due to interconnected nature bone and cartilage in articular joints, a cartilage tissue construct is often insufficient to treat joint disorders. For example, osteoarthritis is typified by articular cartilage defects as well as subchondral bone sclerosis[22]. Cartilage treatments like matrix-assisted autologous chondrocyte transplantation (MACI) and microfracture have good short-term patient outcomes, but over 10% of patients are forced to undergo revision surgery, such as joint replacement, within 5 years and over 50% require revision after 15 years[23,24]. The

goal of regenerative orthopaedic therapies must be to repair the joint in a way that does not have the same health outcome of artificially replacing the entire tissue. To do this, cartilage tissue engineering must develop therapies that accommodate the layered, integrated nature of osteochondral tissue. Several groups have attempted to achieve this goal by adhering cartilage and bone tissue constructs, but even that approach is not layered and interconnected like the native osteochondral junction. As such, we set out to use CPCs, a progenitor cell capable of osteochondral differentiation, to develop an osteochondral construct.

The McAlinden group previously reported on using CPCs in osteogenic assays[25,26], but has yet to establish an *in vitro* CPC chondrogenesis assay. The goal of this study was to develop a robust, repeatable process for isolating CPCs and determining their chondrogenicity. The experiments that will be discussed in later chapters require large numbers of cells, so it was important to develop a process that could quickly and easily scale up the number of highly chondrogenic CPCs from multiple donors. Moreover, we aimed to design a bi-culture system that supported concurrent, geographically restricted differentiation of non-hypertrophic chondrocytes and osteoblasts to form a three-dimensional osteochondral construct.

2.3 Methods

2.3.1 Tissue Collection

Utilization of human osteoarthritic knee joint tissue was approved by the Washington University Human Research Protection Office (IRB ID# 201104119). Tissues were collected from patients undergoing total knee replacement surgery at Barnes-Jewish Hospital (St. Louis, MO, USA) after obtaining informed consent. Tissue was transported in a sealed container at room temperature and stored at 4°C for less than 24 hours until tissue processing occurred. In a sterile biosafety cabinet, Dulbecco's PBS (DPBS) and gauze were used to remove bodily fluids from

the tissue. Once cleaned, a scalpel and forceps were used to remove cartilage tissue from the femoral condyles. Cartilage pieces were kept hydrated by submerging them in DPBS until tissue dissection was complete. From each donor, one large cartilage piece (~10mm^3) was set aside for RNA extraction, and, when possible, another large cartilage piece was set aside for histological evaluation. All remaining cartilage pieces were used for cartilage progenitor cell isolation and expansion. Bone tissues were set aside for demineralization and three-dimensional scaffold processing.

2.3.2 Cartilage Progenitor Cell Isolation and Expansion

CPCs were isolated as previously described[12,25-27]. Before CPC isolation, fibronectin-coated T75 flasks were prepared by adding 5 mL of fibronectin coating solution (10 µg/mL bovine fibronectin, 1 mM CaCl$_2$, and 1 nM MgCl$_2$ in 0.1 M PBS) (Sigma-Aldrich) and incubating at 37°C overnight. After incubation, the coating solution was discarded and 5 mL of blocking solution (1% bovine serum albumin, 1 mM CaCl$_2$, and 1 nM MgCl$_2$ in 0.1 M PBS) (Sigma-Aldrich) was applied to the plates for 30 minutes at room temperature. Fibronectin-coated T75 flasks were stored at 4°C until use. To isolate CPCs, cartilage pieces were diced (~1 mm^3) and suspended in growth medium (DMEM/F12 with 10% FBS, 1% penicillin/streptomycin, 1% amphotericin B) containing 0.025% collagenase and 0.025% pronase. The suspension was transferred to a spinner flask overnight on a magnetic stir plate at 200 rpm in a 37°C incubator. The resulting cell suspension was washed with sterile HBSS, filtered through a 70 µm cell strainer, and plated on a fibronectin coated T75 cell culture flask for 20 minutes. Non-adherent cells were removed and plated on a second fibronectin coated T75 cell culture flask for 20 additional minutes. Non-adherent cells were removed again, labeled as passage 0 primary chondrocytes, and frozen down in growth medium with 10% DMSO for future use. After the

non-adherent cells were removed from each fibronectin coated T75 flask, the adherent cells were trypsinized and pooled. These pooled cells were labeled as passage 1 CPCs and frozen down in growth medium with 10% DMSO until expansion. After frozen storage, CPCs were expanded in growth medium for at least 4 passages, until use in differentiation assays.

2.3.3 Three-Dimensional Demineralized Human Bone Scaffold Generation

After the osteoarthritic knee tissue was cleaned and processing described in *Section 2.3.1* (Tissue Collection), cancellous bone was cut into rectangular strips (approximately 5 mm x 5 mm x 75 mm) using a bandsaw. Rectangular strips were decalcified by using a formic acid solution (Immunocal™; StatLab 1414-X) for 3 days. Partially decalcified cancellous bone strips were diced into cubes (approximately 5 mm x 5 mm x 5 mm) using a scalpel and forceps, then decalcified for another 3 days. Resulting decalcified bone "scaffolds" were washed thoroughly in DPBS (three 6-hour washes) then immersed in an antibiotic/antifungal solution (10,000 unit/ml penicillin, 10,000 µg/ml streptomycin, 25µg/ml amphotericin B) and stored at 4°C for up to one year, or until use in experiments.

2.3.4 Three-Dimensional Scaffold Osteogenic Culture

Scaffolds were handled using sterile forceps in a sterile biosafety cabinet (BSC) and rinsed in DPBS ($\geq$ 50 µL per scaffold) for 5 minutes, then sterilized by soaking them in 70% ethanol for 30 minutes at room temperature. 70% ethanol was aspirated and the scaffolds air dried in the sterile BSC at room temperature for at least one hour. Scaffolds were placed in an ultra-low attachment 24-well plate (1 scaffold/well; Corning CLS3473) for seeding. Passage 4 CPCs were trypsinized, then 50 µL of growth media containing 5×10^5 CPCs were pipetted onto each scaffold, re-pipetting the media flowthrough three times to maximize cellular uptake of the scaffold. Seeded scaffolds were incubated at 37°C and 5% CO_2 for 2 hours to give cells time to adhere to the scaffold. 1 mL of growth media was carefully added to each well and the scaffolds

were cultured for 72 hours at 37°C and 5% CO_2 to give cells time to adhere to the scaffold. After 72 hours, scaffolds were exposed to 1 mL of osteogenic induction media [αMEM containing 10% FBS, L-glutamine (100U/mL), β-glycerol phosphate (10nM), ascorbate (50μM), dexamethasone (10nM)] and incubated at 37°C and 5% CO_2 for 28 days, refreshing media three times per week.

2.3.5 Three-Dimensional Scaffold Chondrogenic Culture

Scaffolds were handled, sterilized, and air-dried as described in *Section 2.3.4* (Three-dimensional Scaffold Osteogenic Culture). Scaffolds were again placed in an ultra-low attachment 24-well plate (1 scaffold/well; Corning CLS3473) for seeding. Passage 4 CPCs were trypsinized, then suspended in fibrinogen (25 mg/mL; Sigma F3879) in 0.2% bovine serum albumin (BSA) at a density of 5 x 10^5 cells per 25 μL. In a separate tube, a "coagulating solution" comprised of 50% thrombin (50 units/mL; Sigma T7009) in 0.2% BSA, 50 mM $CaCl_2$ and 50% hyaluronate (10 mg/mL; Sigma 75043) in 0.2% BSA was mixed by pipetting. 25 μL of the fibrinogen-containing CPC suspension were pipetted onto each scaffold, re-pipetting the flowthrough three times to maximize cellular uptake of the scaffold. Then, 25 μL of the coagulating solution were pipetted onto the scaffold to create a fibrin gel. All flowthrough solution was re-pipetted onto the scaffold until the gel hardened and there was no more liquid flowthrough. 1 mL of growth media was carefully added to each well and the scaffolds were cultured for 72 hours at 37°C and 5% CO_2 to give cells time to adhere to the scaffold. After 72 hours, the seeded scaffolds were exposed to 1 mL of chondrogenic induction media [serum-free high glucose DMEM containing TGF-β3 (10 ng/mL), 1% ITS+, dexamethasone (100 nM), ascorbate (100 μM), L-proline (40 μg/mL)] and incubated at 37°C and 5% CO_2 for 21 days, refreshing media three times per week.

2.3.6 Three-Dimensional Scaffold Osteochondral Bi-Culture

A "bi-culture system" capable of exposing a single three-dimensional scaffold to two different medias at the same time was designed. This system was comprised of a 15 mL conical tube and a filter-free 1 mL pipette tip. To prevent media flow between the compartments, the demineralized bone scaffolds were preconditioned before placing them into the bi-culture system. Scaffolds followed all methods described in *Section 2.3.5* (Three-Dimensional Scaffold Chondrogenic Culture); we hypothesized that the combination of fibrin gel and cartilaginous extracellular matrix would fill the pores within the demineralized bone to prevent media flowthrough. The preconditioned scaffold was inserted into the pipette tip at the end with a wider diameter and pushed down with forceps as far as it could go. Because the scaffold was larger than the smallest diameter of the pipette tip, it became wedged in the pipette tip. This spot was marked on the pipette tip with a razor blade and the scaffold was removed. The pipette tip was then cut with a razor blade such that a portion of the scaffold would be stuck inside the pipette tip and a portion would be exposed outside the pipette tip. The razor cut surface was coated with liquified 5% low-melting point agarose gel (Sigma A4018) and the scaffold was re-inserted into the cut pipette tip. The pipette tip was incubated at room temperature for 5 minutes to give the agarose gel time to harden and form a watertight seal around the scaffold. The 1 mL pipette tip was filled with 1 mL of chondrogenic media and placed into the 15 mL conical tube. If no media flowed into the 15 mL conical tube within 5 minutes, the seal was considered watertight, and 1 mL of osteogenic media was added to the 15 mL conical tube. The scaffold was cultured in the bi-culture system for three weeks in an incubator at 37°C and 5% CO_2, refreshing both the chondrogenic media and the osteogenic media three times per week.

2.3.7 Micro-computed Tomography

Scaffolds that underwent osteogenic culture or osteochondral bi-culture culture were collected

for micro-computed tomography (μCT) analysis. Scaffolds were rinsed in DPBS (three 5-minute

washes), fixed in 10% neutral buffered formalin (NBF) for 24 hours, then rinsed in DPBS again

(three 5-minute washes). Fixed scaffolds were dehydrated using serial dilutions of ethanol (30%,

50%, 70%) and stored at 4°C for less than two weeks. Fixed scaffolds were scanned using a

Scanco μCT40 scanner (Scanco Medical AG) using scan settings of 45 kVp and 177 μA with a

300 ms integration time and an effective voxel size of 6 μm. 3D reconstructions were created

using Scanco (V6.5) software using a threshold value of 180. After scanning, scaffolds were

stored at 4°C until paraffin embedding.

2.3.8 Scaffold Histology

Paraffin-embedded scaffolds were sectioned at a 10 μm thickness and mounted on glass

histology slides. Paraffin wax was melted by incubating sections at 60°C for at least 1 hour, then

slides were deparaffinized using xylene and rehydrated in serial dilutions of ethanol (100%,

95%, 70%), followed by water immersion. H&E staining was performed by the Musculoskeletal

Histology and Morphometry Core, Washington University School of Medicine. For Safranin-O

staining, rehydrated slides were stained with Weigert's Hematoxylin for 1.5 minutes, washed in

running water for 5 minutes, and stained with 0.2% Fast Green (Sigma-Aldrich) for 2 minutes.

Samples were then rinsed in 1% glacial acetic acid (Sigma-Aldrich) and stained in 0.1% Safranin

O (Electron Microscopy Sciences) for 6 minutes. Samples were dehydrated and cleared by

incubation in 95% ethanol, 100% ethanol, and then xylene. Coverslips were mounted using

CytoSeal XYL (Thermo Fisher Scientific). Brightfield images of stained slides were taken on a

whole slide imaging system (Hamamatsu Photonics Nanozoomer 2.0-HT System) using a 20X

magnification lens.

2.3.9 Live-Dead Staining

Scaffolds made of demineralized human bone, chitosan-gelatin cryogel (a gift from Dr. Matthew Silva, Washington University, St. Louis, MO; generated as previously described[28,29]), or poly (ϵ-caprolactone) (PCL; a gift from Dr. Farshid Guilak, Washington University, St. Louis, MO; generated as previously described[30,31]) were tested as candidates for three-dimensional CPC seeding. Testing involved seeding 5×10^5 CPCs onto each scaffold either without or with fibrin gel as described in *Section 2.3.4* (Three-Dimensional Scaffold Osteogenic Culture) or *Section 2.3.5* (Three-Dimensional Scaffold Chondrogenic Culture), respectively. After the 72-hour incubation in growth media, CPC laden scaffolds were stained with the LIVE/DEAD Fixable Green Dead Cell Stain Kit (Thermo Fisher L23101) according to the manufacturer's instructions. Scaffolds were then cut in half and the cut surface was imaged on an inverted confocal microscope (Leica Dmi8) using a 40x magnification lens.

2.3.10 Pellet Chondrogenic Differentiation Assay

Passage 4 CPCs were trypsinized and resuspended in chondrogenic induction medium [serum-free high glucose DMEM containing TGF-β3 (10 ng/mL), 1% ITS+, dexamethasone (100 nM), ascorbate (100 μM), L-proline (40 μg/mL)][32,33]. Cells were seeded in 15 mL conical tubes at a density of 3×10^5 cells/tube and the tubes were centrifuged at 300xg for 5 minutes to aggregate a cell pellet at the bottom of the tube. CPC pellets were incubated at 37°C in a 5% CO_2, 5% O_2 environment for the duration of the assay. Chondrogenic induction media was refreshed three times per week for three weeks to promote chondrogenic differentiation. After Day 7, pellets were agitated during each media change to prevent the pellet from sticking to the bottom of the tube and to allow uniform media exposure.

29

2.3.11 Monolayer Differentiation Assays

Passage 4 CPCs were trypsinized and seeded in 24-well plates at a density of 1×10^5 cells/well in 0.5 mL of growth media. The 24-well plates were incubated at 37°C in a 5% CO_2 environment overnight, then the growth media was replaced with 0.5 mL of either fresh growth media (negative control), chondrogenic induction media as described in *Section 2.3.7* (Pellet Chondrogenic Differentiation Assay*)*, or osteogenic induction media [αMEM containing 10% FBS, L-glutamine (100U/mL), β-glycerol phosphate (10nM), ascorbate (50μM), dexamethasone (10nM)][25,26]. CPCs were incubated at 37°C in a 5% CO_2 environment and media was refreshed three times per week. After three days, RNA was isolated from wells for each media condition (growth media, chondrogenic induction media, or osteogenic induction media). After 14 days, wells cultured in osteogenic induction media were fixed and stained for osteogenic markers.

2.3.12 Fixation

Fixation was performed on CPC pellet cultures exposed to chondrogenic induction media for 21 days and CPCs exposed to osteogenic induction media in 24-well plates for 14 days. For the pellet cultures, chondrogenic induction media was aspirated and pellets from a single donor were pooled in a single 1.5 mL tube and rinsed with PBS at room temperature for approximately 1 minute. For the 24-well plate cultures, osteogenic induction media was aspirated, and the CPC monolayer in each well was rinsed with PBS at room temperature for approximately 1 minute. The rinsed CPCs were then incubated in 10% NBF on an orbital shaker at room temperature for 90 minutes (pellets) or 20 minutes (monolayer). Fixed CPC pellets were then rinsed with PBS for approximately 1 minute, then dehydrated in serial dilutions of ethanol (30%, 50%, 70%) for 20 minutes each, and stored at 4°C in 70% ethanol until paraffin embedding. Fixed monolayer CPCs proceeded immediately to histological staining.

2.3.13 Histology

Fixed monolayers of CPCs were stained for osteogenic differentiation using alizarin red. For

alizarin red, fixed wells were washed with DPBS (three 1-minute washes) then 2% alizarin red S

(ScienCell 0223) staining solution was added to the well. Wells were incubated at in staining

solution for 1 hour at 37°C. Wells were rinsed with deionized water until excess stain was

removed, then imaged using a 12-megapixel camera. Paraffin-embedded pellets were sectioned,

stained, and coverslipped following the same workflow and safranin-O staining protocol

described in *Section 2.3.8* (Scaffold Histology). Brightfield images of stained slides were taken

on a whole slide imaging system (Hamamatsu Photonics Nanozoomer 2.0-HT System) using a

20X magnification lens.

2.4 Results

2.4.1 Three-dimensional osteogenic differentiation of cartilage progenitor cells

Pilot experiments to validate three-dimensional osteogenic differentiation of CPCs were carried

out. These protocols built on existing work from the McAlinden lab, but added deeper analysis to

confirm that osteogenic differentiation was not restricted to the surface of the three-dimensional

scaffold[25,26]. Prior studies observed scaffolds via X-ray imaging which cannot distinguish

superficial bone formation from deep mineralized tissue. μCT images were generated and bone

formation was present on all sides of the scaffold after four weeks of exposure to osteogenic

induction media, as expected (Fig. 2.1A, B). Utilizing a cut plane, depth of mineralization was

also assessed (Fig. 2.1C). While there was limited mineralization in the center of the scaffold,

there was some bone formation beneath the scaffold surface. These findings indicated that three-

dimensional osteogenic differentiation of CPCs was sufficient for developing an osteochondral

tissue construct.
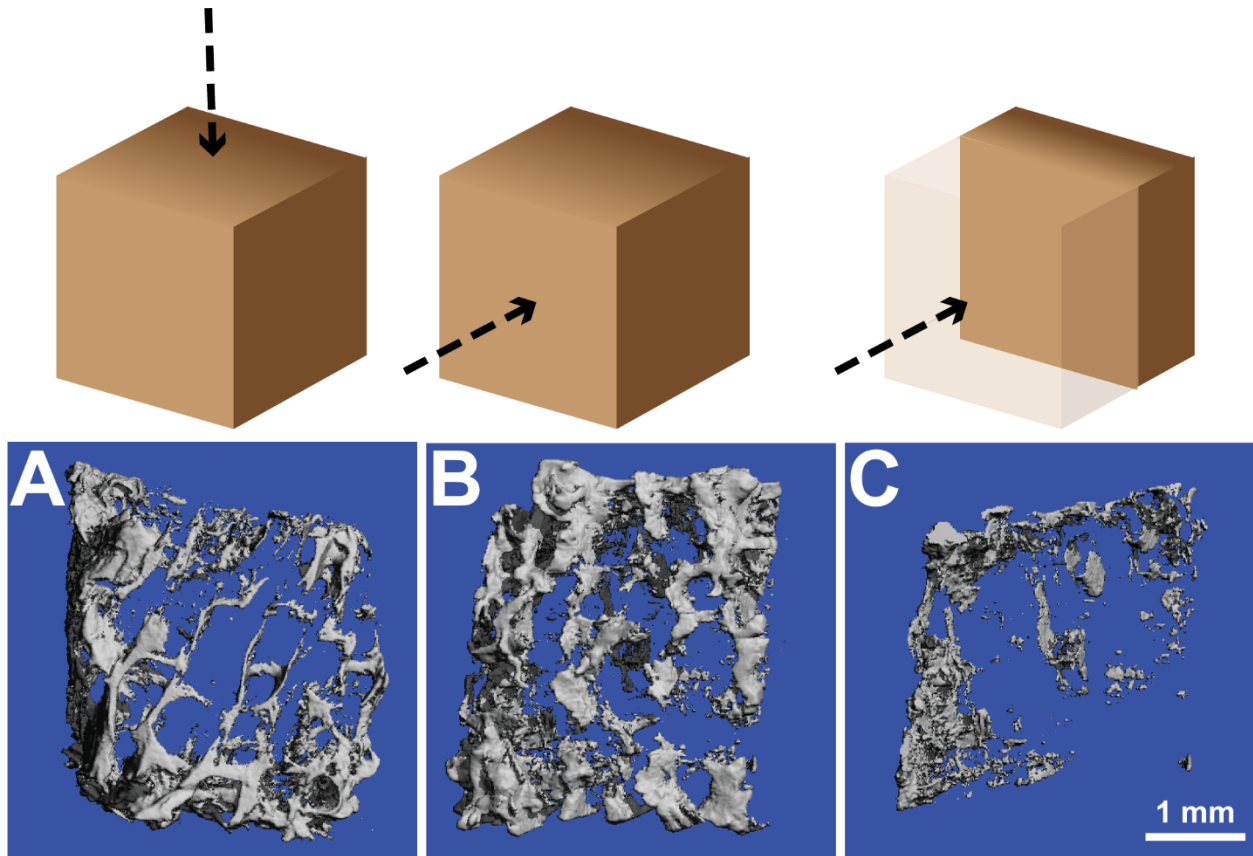
Fig. 2.1. CPC osteogenesis creates uniform mineralization at and below the surface of a three-dimensional demineralized bone scaffold. (A-C) µCT reconstructions of three-dimensional demineralized bone scaffolds seeded with CPCs after 28 days of osteogenic induction media from A) above, B) side view, and C) side cut-plane view.

2.4.2 Bi-culture system geographically restricts osteogenic differentiation

CPCs were seeded onto scaffolds using fibrin gel, then cultured them down a chondrogenic lineage for three weeks to fill the pores of the demineralized scaffold with fibrin gel and cartilaginous extracellular matrix. This filling was necessary to prevent media from flowing through the custom bi-culture system (Fig. 2.2A). CPC-laden, fibrin gel-filled scaffolds were then cultured in the bi-culture system with half of the scaffold cultured according to the validated osteogenic differentiation technique and half cultured in chondrogenic induction media. After three weeks, the bi-cultured scaffolds were collected for µCT analysis. A scaffold with no CPCs and no fibrin gel was scanned as a negative control (Fig. 2.2B, D). The CPC-laden, fibrin gel-filled scaffold had clear mineralization on only one surface (Fig. 2C, E). These results demonstrated proof-of-concept for the bi-culture system design.
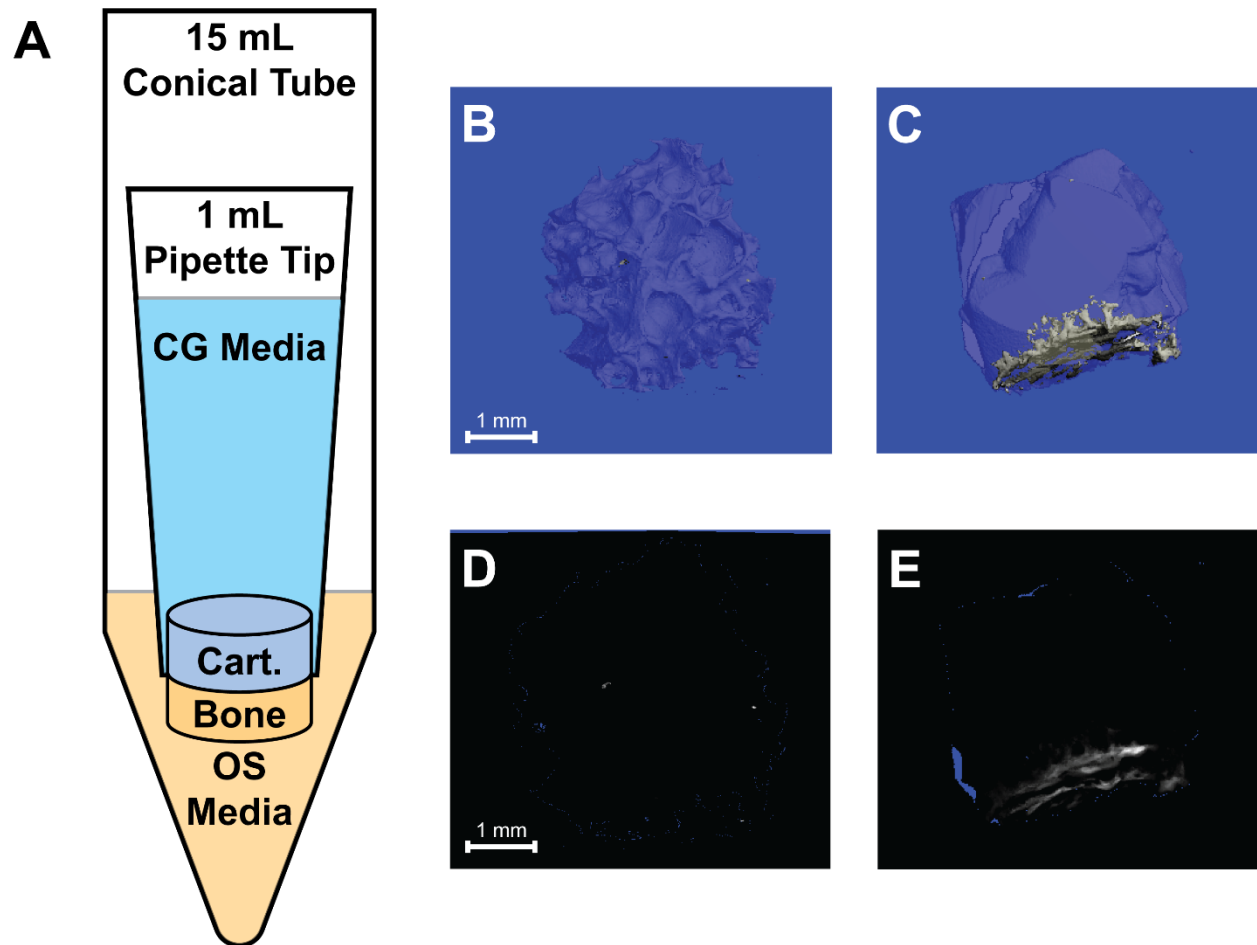
Fig 2.2. Osteogenic differentiation can be geographically restricted using a bi-culture system. A) Bi-culture system design indicating different compartments for chondrogenic (CG) and osteogenic (OS) medias to induce cartilage (Cart.) and bone formation on a three-dimensional scaffold. (B-C) Micro-computed tomography (μCT) three-dimensional reconstructions of B) negative control scaffold and C) bi-cultured scaffold. (D-E) X-ray radiographs of D) negative control scaffold and E) bi-cultured scaffold.

2.4.3 Failed Cartilage Progenitor Cell Three-Dimensional Scaffold Chondrogenesis

To validate the chondrogenic side of the bi-culture system, scaffolds were fixed and evaluated

using histological stains. Hematoxylin and Eosin (H&E) staining showed that there were very

few cells present in the chondrogenic half of the scaffold (Fig. 2.3A). Safranin-O (Saf-O)

staining showed a lack proteoglycan accumulation which would be indicated by red staining

(Fig. 2.3B), suggesting that no cartilage extracellular matrix accumulated in the scaffold. To

begin troubleshooting this issue, cell seeding studies were performed on three different

biomaterial scaffolds [demineralized bone, chitosan-gelatin cryogel, and poly (ε-caprolactone)]

with and without fibrin gel. Live/Dead staining indicated that the demineralized human bone scaffolds seeded in CPCs suspended in fibrin gel provided the best cell density and cell viability among the analyzed combinations of scaffolds and seeding techniques (Fig. 2.3C-H). These results suggested that cell density and cell viability should not have been the reason that chondrogenesis failed in the bi-culture system.
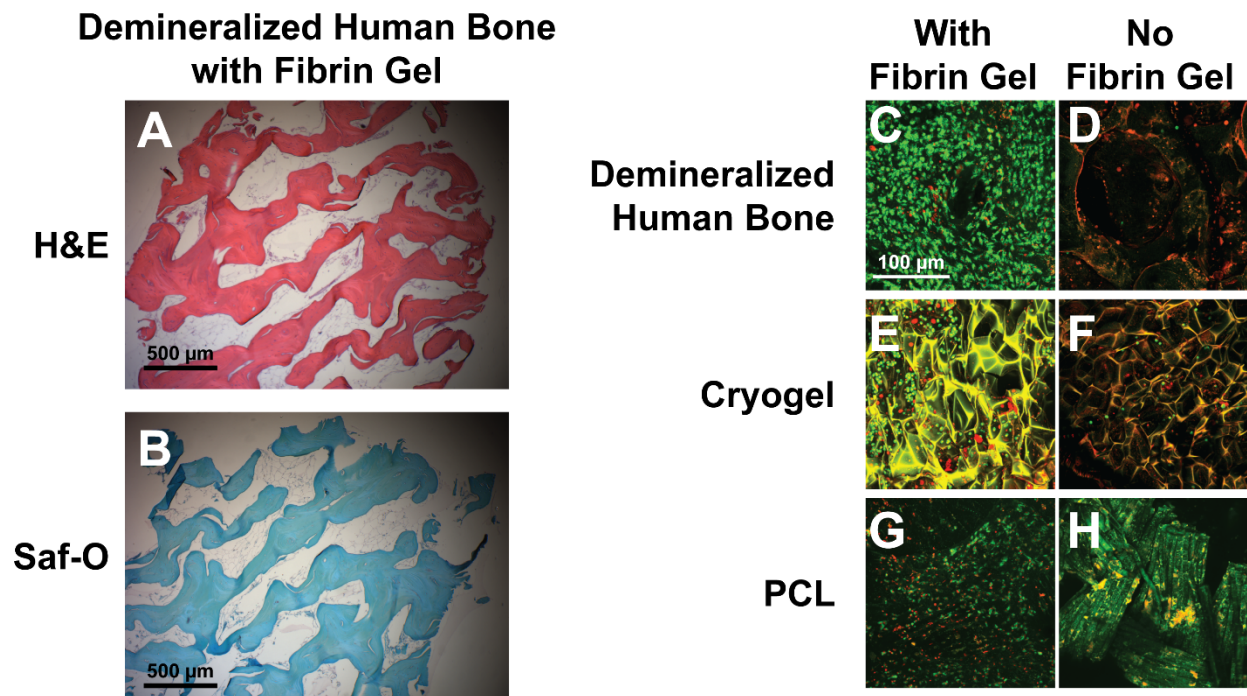
Figure 2.3. Failed chondrogenic differentiation in three-dimensional bone scaffolds is not due to insufficient cell density or cell viability. (A-B) Histological staining of the cartilage portion of the bi-cultured scaffold using A) H&E and B) Safranin-O (Saf-O) after three weeks of chondrogenic culture and three weeks of bi-culture. (C-H) Histological staining for cells that are alive (green) and dead (red) in demineralized human bone, chitosan-gelatin cryogel (Cryogel), or poly (ε-caprolactone) (PCL) scaffolds where cartilage progenitor cells were seeded with or without fibrin gel. Live/Dead staining was completed three days after seeding.

2.4.4 Cartilage Progenitor Cell Differentiation Multipotency Varies by Donor

Since cell viability and density did not seem to be the underlying cause for failed CPC chondrogenesis in three-dimensional human bone scaffolds, the chondrogenicity and, more broadly, multi-lineage differentiation capability of CPCs from multiple donors was tested. CPCs from several donors were tested in well-established culture conditions (monolayer for osteogenesis, micromass pellet for chondrogenesis). Our findings indicated that CPCs from some

donors were poor for both chondrogenic and osteogenic differentiation (Fig. 2.4A.i-A.iv), some

were good at only one lineage (Fig. 2.4B.i-C.iv), and some were good at both (Fig. 2.4Di-D.iv).

This suggested that perhaps the CPC line used in the bi-culture system was selected from a donor

that was well suited for osteogenesis but not chondrogenesis (Fig. 2.4C.i-C.iv). With this

information about donor variability, CPC multi-lineage differentiation testing was carried out

prior to experimental use for all future studies.
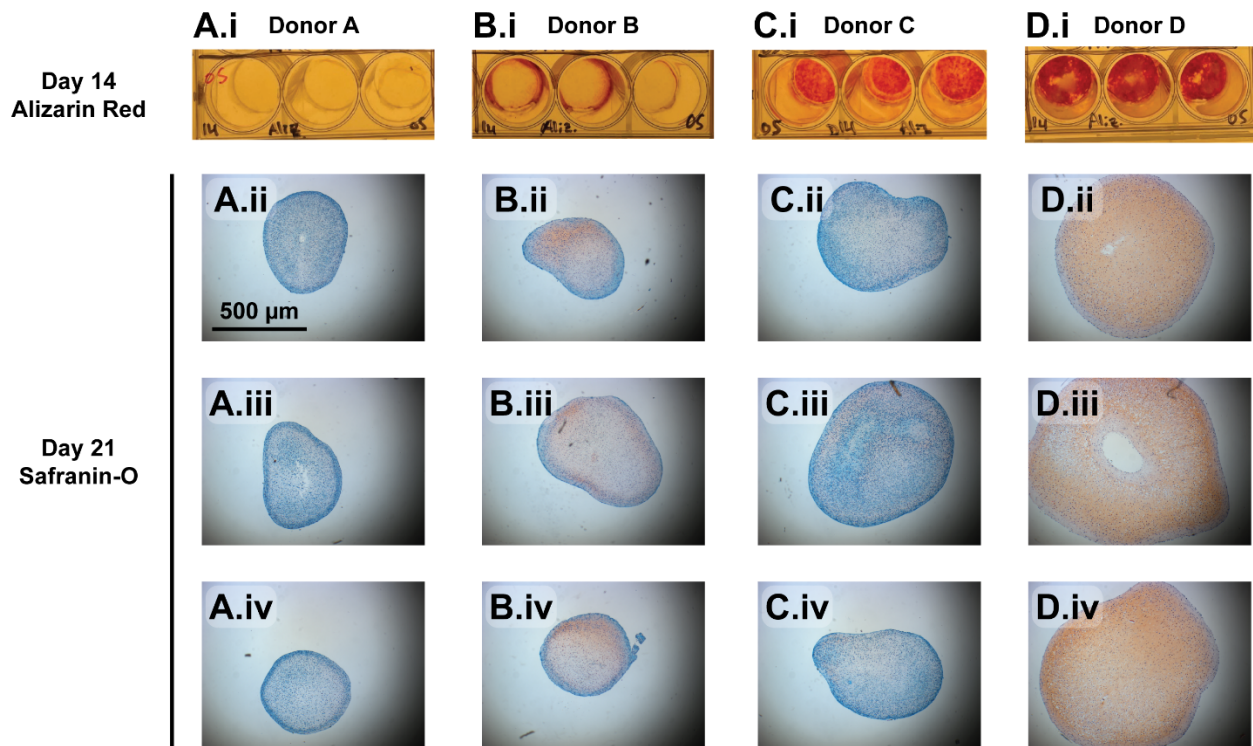
Fig. 2.4. Cartilage progenitor cells from different donors have variable potential for multi-lineage differentiation. (A.i-D.i) Day 14 alizarin red and (A.ii-D.iv) Day 21 safranin-O staining on cartilage progenitor cells from four different donors.

2.4.5 Chondrogenic cartilage progenitor cells do not form cartilage in three-dimensional scaffolds

Having tested the chondrogenic differentiation potential for CPCs from several donors, CPCs

from a donor with high chondrogenic potential were selected for a chondrogenic differentiation

in a three-dimensional scaffold using fibrin gel for seeding. After 21 days in chondrogenic

conditions, safranin-O staining showed small pockets of cartilage extracellular matrix

accumulation near the surface on the chondrogenic scaffolds (Fig. 2.5A-C). Multiple micromass

pellets were cultured concurrently to verify the chondrogenic potential of the cell line, and

safranin-O staining at the same time point showed consistent chondrogenic differentiation (2.5D-

E). While the presence of a small amount of cartilaginous matrix indicated some success, these

results showed that using CPCs with high chondrogenicity was still insufficient to produce a

uniform cartilage construct.
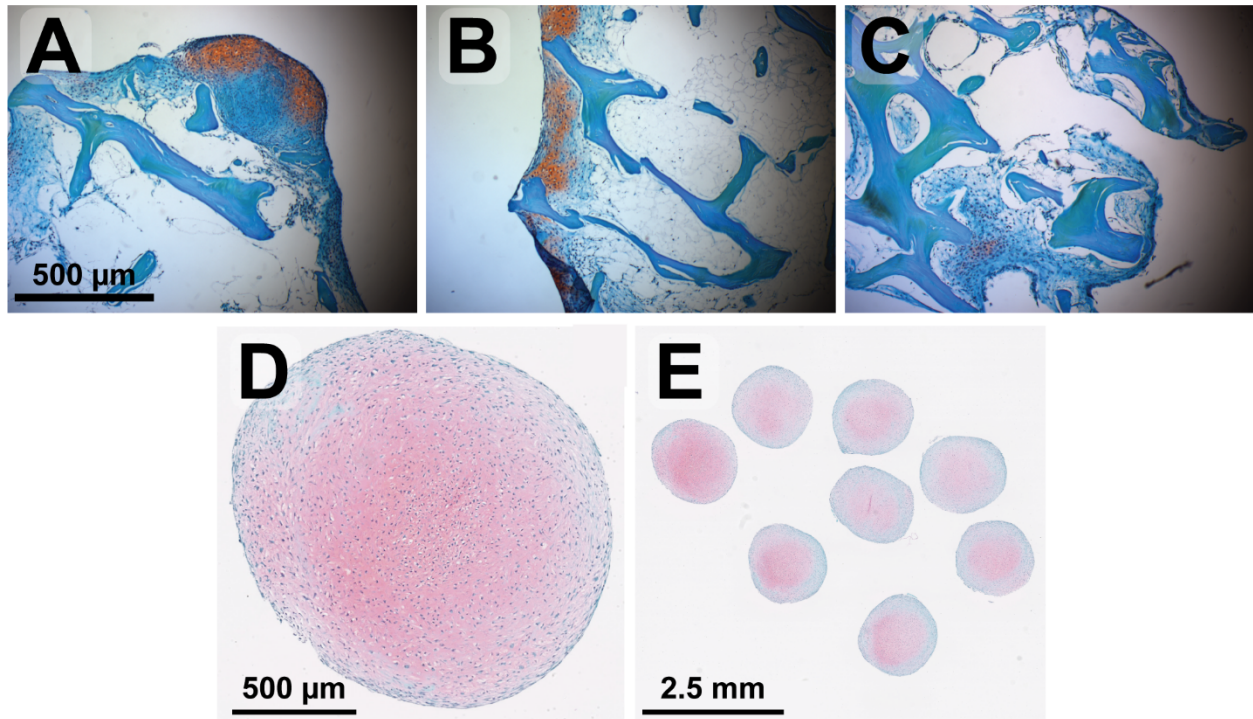
Fig. 2.5. Cartilage progenitor cell chondrogenesis is limited in three-dimensional scaffold even when using highly chondrogenic cells. (A-C) Small regions of proteoglycan-positive safranin-O staining near the surface of three different CPC-laden demineralized human bone scaffolds after 21 days of chondrogenic induction. (D-E) Day 21 safranin-O histology of micromass pellets made up of CPCs from the same donor as the cells used in the scaffolds.

2.5 Discussion

The bi-culture system designed in this project creates an opportunity to develop a fully integrated

osteochondral construct. The presence of mineralized matrix on only one side of the scaffold

demonstrates proof-of-concept for this design and can be built upon to cultivate a native-like

tissue construct. However, the inconsistency in CPC differentiation potential and inability of

CPCs to deposit cartilaginous matrix using this experimental design leave room for

improvement.

36

Others have established three-dimensional cartilage tissue constructs using CPCs. These constructs have been developed both with[8,34] and without[17,20] biomaterial scaffolds. Their culture techniques utilize higher cell density, biomimetic oxygen levels ("physoxia"), dynamic mechanical loading, and/or adenovirus-mediated over-expression of potent chondro-inductive genes. Future work in this bi-culture system should improve upon the cell seeding density and culture conditions for the chondrogenic compartment. Further, the bi-culture system design should be upgraded to include dynamic loading and modulation of media oxygenation during culture.

While we applied a DAF assay to select progenitor-like cells from a population including chondrocytes and CPCs, this approach did not produce a consistent population of multipotent cells. CPC studies often incorporate manual[14,21] or automated[35] clonal selection to isolate high proliferating cells which produce cells with more robust differentiation potential. While this means that there are fewer CPCs in the initial colony, their proliferative properties allow them to expand rapidly. Moreover, the expanded cell colony is highly homogenous and yields reproducible results. Further, this approach relies less on the donor tissue because there is a more stringent cell selection protocol in place. As cell surface markers on CPCs become better characterized[36], more efficient selection protocols should be developed to precisely identify and isolate these multipotent cells.

2.6 References

1   Barbero, A., Ploegert, S., Heberer, M. & Martin, I. Plasticity of clonal populations of dedifferentiated adult human articular chondrocytes. *Arthritis Rheum* **48**, 1315-1325 (2003). https://doi.org/10.1002/art.10950

2   Alsalameh, S., Amin, R., Gemba, T. & Lotz, M. Identification of mesenchymal progenitor cells in normal and osteoarthritic human articular cartilage. *Arthritis Rheum* **50**, 1522-1532 (2004). https://doi.org/10.1002/art.20269

3   Fickert, S., Fiedler, J. & Brenner, R. E. Identification of subpopulations with characteristics of mesenchymal progenitor cells from human osteoarthritic cartilage using triple staining for cell surface markers. *Arthritis Res Ther* **6**, R422-432 (2004). https://doi.org/10.1186/ar1210

4   Hiraoka, K., Grogan, S., Olee, T. & Lotz, M. Mesenchymal progenitor cells in adult human articular cartilage. *Biorheology* **43**, 447-454 (2006).

5   Grogan, S. P., Miyaki, S., Asahara, H., D'Lima, D. D. & Lotz, M. K. Mesenchymal progenitor cell markers in human articular cartilage: normal distribution and changes in osteoarthritis. *Arthritis Res Ther* **11**, R85 (2009). https://doi.org/10.1186/ar2719

6   Seol, D. *et al.* Chondrogenic progenitor cells respond to cartilage injury. *Arthritis Rheum* **64**, 3626-3637 (2012). https://doi.org/10.1002/art.34613

7   Koelling, S. *et al.* Migratory chondrogenic progenitor cells from repair tissue during the later stages of human osteoarthritis. *Cell Stem Cell* **4**, 324-335 (2009). https://doi.org/10.1016/j.stem.2009.01.015

8   Jiang, Y. *et al.* Human Cartilage-Derived Progenitor Cells From Committed Chondrocytes for Efficient Cartilage Repair and Regeneration. *Stem Cells Transl Med* **5**, 733-744 (2016). https://doi.org/10.5966/sctm.2015-0192

9   Grogan, S. P. *et al.* Identification of markers to characterize and sort human articular chondrocytes with enhanced in vitro chondrogenic capacity. *Arthritis Rheum* **56**, 586-595 (2007). https://doi.org/10.1002/art.22408

10   Jiang, Y. & Tuan, R. S. Origin and function of cartilage stem/progenitor cells in osteoarthritis. *Nat Rev Rheumatol* **11**, 206-212 (2015). https://doi.org/10.1038/nrrheum.2014.200

11   Rikkers, M., Korpershoek, J. V., Levato, R., Malda, J. & Vonk, L. A. The clinical potential of articular cartilage-derived progenitor cells: a systematic review. *NPJ Regen Med* **7**, 2 (2022). https://doi.org/10.1038/s41536-021-00203-6

12   Dowthwaite, G. P. *et al.* The surface of articular cartilage contains a progenitor cell population. *J Cell Sci* **117**, 889-897 (2004). https://doi.org/10.1242/jcs.00912

13   Jones, P. H. & Watt, F. M. Separation of human epidermal stem cells from transit amplifying cells on the basis of differences in integrin function and expression. *Cell* **73**, 713-724 (1993). https://doi.org/10.1016/0092-8674(93)90251-k

14   Williams, R. *et al.* Identification and clonal characterisation of a progenitor cell sub-population in normal human articular cartilage. *PloS One* **5**, e13246 (2010). https://doi.org/10.1371/journal.pone.0013246

15   Johnstone, B. *et al.* Tissue engineering for articular cartilage repair—the state of the art. *Eur Cell Mater* **25**, 248-267 (2013). https://doi.org/10.22203/ecm.v025a18

16   Dickhut, A. *et al.* Calcification or dedifferentiation: requirement to lock mesenchymal stem cells in a desired differentiation stage. *J Cell Physiol* **219**, 219-226 (2009). https://doi.org/10.1002/jcp.21673

17   Anderson, D. E., Markway, B. D., Bond, D., McCarthy, H. E. & Johnstone, B. Responses to altered oxygen tension are distinct between human stem cells of high and low chondrogenic capacity. *Stem Cell Res Ther* **7**, 154 (2016). https://doi.org/10.1186/s13287-016-0419-8

18   McCarthy, H. E., Bara, J. J., Brakspear, K., Singhrao, S. K. & Archer, C. W. The comparison of equine articular cartilage progenitor cells and bone marrow-derived stromal cells as potential cell sources for cartilage repair in the horse. *Vet J* **192**, 345-351 (2012). https://doi.org/10.1016/j.tvjl.2011.08.036

19   Schmidt, S. *et al.* Differential Production of Cartilage ECM in 3D Agarose Constructs by Equine Articular Cartilage Progenitor Cells and Mesenchymal Stromal Cells. *Int J Mol Sci* **21** (2020). https://doi.org/10.3390/ijms21197071

20   Levato, R. *et al.* The bio in the ink: cartilage regeneration with bioprintable hydrogels and articular cartilage-derived progenitor cells. *Acta Biomater* **61**, 41-53 (2017). https://doi.org/10.1016/j.actbio.2017.08.005

21   Anderson, D. E., Markway, B. D., Weekes, K. J., McCarthy, H. E. & Johnstone, B. Physioxia Promotes the Articular Chondrocyte-Like Phenotype in Human Chondroprogenitor-Derived Self-Organized Tissue. *Tissue Eng Part A* **24**, 264-274 (2018). https://doi.org/10.1089/ten.TEA.2016.0510

22   Loeser, R. F., Goldring, S. R., Scanzello, C. R. & Goldring, M. B. Osteoarthritis: a disease of the joint as an organ. *Arthritis Rheum* **64**, 1697-1707 (2012). https://doi.org/10.1002/art.34453

23   Andriolo, L., Merli, G., Filardo, G., Marcacci, M. & Kon, E. Failure of Autologous Chondrocyte Implantation. *Sports Med Arthrosc Rev* **25**, 10-18 (2017). https://doi.org/10.1097/JSA.0000000000000137

24   Solheim, E., Hegna, J. & Inderhaug, E. Long-term clinical follow-up of microfracture versus mosaicplasty in articular cartilage defects of medial femoral condyle. *Knee* **24**, 1402-1407 (2017). https://doi.org/10.1016/j.knee.2017.08.061

25   Zheng, H., Liu, J., Tycksen, E., Nunley, R. & McAlinden, A. MicroRNA-181a/b-1 over-expression enhances osteogenesis by modulating PTEN/PI3K/AKT signaling and mitochondrial metabolism. *Bone* **123**, 92-102 (2019). https://doi.org/10.1016/j.bone.2019.03.020

26   Zheng, H. *et al.* MicroRNA-138 Inhibits Osteogenic Differentiation and Mineralization of Human Dedifferentiated Chondrocytes by Regulating RhoC and the Actin Cytoskeleton. *JBMR Plus* **3**, e10071 (2019). https://doi.org/10.1002/jbm4.10071

27   Bell-Hensley, A., Zheng, H. & McAlinden, A. Modulation of MicroRNA Expression During In Vitro Chondrogenesis. *Methods Mol Biol* **2598**, 197-215 (2023). https://doi.org/10.1007/978-1-0716-2839-3_15

28   Hixon, K. R. *et al.* The calcification potential of cryogel scaffolds incorporated with various forms of hydroxyapatite for bone regeneration. *Biomed Mater* **12**, 025005 (2017). https://doi.org/10.1088/1748-605X/aa5d76

29   Kathuria, N., Tripathi, A., Kar, K. K. & Kumar, A. Synthesis and characterization of elastic and macroporous chitosan-gelatin cryogels for tissue engineering. *Acta Biomater* **5**, 406-418 (2009). https://doi.org/10.1016/j.actbio.2008.07.009

30   Valonen, P. K. *et al.* In vitro generation of mechanically functional cartilage grafts based on adult human stem cells and 3D-woven poly(epsilon-caprolactone) scaffolds. *Biomaterials* **31**, 2193-2200 (2010). https://doi.org/10.1016/j.biomaterials.2009.11.092

31   Moutos, F. T. & Guilak, F. Functional properties of cell-seeded three-dimensionally woven poly(epsilon-caprolactone) scaffolds for cartilage tissue engineering. *Tissue Eng Part A* **16**, 1291-1301 (2010). https://doi.org/10.1089/ten.TEA.2009.0480

32   Markway, B. D., Cho, H. & Johnstone, B. Hypoxia promotes redifferentiation and suppresses markers of hypertrophy and degeneration in both healthy and osteoarthritic chondrocytes. *Arthritis Res Ther* **15**, R92 (2013). https://doi.org/10.1186/ar4272

33   Johnstone, B. & Yoo, J. U. Autologous mesenchymal progenitor cells in articular cartilage repair. *Clin Orthop Relat Res*, S156-162 (1999). https://doi.org/10.1097/00003086-199910001-00017

34   Neumann, A. J. *et al.* Human Articular Cartilage Progenitor Cells Are Responsive to Mechanical Stimulation and Adenoviral-Mediated Overexpression of Bone-Morphogenetic Protein 2. *PloS One* **10**, e0136229 (2015). https://doi.org/10.1371/journal.pone.0136229

35   Mantripragada, V. P. *et al.* Progenitor cells from different zones of human cartilage and their correlation with histopathological osteoarthritis progression. *J Orthop Res* **36**, 1728-1738 (2018). https://doi.org/10.1002/jor.23829

36   Grandi, F. C. *et al.* Single-cell mass cytometry reveals cross-talk between inflammation-dampening and inflammation-amplifying cells in osteoarthritic cartilage. *Sci Adv* **6**, eaay5352 (2020). https://doi.org/10.1126/sciadv.aay5352

Chapter 3: MicroRNA-181a/b-1 Regulates Cartilage Progenitor Cell Chondrogenesis

This chapter has been adapted from a research article submitted to *Osteoarthritis and Cartilage Open* by Bell-Hensley *et al*.

3.1 Abstract

Articular cartilage serves a critical role in the skeleton, cushioning long bones and allowing joint articulation. For many reasons, this tissue is subject to degradation that leads to OA. Effective OA treatments that can enhance the anabolic/regenerative capacity of chondrocytes are needed. Studying processes of cartilage development may inform us of approaches to control chondrocyte differentiation and anabolism and, ultimately, how to effectively treat OA lesions. MicroRNAs are broad-acting epigenetic regulators known to affect many skeletal processes. Previous studies from our group identified differential expression of miR-181a-1 in human developing cartilage. The goal of this study was to determine how the entire miR-181a/b-1 cluster regulates *in vitro* chondrogenesis. We report that miR-181a/b-1 over-expression enhanced cartilage extracellular matrix production. Bulk RNA-Seq at Day 7 of chondrogenic pellet culture revealed upregulation of pro-chondrogenic genes such as *COL2A1*, *COL9A2/3*, *COL11A2*, *SNORC* and *MATN4*. Immunostaining of pellet tissue sections revealed that miR-181a/b-1 increased mature type II collagen and decreased expression of the chondroprogenitor type IIA collagen isoform, further indicating enhanced differentiation. Of the genes significantly downregulated by miR-181a/b-1, aquaporin-9 (*AQP9*) was the top hit which decreased in expression by over 14-fold. Our data suggested that *AQP9* was an indirect target of miR-181a/b-1 and that this membrane channel protein localized to the mitochondria in cartilage progenitor

cells. These studies demonstrate a pro-differentiation/anabolic function for miR-181a/b-1 during chondrogenesis that may be due, in part, to suppression of *AQP9*.

3.2 Introduction

A better understanding of processes regulating cartilage development and homeostasis can provide us with important information to better assess the pathological changes that occur during OA and develop new regenerative therapies. Formation of articular cartilage tissue involves a series of complex and highly orchestrated events, as does post-natal homeostatic maintenance of mature cartilage tissue. Epigenetic control of cartilage development and homeostasis has gained interest over recent years[1-3]. Among the epigenetic regulators that have important functions in skeletal biology are miRNAs.

While many miRNAs have been reported to regulate cartilage development and/or homeostasis, McAlinden *et al* was the first to profile miRNA expression in chondrocytes of the developing human embryonic limb[4]. Analysis of differentially expressed miRNAs revealed significant upregulation of miR-181a-1 in hypertrophic chondrocytes, suggesting that it may play an important role in chondrocyte differentiation and endochondral bone formation. The gene encoding miR-181a-1 is located on chromosome 1 near the gene encoding miR-181b-1. This miR-181a/b-1 cluster is co-transcribed *in vivo* and processed to form the mature functional strands, miR-181a-1-5p and miR-181b-1-5p[5,6].

To build on the miRNA profiling study by McAlinden *et al*[4], Zheng *et al* over-expressed the miR-181a/b-1 cluster in skeletal progenitor cells and demonstrated that it enhanced osteogenesis, in part, by increasing PI3K/AKT signaling and mitochondrial respiration[7]. It has also been reported that over-expressing miR-181a-5p mimics in mature chondrocytes has anti-anabolic/pro-catabolic effects[8] and that targeting miR-181a-5p with antagomirs can mitigate OA

symptoms[9]. However, the function of miR-181 family members in regulating chondrogenesis is unknown. The goal of this study was to determine how over-expressing miR-181a/b-1 in human skeletal progenitor cells affects chondrogenic differentiation. Our findings suggest that this miRNA cluster enhanced differentiation and extracellular matrix production. Analysis of bulk RNA-Seq data revealed a number of significantly down-regulated genes, the most down-regulated being the membrane channel protein aquaporin-9 (AQP9). These studies provide new information on the role of miR-181a/b-1 in regulating chondrogenesis and suggest a novel mechanism involving AQP9, of which there is currently very little known in the cartilage biology field.

3.3 Methods

3.3.1 Cartilage Progenitor Cell Isolation and Expansion

Cartilage progenitor cells (CPCs) were isolated and expanded as previously described in *Section 2.3.1* (Tissue Collection) and *Section 2.3.2* (Cartilage Progenitor Cell Isolation and Expansion). After frozen storage, CPCs were expanded in growth medium for at least 6 passages, until use in differentiation assays.

3.3.2 Lentivirus Generation

Human genomic pre-miR-181a-1 (NCBI Ref Seq: NR_029626.1), pre-miR-181b-1 (NCBI Ref Seq NR_029612.1) and intervening 61 nucleotide sequence was amplified by PCR (Table 3.1). The resulting miR-181a/b-1 amplicon was inserted into the pLemiR backbone (Addgene) using the Gibson Assembly Master Mix (New England Biolabs). Stocks of pLemir lentivirus expressing pre-miR-181a/b-1 or a non-silencing (NS) control RNA were prepared as previously described[7,10,11] and titered using the Lenti-X™ qRT-PCR Titration Kit (Takara Bio USA)

according to the manufacturer's instructions. Aliquots of pLemir lentivirus stocks were stored at -80°C and used within two freeze-thaw cycles.

3.3.3 Lentivirus Testing

Passage 5 CPCs were transduced with lentivirus containing either pre-miR-181a/b-1 (LV-181) or NS control RNA (LV-NS) at three different multiplicities of infection (MOIs) in growth medium containing 100 μg/mL protamine sulfate. LV-181 has a transduction efficiency roughly 40% lower than the LV-NS based on expression of the RFP reporter in the pLemir backbone (data not shown), so different MOIs were used for each virus during testing. The testing MOIs for LV-NS were 5,000, 10,000, and 20,000 while the testing MOIs for LV-181 were 3,000, 6,000, and 12,000. Transduced CPCs were cultured for seven days, then transduction efficiency and cell viability were evaluated using brightfield and fluorescent microscopes. After imaging, RNA was extracted for microRNA over-expression analysis.

3.3.4 Lentivirus Transduction

Passage 6 CPCs were transduced with LV-181 or LV-NS in growth medium containing 100 μg/mL protamine sulfate. Transduction MOI was determined for each cell line during lentivirus testing. Transduced CPCs were cultured for 3 days before being trypsinized for pellet formation. Cell viability was assessed using brightfield microscopy immediately before trypsinzing.

3.3.5 Chondrogenic Differentiation Assay

Transduced CPCs were trypsinized and resuspended as chondrogenic pellet cultures (3 x 10^5 cells/pellet) in chondrogenic induction medium in a physoxic environment (37°C, 5% O_2, 5% CO_2) as previously described in *Section 2.3.10* (Pellet Chondrogenic Differentiation Assay). The duration of the differentiation assay was extended to five weeks after histologically evaluating lentivirus-treated pellets after three, four, and five weeks (data not shown). There were only small histological differences between LV-NS and LV-181 pellets after three or four weeks, but

histological differences became apparent after five weeks. Non-transduced CPCs were also cultured in an identical differentiation assay as a cell line control.

3.3.6 RNA Isolation

On Days 7 and 35 of the chondrogenic differentiation assay, pellets were collected for RNA isolation. Pellets were pooled to collect sufficient RNA for RNA-sequencing and qPCR (Day 7; 8-10 pellets) or just qPCR (Day 35; 2-4 pellets). Pooled pellets were suspended in lysis buffer from Norgen BioTek's Total RNA Purification kit for 5 minutes, then flash frozen in liquid nitrogen. Frozen pellets were dissociated using a motorized pellet pestle (DWK Life Sciences GmbH). RNA was extracted from the dissociated pellets using Norgen BioTek's Total RNA Purification kit according to the manufacturer's instructions. Total RNA was quantified using a NanoDrop 2000 Spectrophotometer (Thermo Fisher) then stored at -80°C.

3.3.7 Quantitative Polymerase Chain Reaction

miR-181a-5p and miR-181b-5p were reverse-transcribed and quantified using the TaqMan primer/probe sets (Life Technologies Inc; Table 3.1) along with the TaqMan microRNA reverse transcription kit (Life Technologies Inc.) and TaqMan master mix with no UNG (Life Technologies Inc.)[11]. mRNAs were reverse transcribed using Superscript RT II (Life Technologies Inc.) and quantitative polymerase chain reaction (qPCR) was performed using PowerUp SYBR master mix (Life Technologies Inc.). PCR primer sequences are shown in Table 3.1. Fold changes were calculated using the $2^{-\Delta Ct}$ method using RNU44 as a reference small RNA or *PPIA* as a reference mRNA.

Table 3.1. Primer sequences and Life Technologies miRNA assay IDs used for vector cloning and quantitative PCR. Bolded sequence indicates miR-181a/b-5p binding site. Bolded and italicized sequence indicates mutated sequence within miR-181a/b-5p binding site.

Amplicon	Forward Primer	Reverse Primer
miR-181-a/b-1 Genomic	CTGGGGCACAGATAACCAATGT GATGTGGAGGTTTG	AGGGGCGGAATTTGCTACAACA GTAGGAAGGTG

miR-181a-5p	TaqMan miRNA assay ID 000480 (Life Technologies Inc.)	
miR-181b-5p	TaqMan miRNA assay ID 001098 (Life Technologies Inc.)	
RNU44	TaqMan miRNA assay ID 001094 (Life Technologies Inc.)	
PPIA	TCCTGGCATCTTGTCCATG	CCATCCAACCACTCAGTCTTG
COL2A1	GGCAATAGCAGGTTCACGTACA	CGATAACAGTCTTGCCCCACTT
AQP9	GTGAGGACCACAACAGGTAGG	GCCACATCCAAGGACAATCAAG
AQP9 3'-UTR WT	CTAGCGGGAAGATAAGTTGAGTTGTCCAAGAGCACACTGAAAGT**TGAATGT**TATCTAATGCATTCCTCTACCTTTCAGAAGATCAGTAGCTGGCTG	TCGACAGCCAGCTACTGATCTTCTGAAAGGTAGAGGAATGCATTAGTA**ACATTCA**ACTTTCAGTGTGCTCTTGGACAACTCAACTTATCTTCCCG
AQP9 3'-UTR MUT	CTAGCGGGAAGATAAGTTGAGTTGTCCAAGAGCACACTGAAAGTT*ACC*TGTTATCTAATGCATTCCTCTACCTTTCAGAAGATCAGTAGCTGGCTG	TCGACAGCCAGCTACTGATCTTCTGAAAGGTAGAGGAATGCATTAGTA**AC*AGGTA***ACTTTCAGTGTGCTCTTGGACAACTCAACTTATCTTCCCG

3.3.8 Histology and Immunofluorescence

After 35 days, pellets were fixed in 10% neutral-buffered formalin and embedded in paraffin for histological evaluation. Paraffin-embedded pellets were sectioned at a 10 µm thickness and mounted on glass histology slides. Safranin-O staining was carried out on deparaffinized slides with Weigert's Hematoxylin (1.5 minutes), 0.2% Fast Green (2 minutes), and 0.1% Safranin O (6 minutes). Samples were dehydrated and coverslips were mounted using CytoSeal XYL (Thermo Fisher). For immunofluorescent staining, deparaffinized sections were treated with Proteinase K (10 µg/mL in 10 mM Tris-HCl, pH 7.5) for 20 minutes at 37°C (COLII and COLIIA) or sodium citrate (10 mM in 0.05% Tween 20, pH 6.0) for 10 minutes at 90°C (AQP9). Sections were rinsed, blocked, then incubated overnight at 4°C with the following primary antibodies: COLII[12] (1:200 dilution; a gift from Dr. David Eyre, University of Washington, Seattle), COLIIA[12] (1:200 dilution; a gift from Dr. Linda Sandell, Washington University, St. Louis), AQP9[13] (1:50 dilution; Alpha Diagnostics International Cat. No. #AQP91-A). Sections were incubated with species-specific secondary antibodies (1:200 dilution) that were conjugated to Alexa fluorescent dyes (Invitrogen: goat anti-rabbit Alexa 488; goat anti-rat Alexa 594) for 1 hour at room

temperature. Sections were rinsed and then coverslipped using DAPI mounting medium

(Electron Microscopy Sciences). Brightfield and fluorescent images were taken on a whole slide

imaging system (Hamamatsu Photonics Nanozoomer 2.0-HT System) using a 20X magnification

lens or an inverted confocal microscope (Leica DMi8) using a 63X magnification lens.

3.3.9 Quantitative assessment of histology and immunofluorescence images

Whole slide images of the safranin-O and immunostained pellet tissue sections were imported

into ImageJ software for analysis. Total cross-sectional area was quantified by converting the

safranin-O staining image to an 8-bit image and using the ImageJ "Threshold" tool. The

safranin-O positive area was selected by using a color threshold with the hue filter set to 40-210

with pass option turned off, the saturation filter set to 10-255 with pass option turned on, and the

brightness filter set to 110-255 with pass option turned on. The COLII positive area was selected

on the fluorescent image only the green COLII channel selected, using only a brightness filter set

to 50-254 with pass option turned on. Similarly, the COLIIA positive area was selected on the

fluorescent image only the red COLIIA channel selected, using only a brightness filter set to

140-254 with pass option turned on. The positive staining area for each of the safranin-O, COLII,

and COLIIA stains was divided by the total cross-sectional area.

3.3.10 Bulk RNA sequencing and pathway analysis

Day 7 RNA from four independent cell lines (transduced with LV-NS or LV-181) with adequate

Day 7 microRNA over-expression and consistent Day 35 histology and immunofluorescence

staining were submitted for bulk RNA-Sequencing. Samples were prepared according to library

kit manufacturer's protocol, indexed, pooled, and sequenced on an Illumina NovaSeq X Plus.

Basecalls and demultiplexing were performed with Illumina's DRAGEN and BCLconvert

version 4.2.4 software. RNA-Seq reads were then aligned to the Ensembl release 101 primary

assembly with STAR version 2.7.9a[14]. Gene counts were derived from the number of uniquely

aligned unambiguous reads by Subread:featureCount version 2.0.3[15]. All gene counts were then

imported into the R/Bioconductor package EdgeR and TMM normalization size factors were

calculated to adjust for samples for differences in library size. The TMM size factors and the

matrix of counts were then imported into the R/Bioconductor package Limma[16]. Weighted

likelihoods based on the observed mean-variance relationship of every gene and sample were

then calculated for all samples and the count matrix was transformed to moderated log 2 counts-

per-million with Limma's voomWithQualityWeights[17]. The performance of all genes was

assessed with plots of the residual standard deviation of every gene to their average log-count

with a robustly fitted trend line of the residuals. Differential expression analysis was then

performed to analyze for differences between conditions and the results were filtered for only

those genes with Benjamini-Hochberg false-discovery rate adjusted p-values less than or equal to

0.05. For each contrast extracted with Limma, global perturbations in known Gene Ontology

(GO) terms and MSigDB Reactome pathways were detected using the R/Bioconductor package

GAGE (to test for changes in expression of the reported log 2 fold-changes reported by Limma

in each term versus the background log 2 fold-changes of all genes found outside the respective

term. Raw and processed data from this study has been uploaded to the GEO depository and

assigned the accession code: GSE262978.

3.3.11 MicroRNA Target Prediction

A search for predicted miR-181a/b-5p target mRNAs was performed using the TargetScan

database (http://www.targetscan.org/) and the miRanda algorithm[18,19].

3.3.12 Luciferase Assay

Human AQP9 3'-UTR wild-type (WT) and mutant (MUT) oligonucleotide sequences (Table 3.1)

were cloned into the pmirGLO Dual-Luciferase miRNA Target Expression Vector (Promega).

These plasmids were transfected into human embryonic kidney cell line 293 (HEK293) cells

transduced with LV-181 or LV-NS. Cells were incubated at 37°C for 48 hours, then luciferase

activity was assessed with the Dual-Glo® Luciferase Assay System (Promega) according to the

manufacturer's instructions on an Agilent BioTek Cytation 5 microplate reader.

3.3.13 MitoTracker™ Staining

Passage 6 CPCs were treated with 100 nM MitoTracker™ Green (Thermo Fisher), fixed, and

permeabilized according to the manufacturer's instructions. Permeabilized cells were co-stained

with AQP9[13] (1:50 dilution) as described in *Section 3.3.8* (Histology and Immunofluorescence).

Slides were imaged on an inverted confocal microscope (Leica DMi8) using a 63X

magnification lens.

3.3.14 Statistical Analysis

All experiments were carried out in triplicate with CPCs derived from 3-4 independent biological

replicates. Data are presented as mean ± SD and statistical comparisons were made using paired

t-tests with pairing between CPCs expanded from the same donor, except for RNA expression

data which was compared using ratio paired t-tests to better assess proportional differences in

fold change. Probability values were considered statistically significant at $p \leq 0.05$.

3.4 Results

3.4.1 miR-181a/b-1 over-expression promotes chondrogenic differentiation

Transduced passage 7 CPCs were cultured as three-dimensional micromass pellets in

chondrogenic induction media for 35 days. We first confirmed over-expression of miR-181a/b-1

functional strands for the duration of the experiment (Fig. 3.1A, B). Pellet cultures were

collected for histology after 35 days in chondrogenic induction media and stained for cartilage

extracellular matrix proteins to assess the impact of lentiviral-mediated over-expression of miR-

181a/b-1 (LV-181) on chondrogenic differentiation. Proteoglycan content was assessed using

Safranin-O/Fast Green F staining (Fig. 3.1C, D; Appendix A). Quantitative analysis of safranin-O positive area fraction showed a significant increase in LV-181 pellets (Fig. 3.1E). Collagen composition was evaluated by immunolocalization of mature type II collagen fibers (COLII; Fig. 3.1F, G; Appendix B) as well as type IIA procollagen, the COL2A1 isoform expressed by chondroprogenitor cells (COLIIA; Fig. 3.1I, J; Appendix C). The COLIIA antibody recognizes the "IIA" exon 2-encoded cysteine rich domain in the amino propepetide of type IIA procollagen[20]. Analysis of immunostained images showed a significant increase in COLII positive area fraction in CPCs treated with LV-181 (Fig. 3.1H). Conversely, COLIIA area fraction was reduced in LV-181 pellets, though CPCs from one donor had minimal COLIIA expression in the control group and COLIIA expression appeared to increase in LV-181 pellets (Fig. 3.1K). In summary, miR-181a/b-1 over-expression appeared to promote a mature chondrocyte phenotype as indicated by enhanced proteoglycan and type II collagen deposition and reduction of the "chondroprogenitor" IIA isoform of type II collagen.
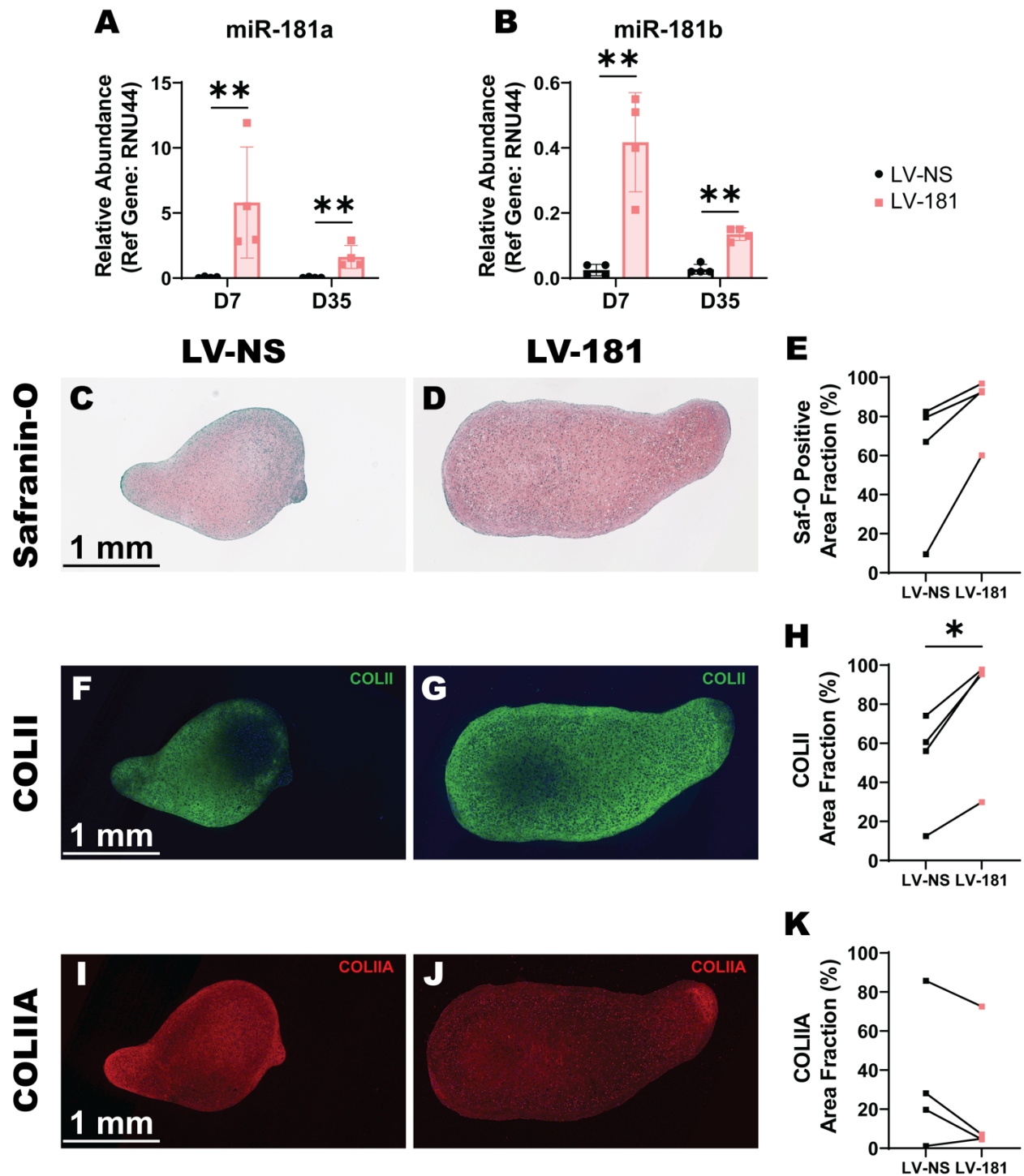
Fig. 3.1. Chondrogenic differentiation enhanced by miR-181a/b-1 over-expression. A,B) Relative abundance of (A) miR-181a-5p and (B) miR-181b-5p increased following lentiviral over-expression of the miR-181a/b-1 cluster (LV-181) after 7 and 35 days. C-K) Representative images and quantitative analysis of Safranin-O histology (Saf-O; C-E) and immunostaining for type II collagen (COLII; F-H) and type IIA pro-collagen (COLIIA; I-K). Immunostaining and quantitative analysis performed on pellet cultures after 35 days of chondrogenic induction. Positive staining was quantified as a percentage of the total cross-sectional area for quantitative analyses (E, H, K). * p < 0.05, ** p < 0.01. *n* = 4 CPC lines from independent donors. For miRNA expression analysis, RNA was pooled from 7-10 pellets (Day 7) or 2-4 pellets (Day 35). For histology and immunostaining, each dot is the average for 3-4

52

pellets for CPCs from a single donor. Abbreviations: LV-NS lentivirus encoding non-silencing miRNA sequence, LV-181 lentivirus encoding pre-miR-181a/b-1, Saf-O Safranin-O, COLII type II collagen, COLIIA type IIA pro-collagen. For full Safranin-O, COLII, and COLIIA staining results, see Appendix A, Appendix B, and Appendix C, respectively.

3.4.2 miR-181a/b-1 over-expression promotes cartilage anabolism

To determine the mechanism by which miR-181a/b-1 modulates chondrogenesis, bulk RNA-Sequencing (RNA-Seq) and pathway analysis were carried out on Day 7 RNA. Raw data files can be accessed online at the GEO repository under accession code GSE262978. Focusing only on protein-coding genes, there were 75 significantly differentially expressed genes with a Benjamini-Hochberg false-discovery rate adjusted p-value ≤ 0.05 and Log_2(Fold Change) ≥ 2 (Fig. 3.2A; Appendix D & E). Among the most significantly upregulated genes were several markers associated with the mature chondrocyte phenotype and cartilage anabolism including *COL2A1*, *COL9A2/3*, *SNORC*, *COL11A2*, *MATN4*, and *CSPG4* (Fig. 3.2A; Appendix D). To confirm RNA-Seq results, over-expression of the top upregulated gene, *COL2A1*, was confirmed via qPCR on Day 7 RNA (Fig. 3.2B). Further, *COL2A1* upregulation was sustained through Day 35 of chondrogenic induction (Fig. 3.2B). Moreover, GO biological processes upregulated by LV-181 included cartilage anabolic pathways such as *skeletal system development*, *extracellular structure organization*, and *cartilage development* (Fig. 3.2C). In addition, Reactome biological pathways upregulated in the LV-181 group included *collagen biosynthesis and modifying enzymes*, *collagen formation*, a*ssembly of collagen fibrils and other multimeric structures*, and *collagen chain trimerization* pathways (Fig. 3.3; Appendix F). These findings support a role for miR-181a/b-1 in promoting cartilage anabolism and extracellular matrix formation.
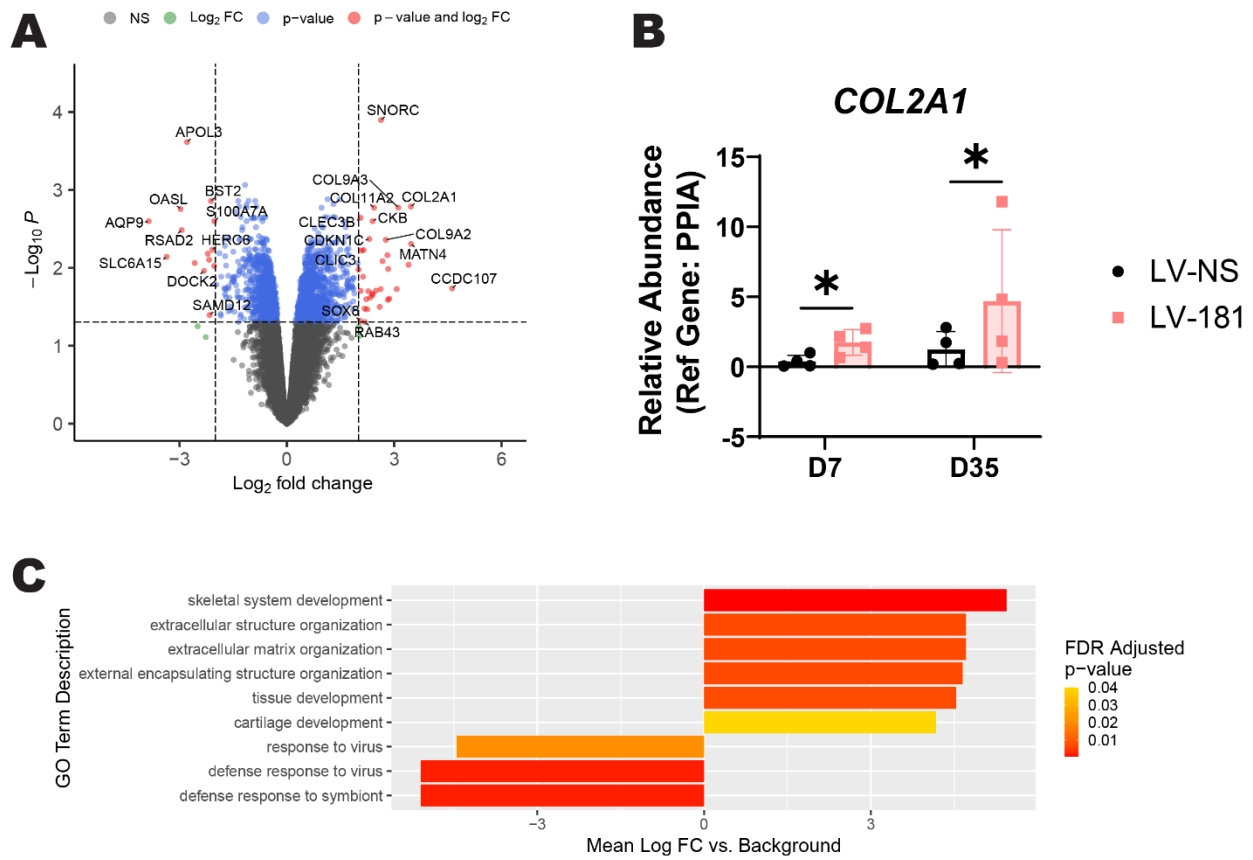
Fig. 3.2. Differentially expressed genes following miR-181a/b-1 over-expression. A) Volcano plot showing differentially expressed genes in CPCs after 7 days of chondrogenic induction following miR-181a/b-1 over-expression. P-values are adjusted for Benjamini-Hochberg false discovery rate (FDR). B) qPCR analysis of type II collagen RNA (COL2A1) expression at days 7 and 35 of chondrogenic induction. C) Significantly perturbed GO biological processes at Day 7 of CPC chondrogenesis following miR-181a/b-1 over-expression. * $p \leq 0.05$. n = 4 CPC lines from independent donors; RNA was pooled from 7-10 pellets (Day 7) or 2-4 pellets (Day 35). For full list of upregulated genes, see Appendix D. For full list of downregulated genes, see Appendix E.
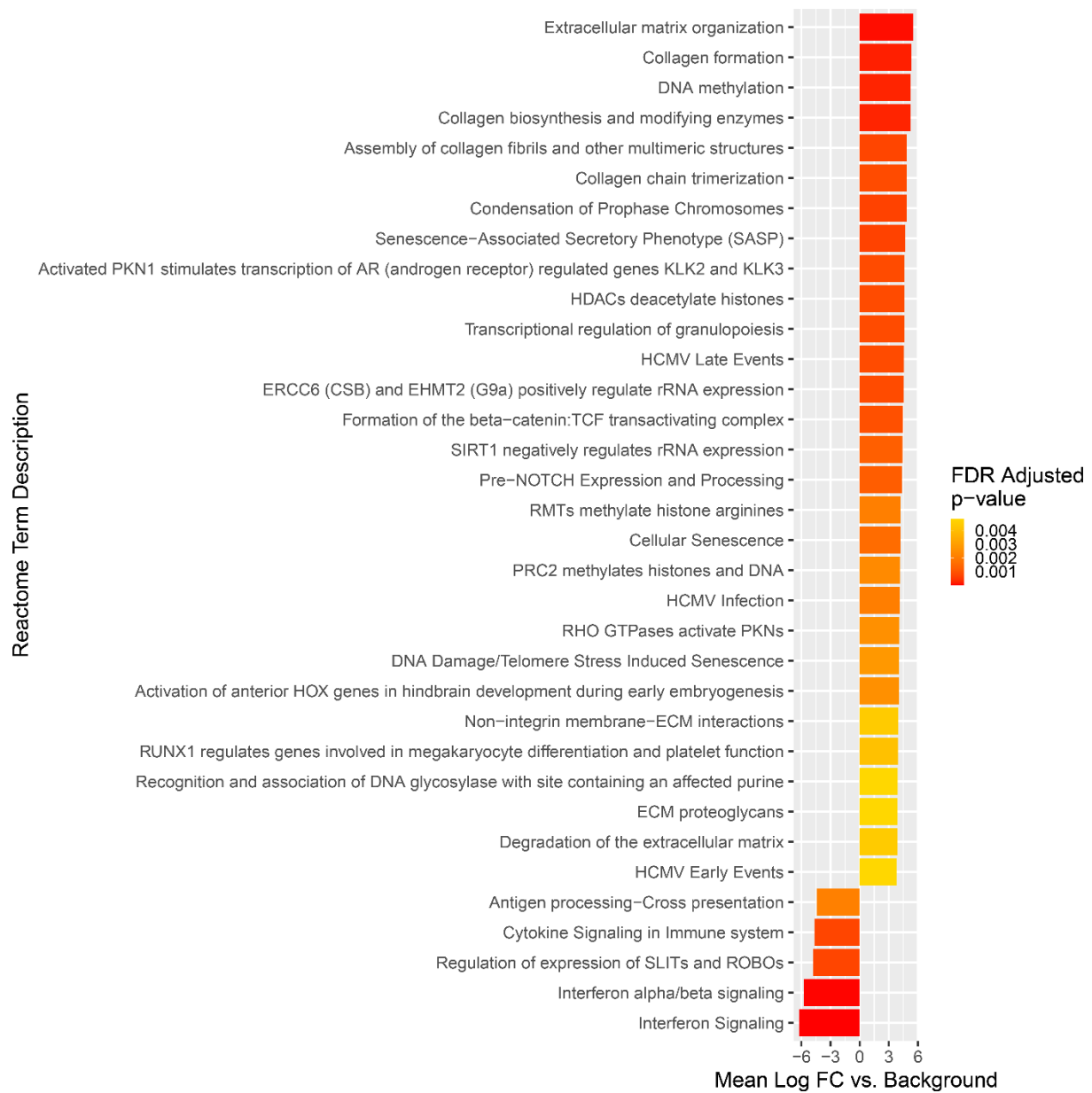
Fig. 3.3. Top significantly perturbed Reactome biological pathways at Day 7 of CPC chondrogenesis following miR-181a/b-1 over-expression. For full list of perturbed Reactome pathways, see Appendix F.

3.4.3 miR-181a/b-1 downregulates a number of genes, including potential target genes

RNA-Seq analysis also revealed several significantly down-regulated genes in response to miR-181a/b-1 over-expression during chondrogenesis (Fig. 3.2A; Appendix E). Some of these down-regulated genes were confirmed direct targets of miR-181a/b, such as *CBX7*[21,22], *PTPN22*[23], and *TGFBR1*[24]. An algorithm called MiRanda[19] was used to score miRNA-mRNA interactions for all

protein-coding genes detected in the RNA-Seq readout (Fig. 3.4A). This algorithm provided a

mathematical method for predicting miRNA targets based on local alignment, evolutionary

conservation, and miRNA:mRNA interaction folding energy[19]. A general miRNA target

prediction threshold used for the MiRanda algorithm is MiRanda Score ≥ 140[25]. Several targets

of miR-181a/b-5p that have been confirmed *in vitro* generated MiRanda scores ≥ 140 with

TGFBR1[24] being the highest with a score of 147. Interestingly, the most downregulated gene in

the RNA-Seq readout, aquaporin-9 (*AQP9*), had a MiRanda score of 161 for miR-181a/b-5p

(Fig. 3.4A). Downregulation of *AQP9* was confirmed via qPCR in the same Day 7 RNA isolates

(Fig. 3.4B). These findings suggest that downregulation of AQP9 may be one mechanism by

which miR-181a/b-1 modulates chondrogenesis and that this miRNA cluster may have directly

targeted and suppressed *AQP9*.
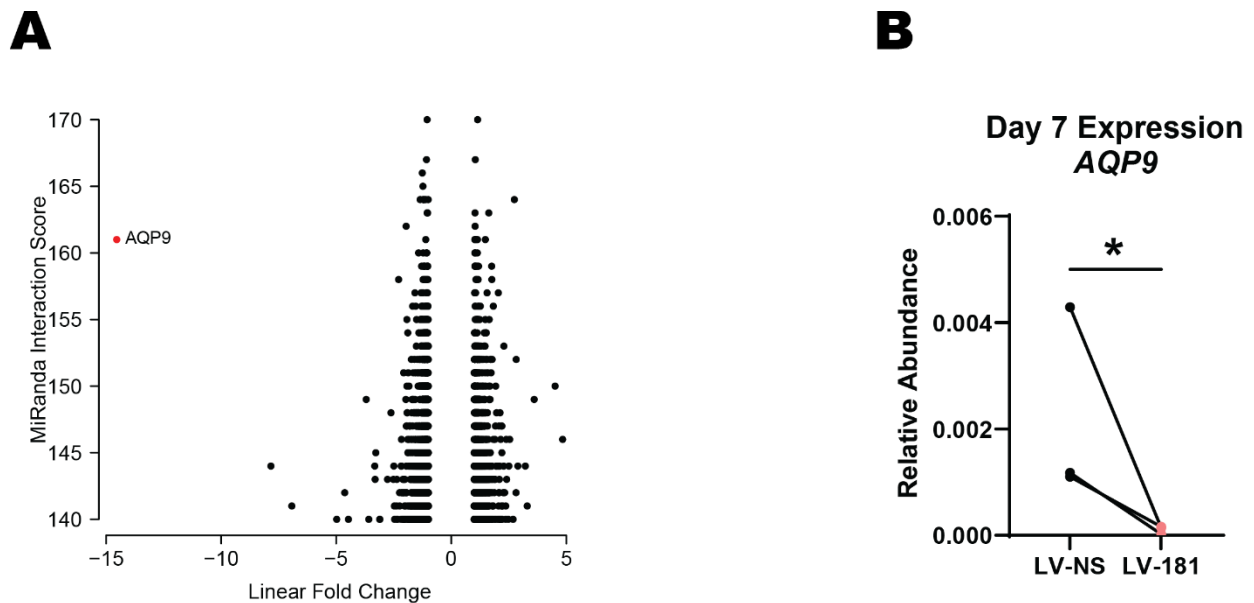
Fig. 3.4. Aquaporin-9 is a predicted target of miR-181a/b-1 and is downregulated by miR-181a/b-1 over-expression in TGF-β-induced chondrogenesis. A) Predicted targets of miR-181a/b-5p based on MiRanda interaction scoring algorithm compared to their linear fold change. B) qPCR analysis of aquaporin-9 RNA (*AQP9*) expression at Day 7 of chondrogenic induction. * $p < 0.05$. *n* = 3-4 CPC lines from independent donors. RNA was pooled from 7-10 pellets for RNA-Seq and qPCR analyses.

3.4.4 *AQP9* is an indirect target of miR-181a/b-1

To determine if miR-181a/b-5p directly targets *AQP9*, a dual luciferase reporter assay was

carried out using wild-type (WT) or mutated (MUT) sequences from the predicted binding site in

the 3' UTR of *AQP9* (Fig. 3.5A). HEK cells were transduced with LV-NS or LV-181 at three

different MOIs, treated with puromycin to select for transduced cells, then transfected with the

WT or MUT plasmid. When luciferase activity was evaluated, the ratio of Firefly luminosity to

Renilla luminosity was unchanged by LV-181 treatment (Fig. 3.5B), indicating that *AQP9* was

not a direct target of miR-181a/b.
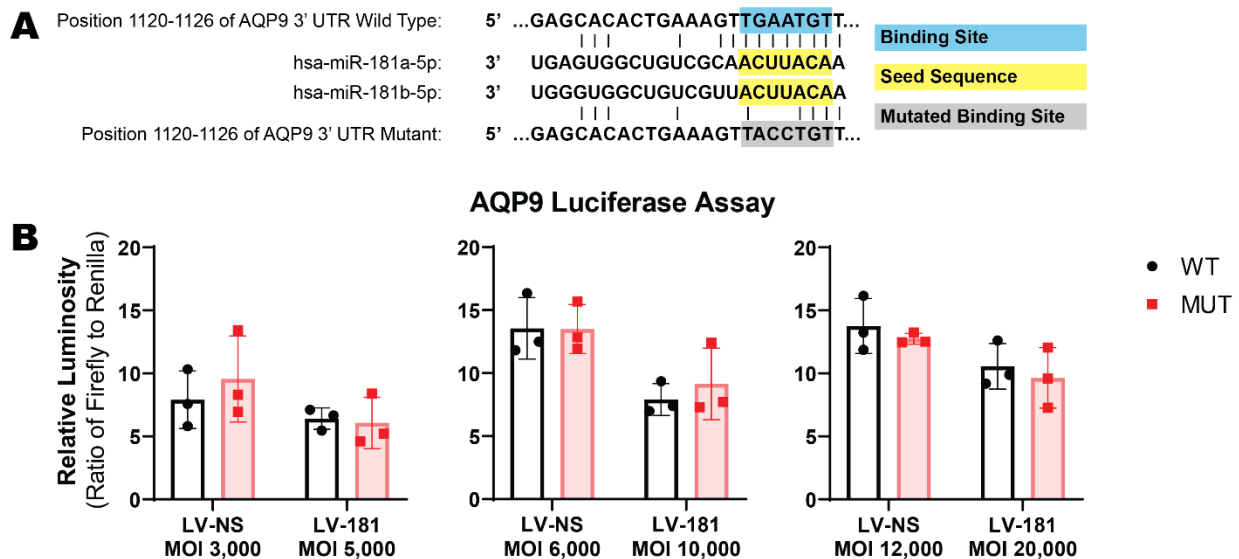
Fig. 3.5. Aquaporin-9 is not a direct target of miR-181a/b-1. A) Construct sequences used for the reporter luciferase assay with wild-type (WT) and mutated (MUT) sequences and the associated miR-181a/b-5p seed sequences. B) Results of reporter luciferase assay in HEK cells using 3 different MOIs per lentivirus. *n* = 3 biological replicates of HEK293T cells.

3.4.5 Aquaporin-9 expression is downregulated during chondrogenic differentiation

To assess *AQP9* expression during chondrogenesis, we evaluated a publicly available bulk RNA-

Seq dataset from Huynh *et al* describing the transcriptome of MSCs over a 21-day

chondrogenesis assay (GEO accession: GSE109503)[26]. In the RNA-Seq time course, *AQP9* was

expressed early in MSC chondrogenic differentiation and decreased over time (Fig. 3.6A). The

chondrogenic assay performed by Huynh *et al* used an identical media recipe to the one used in

our assay despite using a slightly larger pellet size (500,000 cells/pellet), a different progenitor

cell source (passage 4 MSCs), and a normoxic incubation environment (~20% O_2). Despite some

methodological differences, their time course showed that *AQP9* was expressed highly from Day

0 to Day 3 and then gradually decreased to negligible levels by Day 21. Similarly, qPCR

evaluation of *AQP9* expression during our CPC chondrogenesis assay showed a decrease

between Day 7 and Day 35, except in cell lines with endogenously low baseline *AQP9*

expression (Fig. 3.6B). Moreover, *AQP9* expression was significantly lower in the LV-181 group

at Day 7 and Day 35. In summary, *AQP9* expression progressively decreased during *in vitro*

chondrogenesis, and it was further suppressed by miR-181a/b-1 over-expression, but not due to

direct targeting.
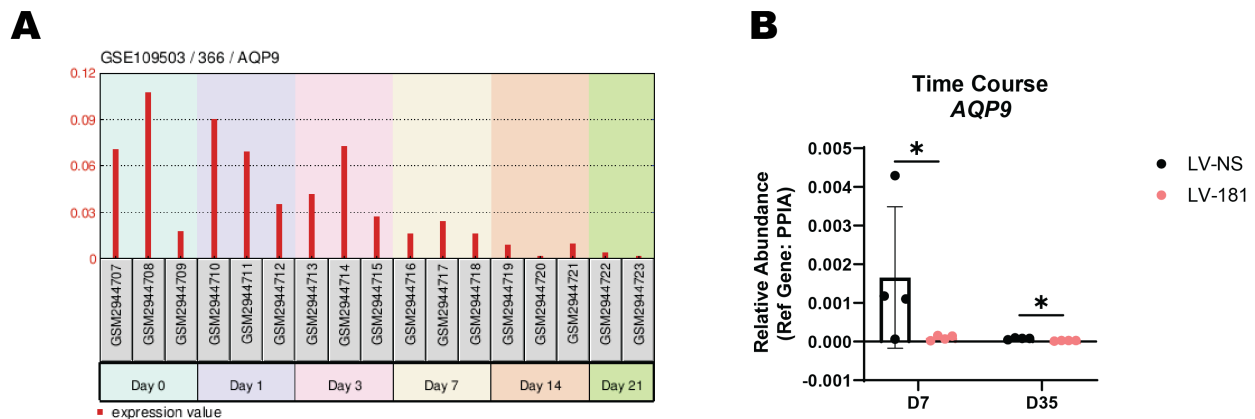
Fig. 3.6. Aquaporin-9 is downregulated during chondrogenesis. A) Expression pattern of *AQP9* in human MSC chondrogenesis (Data retrieved from GEO accession GSE109503)[26]. B) qPCR analysis of aquaporin-9 RNA (*AQP9*) expression at days 7 and 35 of chondrogenic induction. * $p < 0.05$. $n = 4$ CPC lines from independent donors; each CPC line had RNA pooled from 7-10 pellets (Day 7) or 2-4 pellets (Day 35).

3.4.6 Aquaporin-9 is expressed on the mitochondrial membrane in cartilage progenitor cells

While aquaporins are most commonly expressed on the cell membrane[27], there is evidence that

AQP9 is also expressed on the inner mitochondrial membrane[13,28]. We carried out

immunostaining to analyze AQP9 protein localization in chondrocytes within cartilage pellet

tissue sections compared to localization in positive control tissue (mouse liver tissue from wild

type C57BL/6 mice). Our data showed that Aqp9 localized to the cell membrane in liver cells (Fig. 3.7A), as expected[27], whereas in chondrocytes, AQP9 was expressed intracellularly (Fig. 3.7B). We also quantified AQP9 protein expression in Day 35 cartilage pellets but did not observe notable differences in expression levels between LV-NS and LV-181 pellets (Appendix G). To further explore if AQP9 localized to the mitochondrial membrane, we co-stained CPCs in monolayer with MitoTracker Green and AQP9 antibodies (Fig. 3.7C). Our findings suggest that, in chondro-progenitor cells, AQP9 expression may co-localize with the mitochondria.
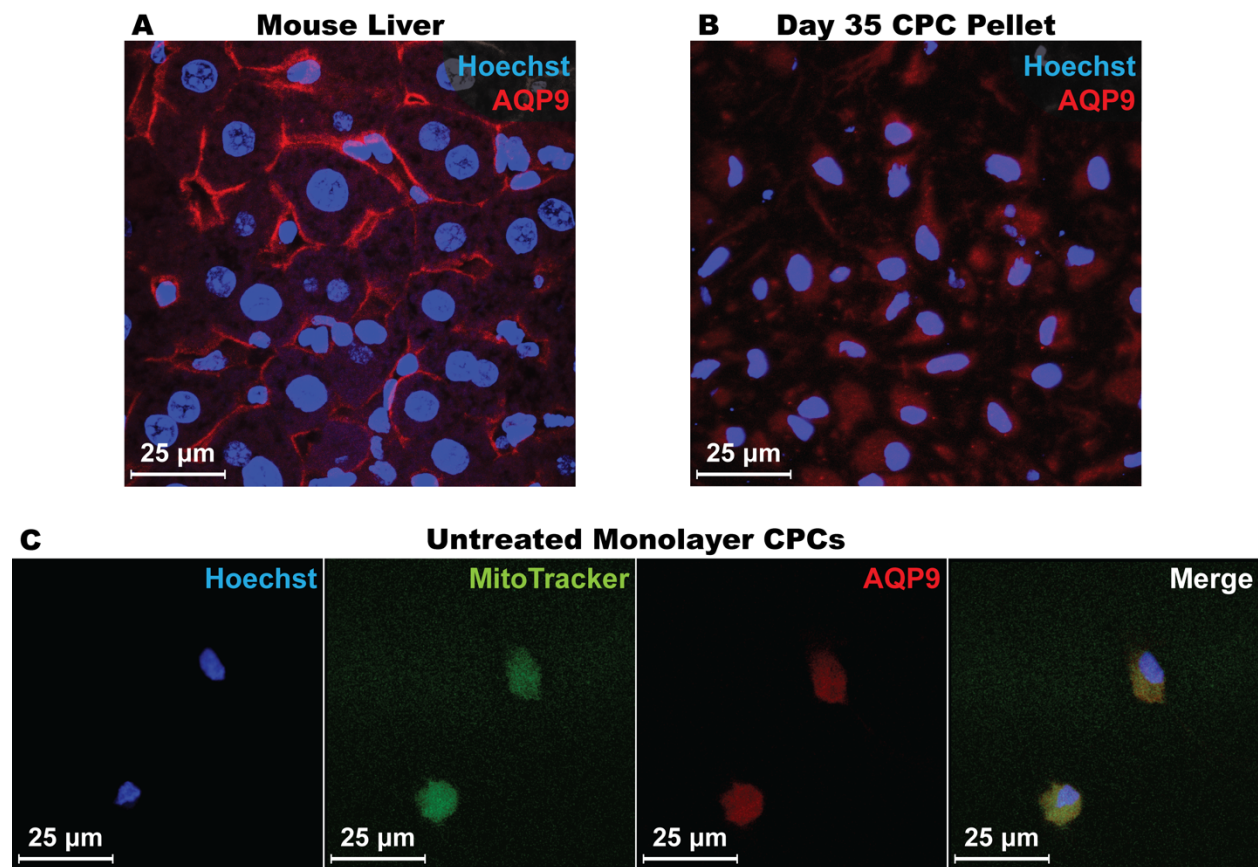
Fig. 3.7. Aquaporin-9 expression localizes to the mitochondrial membrane in cartilage progenitor cells. (A-B) Immunostaining of aquaporin-9 (AQP9) in A) mouse liver tissue from a wild-type C57Bl/6 mouse and B) cartilage progenitor cell pellets after 35 days of chondrogenic induction. C) Dual immunostaining of AQP9 and MitoTracker Green in monolayer cartilage progenitor cells.

3.5 Discussion

We report that the miR-181a/b-1 cluster promotes anabolic pathways in TGF-β-induced chondrogenic differentiation of CPCs in three-dimensional pellet cultures under physoxic conditions *in vitro*. Several of the top upregulated genes, including *SNORC, MATN4*, and *CKB*, have recently been identified as regulators of cartilage development and homeostasis. Heinonen *et al.* identified *SNORC* as a cartilage-specific transmembrane proteoglycan that is critical for regulation of chondrocyte proliferation and maturation during endochondral ossification[29,30]. Another upregulated gene, *MATN4*, is expressed in cartilage, including prechondroblasts and articular chondrocytes, during development[31]. Creatine kinase B (CKB) is critical for growth plate development, cartilage anabolism, and chondrocyte maturation/hypertrophy[32,33]. Upregulation of this set of genes suggests that miR-181a/b-1 promotes CPC proliferation and differentiation into prehypertrophic chondrocytes.

Bioinformatic analysis of Reactome signaling pathways further supported a pro-anabolic/anti-catabolic role for miR-181a/b-1 in chondrogenesis. Pro-anabolic pathways promoted by miR-181a/b-1 over-expression included extracellular matrix organization; collagen formation, biosynthesis and modifying enzymes, and chain trimerization; and assembly of collagen fibrils and other multimeric structures. Reactome pathways associated with NF-κB activation via TNFR2 (R-HSA-5668541), FCERI (R-HSA-2871837), and CLEC7A (also known as Dectin-1; R-HSA-5607761) were all significantly downregulated. The NF-κB signaling pathway is a known promotor of inflammation and cartilage catabolism[34,35] indicating a possible anti-inflammatory role for miR-181a/b-1. Reactome pathways for RUNX2/3 expression (R-HSA-8939902 and R-HSA-8941858) were also downregulated. Both RUNX2 and RUNX3 are key regulators of chondrocyte hypertrophy and osteoblast differentiation and are upregulated during catabolic chondrocyte processes[35,36] denoting an anti-catabolic, anti-hypertrophy role for miR-

181a/b-1 during chondrogenic induction. This bioinformatic analysis supports a pro-anabolic role for miR-181a/b-1, and further studies are needed to properly assess its role in potentially regulating hypertrophic differentiation during chondrogenesis.

Prior studies of miR-181a/b in cartilage development and homeostasis studies suggest that it may promote hypertrophy during differentiation, or catabolic processes in mature chondrocytes. Specifically, Nakamura *et al.* demonstrated that intra-articular injection of miR-181a mimics in a rat model of spinal facet joint OA exacerbated NF-κB mediated cartilage catabolism and degradation[8]. The same group showed that intra-articular injections of miR-181a antagomirs protected against cartilage degradation in a rat model of facet joint OA and a mouse model of trauma-induced knee OA[9]. Others have reported a correlation between expression of miR-181a and hypertrophic chondrocyte marker *COL10A1* during *in vitro* MSC chondrogenesis[37] and *in vivo* embryonic human growth plate development[4]. In our CPC differentiation assays, COLX immunostaining of pellet cultures was attempted, but it was not expressed at detectable levels in control or treated pellets at Day 35 of chondrogenic induction (data not shown). Expression of *COL10A1* was also not detected in the RNA sequencing data on samples harvested at Day 7 of chondrogenic induction. Taken together, we propose that, while miR-181a appears to be detrimental to cartilage homeostasis *in vivo*, it appears to play a role in promoting chondrocyte differentiation and anabolic, ECM-promoting activity during *in vitro* chondrogenesis.

To better understand the molecular mechanisms underpinning this pro-differentiation function, we explored downregulated genes that are potential targets of miR-181a/b-1. Only two reported, and confirmed, targets of miR-181a/b were significantly downregulated in our RNA-Seq data: chromobox 7 (*CBX7*)[21,22] and protein tyrosine phosphatase non-receptor type 22 (*PTPN22*)[23]. While *PTPN22* has not been studied in the skeletal system, downregulation of *CBX7* via miR-

181a/b over-expression has been reported to enhance murine embryonic stem cell differentiation[21]. This suggests that the pro-differentiation function of miR-181a/b-1 in CPC chondrogenesis may involve targeting of *CBX7*. One downregulated gene that was also a predicted, but unconfirmed, miR-181a/b target was aquaporin-9 (*AQP9*). Here, we used a luciferase assay to show that miR-181a/b did not directly target the 3' UTR of *AQP9* indicating that miR-181a/b-1 indirectly downregulates *AQP9* during TGF-β-induced chondrogenesis. However, the predicted binding site for miR-181a/b is only present in humans and is not evolutionarily conserved, suggesting that is may not a direct target for miR-181a/b. Further studies are needed to determine the mechanisms by which this indirect suppression occurs. Very little is known about AQP9, or indeed any of the other 12 identified aquaporins, in skeletal tissues. AQP9 is a membrane channel protein that can transport small molecules such as water, glycerol, urea, hydrogen peroxide[38,39]. While *AQP9* localizes to the cell membrane in many tissues[27], it has also been found on the mitochondrial membrane in rat brain cells[13,28]. Our studies showed that AQP9 localized inside chondrocytes and co-localized with MitoTracker in CPCs. Studies have shown that miR-181a/b-1 regulates mitochondrial metabolism[6] and this novel indirect downregulation of *AQP9* suggests a potential new mechanism for regulating mitochondrial metabolism. Studies of AQP9 in chondrocyte cultures have suggested that AQP9 promotes cartilage catabolism via NF-κB signaling in response to IL-1β stimulation *in vitro*[40]. Our finding that NF-κB activation-related Reactome pathways were knocked down when AQP9 was downregulated supports this mechanism. Others have studied endochondral ossification in AQP9^{-/-} mice (Jax Stock No. # 037111-JAX) and found that knockout mice have significantly thicker proliferating zones in their growth plates[41]. Interestingly, in osteoclast studies, treatment with phloretin, a non-specific AQP9 inhibitor, reduced osteoclast nuclei count and cell size

suggesting that AQP9 inhibition negatively regulated monocyte fusion and cytosol synthesis by blocking AQP9-mediated water transport[42]. However, experiments using *AQP9*^{-/-} mice demonstrated that AQP9 was not necessary for osteoclast differentiation or function *in vivo* or during *in vitro* osteoclastogenesis using *AQP9*^{-/-} bone marrow macrophages[43]. Additional studies are necessary to fully understand the role of AQP9 during chondrogenesis.

Given the intracellular localization of AQP9 in CPCs and chondrocytes, its potential role in regulating mitochondrial metabolism/function during chondrocyte differentiation warrants further study. While we have established that *AQP9* is downregulated during *in vitro* chondrogenic assays, we must define its functional role in chondrogenesis by using *AQP9*-specific knockdown approaches, such as siRNAs and/or small molecule inhibitors. We must also further investigate the role of AQP9 in cartilage development by over-expressing *AQP9* in CPCs and assessing chondrogenic readouts, and by using commercially available AQP9 knockout mice (Jax Stock No. # 037111-JAX). Only a few studies have been conducted on AQP9 in cartilage and chondrogenesis.

In conclusion, over-expression of miR-181a/b-1 promotes cartilage anabolism and chondrocyte differentiation during TGF-β-mediated *in vitro* CPC chondrogenesis in three-dimensional pellet cultures under hypoxic conditions. The information presented in this study suggests that miR-181a/b-1 plays a key role in regulating chondrogenic differentiation and has a pro-differentiation, pro-anabolic function. Further, it may influence chondrogenesis via a novel mechanism involving indirect downregulation of AQP9.

3.6 References

1   McAlinden, A. & Im, G. I. MicroRNAs in orthopaedic research: Disease associations, potential therapeutic applications, and perspectives. *J Orthop Res* **36**, 33-51 (2018). https://doi.org/10.1002/jor.23822

2   Allas, L., Boumédiene, K. & Baugé, C. Epigenetic dynamic during endochondral ossification and articular cartilage development. *Bone* **120**, 523-532 (2019). https://doi.org/10.1016/j.bone.2018.10.004

3   Hensley, A. P. & McAlinden, A. The role of microRNAs in bone development. *Bone* **143**, 115760 (2021). https://doi.org/10.1016/j.bone.2020.115760

4   McAlinden, A., Varghese, N., Wirthlin, L. & Chang, L. W. Differentially expressed microRNAs in chondrocytes from distinct regions of developing human cartilage. *PLoS One* **8**, e75012 (2013). https://doi.org/10.1371/journal.pone.0075012

5   Yang, Z. *et al.* Evolution of the mir-181 microRNA family. *Comput Biol Med* **52**, 82-87 (2014). https://doi.org/10.1016/j.compbiomed.2014.06.004

6   Bell-Hensley, A., Das, S. & McAlinden, A. The miR-181 family: Wide-ranging pathophysiological effects on cell fate and function. *J Cell Physiol* **238**, 698-713 (2023). https://doi.org/10.1002/jcp.30969

7   Zheng, H., Liu, J., Tycksen, E., Nunley, R. & McAlinden, A. MicroRNA-181a/b-1 over-expression enhances osteogenesis by modulating PTEN/PI3K/AKT signaling and mitochondrial metabolism. *Bone* **123**, 92-102 (2019). https://doi.org/10.1016/j.bone.2019.03.020

8   Nakamura, A. *et al.* Identification of microRNA-181a-5p and microRNA-4454 as mediators of facet cartilage degeneration. *JCI Insight* **1**, e86820 (2016). https://doi.org/10.1172/jci.insight.86820

9   Nakamura, A. *et al.* microRNA-181a-5p antisense oligonucleotides attenuate osteoarthritis in facet and knee joints. *Ann Rheum Dis* **78**, 111-121 (2019). https://doi.org/10.1136/annrheumdis-2018-213629

10   Richner, M., Victor, M. B., Liu, Y., Abernathy, D. & Yoo, A. S. MicroRNA-based conversion of human fibroblasts into striatal medium spiny neurons. *Nat Protoc* **10**, 1543-1555 (2015). https://doi.org/10.1038/nprot.2015.102

11   Bell-Hensley, A., Zheng, H. & McAlinden, A. Modulation of MicroRNA Expression During In Vitro Chondrogenesis. *Methods Mol Biol* **2598**, 197-215 (2023). https://doi.org/10.1007/978-1-0716-2839-3_15

12   McAlinden, A., Hudson, D. M., Fernandes, A. A., Ravindran, S. & Fernandes, R. J. Biochemical and immuno-histochemical localization of type IIA procollagen in annulus fibrosus of mature bovine intervertebral disc. *Matrix Biol Plus* **12**, 100077 (2021). https://doi.org/10.1016/j.mbplus.2021.100077

13   Amiry-Moghaddam, M. *et al.* Brain mitochondria contain aquaporin water channels: evidence for the expression of a short AQP9 isoform in the inner mitochondrial membrane. *FASEB J* **19**, 1459-1467 (2005). https://doi.org/10.1096/fj.04-3515com

14   Dobin, A. *et al.* STAR: ultrafast universal RNA-seq aligner. *Bioinformatics* **29**, 15-21 (2013). https://doi.org/10.1093/bioinformatics/bts635

15   Liao, Y., Smyth, G. K. & Shi, W. featureCounts: an efficient general purpose program for assigning sequence reads to genomic features. *Bioinformatics* **30**, 923-930 (2014). https://doi.org/10.1093/bioinformatics/btt656

16   Ritchie, M. E. *et al.* limma powers differential expression analyses for RNA-sequencing and microarray studies. *Nucleic Acids Res* **43**, e47 (2015). https://doi.org/10.1093/nar/gkv007

17   Liu, R. *et al.* Why weight? Modelling sample and observational level variability improves power in RNA-seq analyses. *Nucleic Acids Res* **43**, e97 (2015). https://doi.org/10.1093/nar/gkv412

18   Enright, A. J. *et al.* MicroRNA targets in Drosophila. *Genome Biol* **5**, R1 (2003). https://doi.org/10.1186/gb-2003-5-1-r1

19   John, B. *et al.* Human MicroRNA targets. *PLoS Biol* **2**, e363 (2004). https://doi.org/10.1371/journal.pbio.0020363

20   Sandell, L. J., Nalin, A. M. & Reife, R. A. Alternative splice form of type II procollagen mRNA (IIA) is predominant in skeletal precursors and non-cartilaginous tissues during early mouse development. *Dev Dyn* **199**, 129-140 (1994). https://doi.org/10.1002/aja.1001990206

21   O'Loghlen, A. *et al.* MicroRNA regulation of Cbx7 mediates a switch of Polycomb orthologs during ESC differentiation. *Cell Stem Cell* **10**, 33-46 (2012). https://doi.org/10.1016/j.stem.2011.12.004

22   Mansueto, G. *et al.* Identification of a New Pathway for Tumor Progression: MicroRNA-181b Up-Regulation and CBX7 Down-Regulation by HMGA1 Protein. *Genes Cancer* **1**, 210-224 (2010). https://doi.org/10.1177/1947601910366860

23   Li, Q. J. *et al.* miR-181a is an intrinsic modulator of T cell sensitivity and selection. *Cell* **129**, 147-161 (2007). https://doi.org/10.1016/j.cell.2007.03.008

24   Zhang, J. Q. *et al.* miR-181a promotes porcine granulosa cell apoptosis by targeting TGFBR1 via the activin signaling pathway. *Mol Cell Endocrinol* **499**, 110603 (2020). https://doi.org/10.1016/j.mce.2019.110603

25   Marín, R. M. & Vanícek, J. Efficient use of accessibility in microRNA target prediction. *Nucleic Acids Res* **39**, 19-29 (2011). https://doi.org/10.1093/nar/gkq768

26   Huynh, N. P. T., Zhang, B. & Guilak, F. High-depth transcriptomic profiling reveals the temporal gene signature of human mesenchymal stem cells during chondrogenesis. *FASEB J* **33**, 358-372 (2019). https://doi.org/10.1096/fj.201800534R

27   Elkjaer, M. *et al.* Immunolocalization of AQP9 in liver, epididymis, testis, spleen, and brain. *Biochem Biophys Res Commun* **276**, 1118-1128 (2000). https://doi.org/10.1006/bbrc.2000.3505

28   Tescarollo, F., Covolan, L. & Pellerin, L. Glutamate reduces glucose utilization while concomitantly enhancing AQP9 and MCT2 expression in cultured rat hippocampal neurons. *Front Neurosci* **8**, 246 (2014). https://doi.org/10.3389/fnins.2014.00246

29   Heinonen, J. *et al.* Snorc is a novel cartilage specific small membrane proteoglycan expressed in differentiating and articular chondrocytes. *Osteoarthritis Cartilage* **19**, 1026-1035 (2011). https://doi.org/10.1016/j.joca.2011.04.016

30   Heinonen, J. *et al.* Defects in chondrocyte maturation and secondary ossification in mouse knee joint epiphyses due to Snorc deficiency. *Osteoarthritis Cartilage* **25**, 1132-1142 (2017). https://doi.org/10.1016/j.joca.2017.03.010

31   Groma, G. *et al.* Matrilin-4 is processed by ADAMTS-5 in late Golgi vesicles present in growth plate chondrocytes of defined differentiation state. *Matrix Biol* **30**, 275-280 (2011). https://doi.org/10.1016/j.matbio.2011.04.002

32   Shapiro, I. M., Debolt, K., Funanage, V. L., Smith, S. M. & Tuan, R. S. Developmental regulation of creatine kinase activity in cells of the epiphyseal growth cartilage. *J Bone Miner Res* **7**, 493-500 (1992). https://doi.org/10.1002/jbmr.5650070505

33   Funanage, V. L., Carango, P., Shapiro, I. M., Tokuoka, T. & Tuan, R. S. Creatine kinase activity is required for mineral deposition and matrix synthesis in endochondral growth cartilage. *Bone Miner* **17**, 228-236 (1992). https://doi.org/10.1016/0169-6009(92)90742-v

34   Rigoglou, S. & Papavassiliou, A. G. The NF-κB signalling pathway in osteoarthritis. *Int J Biochem Cell Biol* **45**, 2580-2584 (2013). https://doi.org/10.1016/j.biocel.2013.08.018

35   Chen, D., Kim, D. J., Shen, J., Zou, Z. & O'Keefe, R. J. Runx2 plays a central role in Osteoarthritis development. *J Orthop Translat* **23**, 132-139 (2020). https://doi.org/10.1016/j.jot.2019.11.008

36   Yoshida, C. A. *et al.* Runx2 and Runx3 are essential for chondrocyte maturation, and Runx2 regulates limb growth through induction of Indian hedgehog. *Genes Dev* **18**, 952-963 (2004). https://doi.org/10.1101/gad.1174704

37   Gabler, J. *et al.* Stage-Specific miRs in Chondrocyte Maturation: Differentiation-Dependent and Hypertrophy-Related miR Clusters and the miR-181 Family. *Tissue Eng Part A* **21**, 2840-2851 (2015). https://doi.org/10.1089/ten.TEA.2015.0352

38   Watanabe, S., Moniaga, C. S., Nielsen, S. & Hara-Chikuma, M. Aquaporin-9 facilitates membrane transport of hydrogen peroxide in mammalian cells. *Biochem Biophys Res Commun* **471**, 191-197 (2016). https://doi.org/10.1016/j.bbrc.2016.01.153

39   Tsukaguchi, H. *et al.* Molecular characterization of a broad selectivity neutral solute channel. *J Biol Chem* **273**, 24737-24743 (1998). https://doi.org/10.1074/jbc.273.38.24737

40   Takeuchi, K. *et al.* Downregulation of aquaporin 9 decreases catabolic factor expression through nuclear factor-κB signaling in chondrocytes. *Int J Mol Med* **42**, 1548-1558 (2018). https://doi.org/10.3892/ijmm.2018.3729

41   Tang, P. *Characterizing AQP9: a regulator of epiphyseal plate chondrocyte proliferation, hypertrophy, and long bone growth* M.Sc. thesis, University of Toronto, (2018).

42   Aharon, R. & Bar-Shavit, Z. Involvement of aquaporin 9 in osteoclast differentiation. *J Biol Chem* **281**, 19305-19309 (2006). https://doi.org/10.1074/jbc.M601728200

43   Liu, Y. *et al.* Osteoclast differentiation and function in aquaglyceroporin AQP9-null mice. *Biol Cell* **101**, 133-140 (2009). https://doi.org/10.1042/BC20080083

Chapter 4: MicroRNA-138 Does Not Regulate Cartilage Progenitor Cell Chondrogenesis

4.1 Abstract

Generation of stable, native-like articular cartilage *in vitro* is an ongoing challenge for the field

of cartilage tissue engineering. Developing articular-like cartilage tissue constructs is critical for

creating biomimetic treatments for articular cartilage defects and osteoarthritis. Epigenetic

regulators like miRNAs have been reported to play an important role in natural cartilage

development. Here, we over-express miR-138 in cartilage progenitor cells during an *in vitro*

chondrogenesis assay to better mimic differentiation cues that are present during developmental

cartilage formation. We report that miR-138 over-expression does not promote or inhibit

cartilaginous differentiation of cartilage progenitor cells. Bulk RNA-sequencing was performed

to assess the molecular impact of miR-138 over-expression and several signaling pathways that

are involved in chondrocyte differentiation and homeostasis were down-regulated. This study

adds to the ambiguous literature regarding the role of miR-138 in chondrogenesis, but identifies

biological pathways that may be important for understanding why this miRNA is differentially

expressed in distinct zones of developing cartilage.

4.2 Introduction

Guiding differentiation of progenitor cells along native-like differentiation lineages requires

native-like biochemical stimulation. In chondrogenic assays, this typically involves use of potent

pro-chondrogenic molecules such as TGF-β [1,2] or BMP-2 [3-6]. However, the intricacies of *in vivo*

cartilage differentiation demand a more nuanced approach.

While numerous protein-coding genes and proteins have been identified as key regulators of chondrogenic differentiation, a microarray from McAlinden *et al* was the first to investigate expression of miRNAs in distinct layers of developing cartilage[7]. This microarray identified a battery of miRNAs with differential expression in chondro-progenitors, proliferating zone chondrocytes, and hypertrophic zone chondrocytes. Among the differentially expressed miRNAs was miR-138, whose expression was significantly lower in chondro-progenitors than in proliferating or hypertrophic zone chondrocytes.

Initial characterization of miR-138 in mice found that it was expressed primarily in the brain, but it was also detected at lower levels in cartilage, long bone, and muscle among others including the eye, pancreas, small intestine, and testis[8-10]. Given its endogenous expression pattern, many studies of miR-138 have focused on its role in neuronal differentiation and regeneration as well as neurological diseases which was discussed in a recent review article from our group[11]. While miR-138 is decreased in some neurological diseases, such as Alzheimer's disease[12,13], there are reports that it is upregulated during brain cancers[14]. Cancer screens in other parts of the body have also detected miR-138 as differentially expressed in various cancers and, in almost all cases, miR-138 expression correlates with improved survival[15,16]. Several common pathways are affected by miR-138 in its tumor suppression function and regulation of neurological developmental pathways including cell proliferation via targeting of RhoC[17,18] and cytoskeleton maintenance via targeting of vimentin[19].

After identifying miR-138 as a differentially expressed miRNA in the developing limb bud, the McAlinden lab and others have assessed the role of miR-138 in osteogenic differentiation and found that it was a potent inhibitor of osteogenesis[11,18]. In the context of endochondral ossification, this suggests that miR-138 may delay chondroprogenitor cell maturation into

hypertrophic-like chondrocytes, possibly by preventing the cytoskeleton remodeling necessary to develop into hypertrophic-like chondrocytes [20,21]. The increased expression of miR-138 in proliferating and hypertrophic chondrocytes reported in the microarray by McAlinden *et al* suggests that it may be critical in regulating the duration of each phase of chondroprogenitor maturation[7].

Here, we report that over-expression of miR-138 in CPCs does not promote or inhibit chondrogenic differentiation. Bioinformatic analysis of bulk RNA-Seq data indicates conflicting roles for miR-138 during *in vitro* CPC chondrogenesis, leaving uncertainties about its influence on cartilage development.

4.3 Methods

4.3.1 Cartilage Progenitor Cell Isolation and Expansion

Cartilage progenitor cells (CPCs) were isolated and expanded as previously described in *Section 2.3.1* (Tissue Collection) and *Section 2.3.2* (Cartilage Progenitor Cell Isolation and Expansion). After frozen storage, CPCs were expanded in growth medium for at least 6 passages, until use in differentiation assays.

4.3.2 Lentivirus Generation, Testing, and Transduction

Human genomic pre-miR-138-1 (NCBI Ref Seq: NR_029700.1) was amplified by PCR (Table 4.1). The resulting miR-138-1 amplicon was inserted into the pLemiR backbone (Addgene), prepared, titered, and stored as previously described in *Section 3.3.2* (Lentivirus Generation). The resulting virus was tested in Passage 5 CPCs and transduced in Passage 6 CPCs as previously described in *Section 3.3.3* (Lentivirus Testing) and *Section 3.3.4* (Lentivirus Transduction), respectively.

4.3.3 Chondrogenic Differentiation Assay

Transduced and non-transduced CPCs were trypsinized, resuspended in chondrogenic induction medium, and cultured as micromass pellets down a chondrogenic lineage for 5 weeks as previously described in *Section 3.3.5* (Chondrogenic Differentiation Assay).

4.3.4 RNA Isolation

On day 7 and day 35 of the chondrogenic differentiation assay, pellets were collected for RNA isolation as previously described in *Section 3.3.6* (RNA Isolation).

4.3.5 MicroRNA Quantitative Polymerase Chain Reaction

Using the isolated total RNA, miR-138-5p were reverse-transcribed and quantified using the appropriate TaqMan primer/probe sets (Life Technologies Inc; Table 4.1) along with the TaqMan microRNA reverse transcription kit (Life Technologies Inc.) and TaqMan master mix with no UNG (Life Technologies Inc.). Fold changes were calculated using the $2^{-\Delta Ct}$ method using RNU44 as a reference small RNA[22].

Table 4.1. Primer sequences and Life Technologies miRNA assay IDs used for vector cloning and quantitative PCR.

Amplicon	Forward Primer	Reverse Primer
miR-138 Genomic	GCACAGATAACTCGAGCGGATG GGGAAGGCAGTGAAATG	GGGAGAGGGGCGGAATTTGCGG GGGATAAACAGCAGCC
miR-138-5p	TaqMan miRNA assay ID 002284 (Life Technologies Inc.)	
RNU44	TaqMan miRNA assay ID 001094 (Life Technologies Inc.)	

4.3.6 Histology and Immunofluorescence

On day 35 of the chondrogenic differentiation assay, 3-4 pellets per group were collected for histological evaluation and imaging as previously described in *Section 3.3.8* (Histology and Immunofluorescence).

4.3.7 Quantitative assessment of histology and immunofluorescence images

Whole slide images of the safranin-O and immunostained pellet tissue sections were exported

and analyzed as previously described in *Section 3.3.9* (Quantitative assessment of histology and

immunofluorescence images).

4.3.8 Bulk RNA sequencing and pathway analysis

Day 7 RNA from four independent cell lines (transduced with LV-NS or LV-138) with adequate

day 7 miR-138 over-expression and consistent day 35 histology and immunofluorescence

staining were submitted for bulk RNA-Sequencing as previously described in *Section 3.3.10*

(Bulk RNA sequencing and pathway analysis). Raw and processed data from this study has been

uploaded to the GEO depository and assigned the accession code: GSE262978.

4.3.9 Statistical Analysis

All experiments were carried out in triplicate with CPCs derived from 3-4 independent biological

replicates. Data are presented as mean ± SD and statistical comparisons were made using paired

t-tests with pairing between CPCs expanded from the same donor, except for RNA expression

data which was compared using ratio paired t-tests to better assess proportional differences in

fold change. Probability values were considered statistically significant at $p \leq 0.05$.

4.4 Results

4.4.1 Chondrogenic extracellular matrix composition unaffected by miR-138 over-expression

To evaluate the impact of lentivirus mediated overexpression of miR-138 (LV-138) on

chondrogenic differentiation, extracellular matrix composition was histologically evaluated in

CPCs after 35 days in chondrogenic induction media. The CPCs, cultured as micromass pellets

in a physoxic (5% O_2) environment, had robust over-expression of the functional miR-138-5p

strand at Day 7 and Day 35 of the differentiation assay when compared to a control group with

lentiviral over-expression of a non-silencing sequence (LV-NS) (Fig. 4.1A). Of note, the

endogenous expression of miR-138 in the LV-NS CPCs decreased significantly over the course

of the differentiation assay (Fig. 4.1B). Despite the significant increase in miR-138-5p, there was

no difference in the area fraction that stained positively for proteoglycans or collagens via

safranin-O histology or immunostaining, respectively (Fig. 4.1C-K). There are upward trends in

the area fractions for safranin-O, type II collagen, and "embryonic" type IIA procollagen

staining, however this positive trend has a large variance in effect size depending on the CPC

donor. Given the current sample size, we can say that miR-138 over-expression has no impact on

chondrogenic differentiation outcomes, but miR-138 is downregulated during *in vitro* CPC
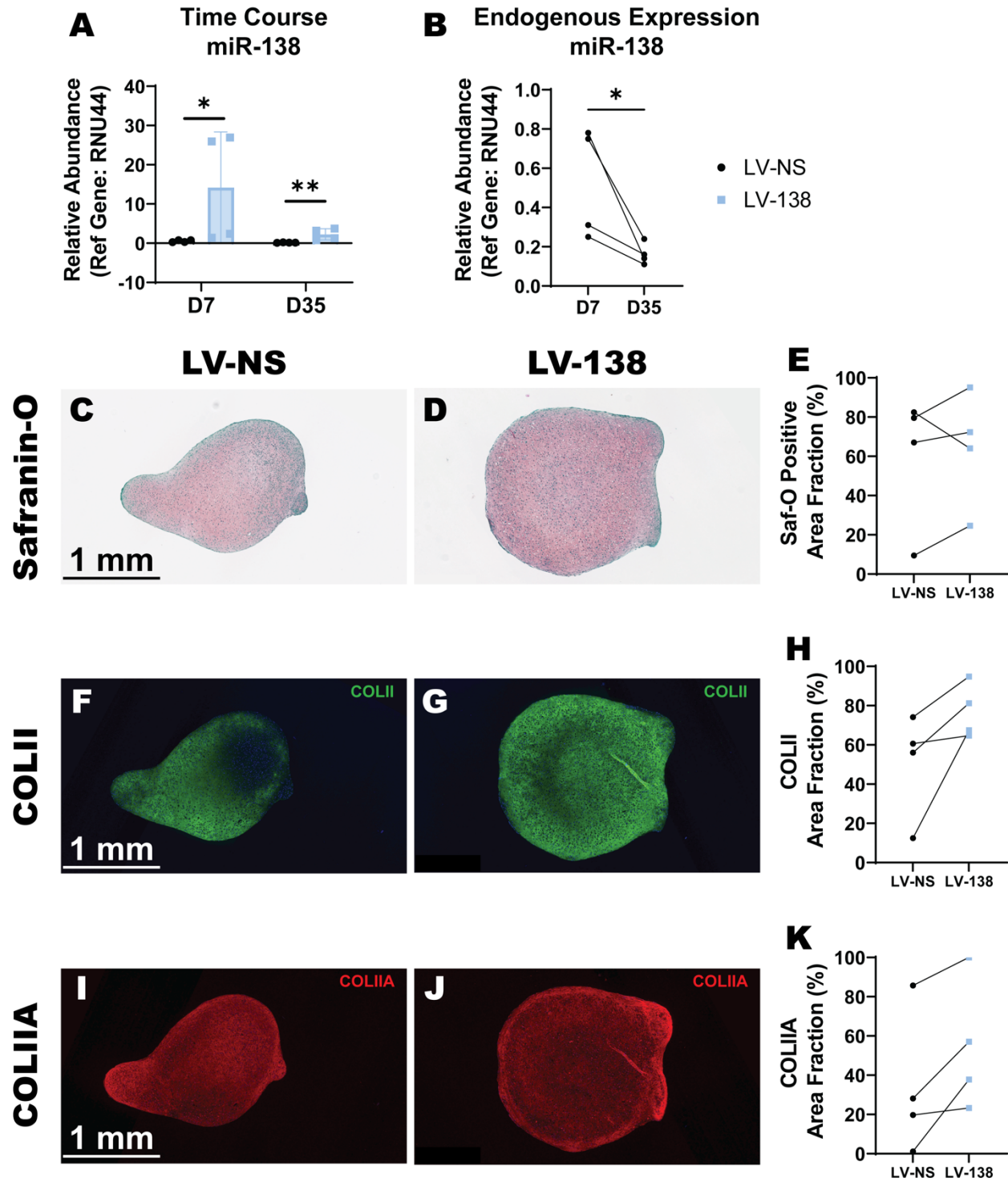
chondrogenesis.

Fig. 4.1. Chondrogenic differentiation unaffected by miR-138 over-expression. (A-B) Relative abundance of miR-138 in A) LV-138 and LV-NS groups and B) LV-NS groups after 7 and 35 days. (C-K) Representative images and quantitative analysis of Safranin-O histology (Saf-O; C-E) and immunostaining for type II collagen (COLII; F-H) and type IIA pro-collagen (COLIIA; I-K). Immunostaining and quantitative analysis performed on pellet cultures after 35 days of chondrogenic induction. Positive staining was quantified as a percentage of the total cross-sectional area for quantitative analyses (E, H, K). * $p < 0.05$, ** $p < 0.01$. $n = 4$ CPC lines from independent donors. For miRNA expression analysis, RNA was pooled from 7-10 pellets (Day 7) or 2-4 pellets (Day 35). For histology and immunostaining, each dot is the average for 3-4 pellets for CPCs from a single donor. Abbreviations: LV-NS lentivirus

encoding non-silencing miRNA sequence, LV-138 lentivirus encoding pre-miR-138, Saf-O Safranin-O, COLII type II collagen, COLIIA type IIA pro-collagen.

4.4.2 Over-expression of miR-138 does not cause significant differential gene expression

Since miR-138 is downregulated during chondrogenesis, we performed RNA-Seq on RNA isolated after 7 days of the chondrogenic differentiation to see if miR-138 over-expression impacted the inner workings of the CPCs. RNA transcripts from over 12,000 protein-coding genes were detected, but only one of them, *CCDC69*, had a p-value of less than 0.05 after correcting for false-discovery rate using the Benjamini-Hochberg procedure (Fig 4.2A). None of the detected genes, including *CCDC69*, had a Log_2 fold-change magnitude of greater than 2. MicroRNAs can affect their mRNA targets by causing degradation, but more frequently they cause dysregulation by repressing translation. While this translational repression cannot be detected by RNA-Seq, the pathways downstream of the target mRNAs can be identified. Bioinformatic analyses of gene ontology (GO) terms were completed using the generally applicable gene expression gene-set analysis (GAGE) technique. However, even using these broader approaches, only one GO term, *hydrolase activity*, was significantly perturbed (Fig. 4.2B). These findings suggest that miR-138 over-expression does not upregulate any key cartilage anabolic or catabolic functions at Day 7 of CPC chondrogenesis.
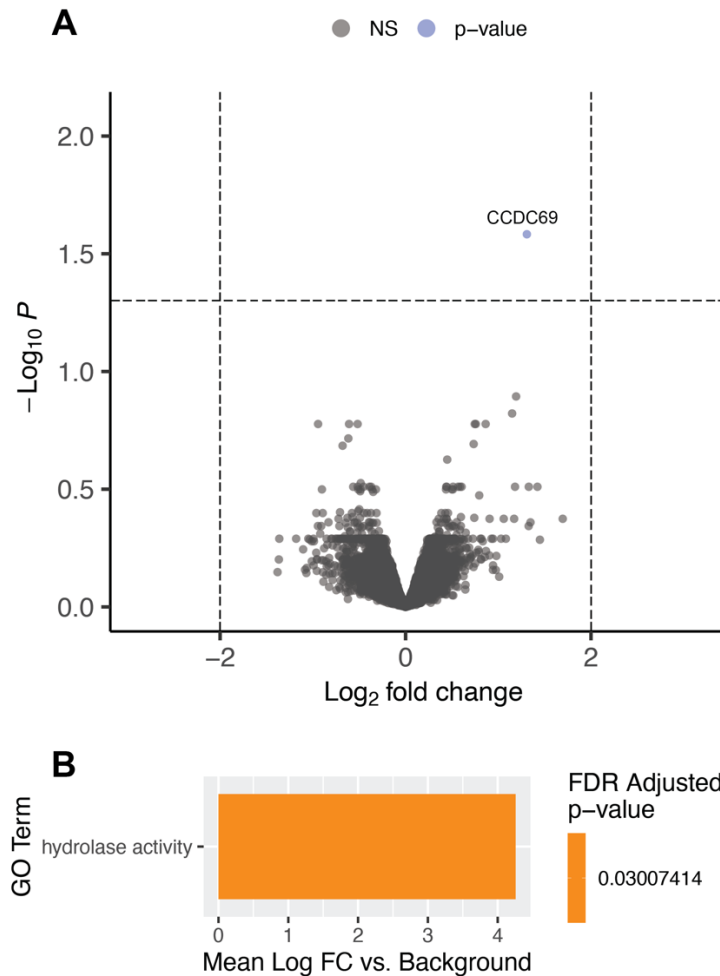
Fig. 4.2. Differentially expressed genes following miR-138 over-expression. A) Volcano plot showing differentially expressed genes in CPCs after 7 days of chondrogenic induction following miR-138 over-expression. P-values are adjusted for Benjamini-Hochberg false discovery rate (FDR). B) Significantly perturbed GO molecular functions at Day 7 of CPC chondrogenesis following miR-138 over-expression. $n = 4$ CPC lines from independent donors; RNA was pooled from 7-10 pellets (Day 7).

4.4.3 miR-138 over-expression downregulates conflicting pathways during CPC chondrogenesis

While only a few genes and GO terms were dysregulated following miR-138 over-expression, there were 23 significantly perturbed Reactome pathways (Fig. 4.3). Interestingly, 21 of the highlighted Reactome pathways were downregulated despite there being no significantly downregulated genes or GO terms. Several of the inhibited Reactome pathways could be associated with cartilage differentiation including pro-anabolic pathways like *collagen chain trimerization*, pro-catabolic pathways like *formation of the beta-catenin:TCF transactivating complex*, and cellular senescence pathways like *oxidative stress induced senescence*. The

77

abundance of conflicting downregulated Reactome pathways implicates a complex role for miR-138 in chondrogenesis.

Fig. 4.3. Significantly perturbed Reactome biological pathways at Day 7 of CPC chondrogenesis following miR-138 over-expression.

4.5 Discussion

We report that lentiviral-mediated over-expression of miR-138 does not have an impact on CPC chondrogenesis. While there are few gene targets and GO pathways implicated by our analysis,

there are several downregulated Reactome pathways that align with previous reports on miR-138 in the context of bone development and homeostasis[11] as well as tumor suppression[16]. These overlaps suggest that miR-138 may be acting to transcriptionally repress some of its known targets despite its lack of influence on chondrogenic outcomes via proteoglycan and COLII accumulation.

One downregulated pathway that was previously connected to miR-138 over-expression is *RHO GTPases activate PKNs*. This pathway includes *RHOC*, a known target of miR-138[17,18]. While *RHOC* is not differentially expressed, transcriptional repression by miR-138 could have a downstream effect on cell migration, focal adhesion, and proliferation[11,16-18,23]. Reactome pathway analysis also indicated that another cell proliferation-related pathway, *condensation of prophase chromosomes*, was downregulated, further supporting an anti-proliferation role for miR-138 in CPC chondrogenesis.

Interestingly, among the conflicting studies on the role of miR-138 in chondrogenesis, there are a few studies that suggest that miR-138 is anti-proliferation and anti-migration. Wang *et al* and Chunlei *et al* showed that treating chondrogenic cell lines with an inhibitor for miR-138-5p enhanced cell proliferation[24,25]. Meanwhile, Shi *et al* reported that treating chondrogenic cells with miR-138 mimics hindered proliferation and cell migration[26]. These studies showed that miR-138 can target *SOX9*[24], *HIF1A*[25], and *MCM3AP-AS1*[26]. All three of these genes were minimally downregulated in our CPC chondrogenesis assay, ranging from a fold change of -0.07 to -0.15 with adjusted p-values greater than 0.8.

The range of proposed roles for miR-138 in chondrogenesis varies widely, as discussed in our group's recent review article, so an unclear role for miR-138 is perhaps unsurprising[11]. Our pathway analysis indicated downregulation of one pro-anabolic pathway, *collagen chain*

trimerization, suggesting an anti-anabolic for miR-138. However, it is clear that additional studies with temporally regulated over-expression are necessary to better understand its role in chondrogenesis. The original microarray by McAlinden *et al*[7] indicated an upregulation of miR-138 in hypertrophic chondrocytes, so over-expression of miR-138 during the later stages of chondrogenesis should be investigated. In future *in vitro* experiments, RNA-Seq data from timepoints aligned with chondrocyte hypertrophy would be informative – for the CPCs used in this study, that would extend beyond 35 days in chondrogenic induction media. To expedite hypertrophic differentiation, CPC chondrogenesis assays could be performed in an environment with atmospheric oxygen levels rather than physoxia[27,28]. Alternatively, miR-138 could be over-expressed in MSCs which are known to undergo hypertrophy in chondrogenic assays[27]. For an *in vivo* approach, generation of a genetic mouse model with a miR-138 knock-out or knock-in would enable critical studies on the function of miR-138 during the native endochondral ossification process.

4.6 References

1   Yoo, J. U. *et al.* The chondrogenic potential of human bone-marrow-derived mesenchymal progenitor cells. *J Bone Joint Surg Am* **80**, 1745-1757 (1998). https://doi.org/10.2106/00004623-199812000-00004

2   Johnstone, B., Hering, T. M., Caplan, A. I., Goldberg, V. M. & Yoo, J. U. In vitro chondrogenesis of bone marrow-derived mesenchymal progenitor cells. *Exp Cell Res* **238**, 265-272 (1998). https://doi.org/10.1006/excr.1997.3858

3   Schmitt, B. *et al.* BMP2 initiates chondrogenic lineage development of adult human mesenchymal stem cells in high-density culture. *Differentiation* **71**, 567-577 (2003). https://doi.org/10.1111/j.1432-0436.2003.07109003.x

4   Kramer, J. *et al.* Embryonic stem cell-derived chondrogenic differentiation in vitro: activation by BMP-2 and BMP-4. *Mech Dev* **92**, 193-205 (2000). https://doi.org/10.1016/s0925-4773(99)00339-1

5   Denker, A. E., Haas, A. R., Nicoll, S. B. & Tuan, R. S. Chondrogenic differentiation of murine C3H10T1/2 multipotential mesenchymal cells: I. Stimulation by bone morphogenetic protein-2 in high-density micromass cultures. *Differentiation* **64**, 67-76 (1999). https://doi.org/10.1046/j.1432-0436.1999.6420067.x

6   Haas, A. R. & Tuan, R. S. Chondrogenic differentiation of murine C3H10T1/2 multipotential mesenchymal cells: II. Stimulation by bone morphogenetic protein-2 requires modulation of N-cadherin expression and function. *Differentiation* **64**, 77-89 (1999). https://doi.org/10.1046/j.1432-0436.1999.6420077.x

7   McAlinden, A., Varghese, N., Wirthlin, L. & Chang, L. W. Differentially expressed microRNAs in chondrocytes from distinct regions of developing human cartilage. *PLoS One* **8**, e75012 (2013). https://doi.org/10.1371/journal.pone.0075012

8   Obernosterer, G., Leuschner, P. J., Alenius, M. & Martinez, J. Post-transcriptional regulation of microRNA expression. *RNA* **12**, 1161-1167 (2006). https://doi.org/10.1261/rna.2322506

9   Seidl, C. I., Martinez-Sanchez, A. & Murphy, C. L. Derepression of MicroRNA-138 Contributes to Loss of the Human Articular Chondrocyte Phenotype. *Arthritis Rheumatol* **68**, 398-409 (2016). https://doi.org/10.1002/art.39428

10   Eskildsen, T. *et al.* MicroRNA-138 regulates osteogenic differentiation of human stromal (mesenchymal) stem cells in vivo. *Proc Natl Acad Sci U S A* **108**, 6139-6144 (2011). https://doi.org/10.1073/pnas.1016758108

11   Brito, V. G. B., Bell-Hensley, A. & McAlinden, A. MicroRNA-138: an emerging regulator of skeletal development, homeostasis, and disease. *Am J Physiol Cell Physiol* **325**, C1387-C1400 (2023). https://doi.org/10.1152/ajpcell.00382.2023

12   Lau, P. *et al.* Alteration of the microRNA network during the progression of Alzheimer's disease. *EMBO Mol Med* **5**, 1613-1634 (2013). https://doi.org/10.1002/emmm.201201974

13   Kan, A. A. *et al.* Genome-wide microRNA profiling of human temporal lobe epilepsy identifies modulators of the immune response. *Cell Mol Life Sci* **69**, 3127-3145 (2012). https://doi.org/10.1007/s00018-012-0992-7

14   Wei, J. *et al.* MiR-138 exerts anti-glioma efficacy by targeting immune checkpoints. *Neuro Oncol* **18**, 639-648 (2016). https://doi.org/10.1093/neuonc/nov292

15   Yeh, M., Oh, C. S., Yoo, J. Y., Kaur, B. & Lee, T. J. Pivotal role of microRNA-138 in human cancers. *Am J Cancer Res* **9**, 1118-1126 (2019).

16   Sha, H. H. *et al.* MiR-138: A promising therapeutic target for cancer. *Tumour Biol* **39**, 1010428317697575 (2017). https://doi.org/10.1177/1010428317697575

17   Islam, M., Datta, J., Lang, J. C. & Teknos, T. N. Down regulation of RhoC by microRNA-138 results in de-activation of FAK, Src and Erk1/2 signaling pathway in head and neck squamous cell carcinoma. *Oral Oncol* **50**, 448-456 (2014).

18   Zheng, H. *et al.* MicroRNA-138 Inhibits Osteogenic Differentiation and Mineralization of Human Dedifferentiated Chondrocytes by Regulating RhoC and the Actin Cytoskeleton. *JBMR Plus* **3**, e10071 (2019). https://doi.org/10.1002/jbm4.10071

19   Zhang, J. *et al.* in *Biomed Pharmacother* Vol. 77   135-141 (© 2015. Published by Elsevier Masson SAS., 2016).

20   Reichenberger, E., Aigner, T., von der Mark, K., Stöss, H. & Bertling, W. In situ hybridization studies on the expression of type X collagen in fetal human cartilage. *Dev Biol* **148**, 562-572 (1991). https://doi.org/10.1016/0012-1606(91)90274-7

21   Woods, A., Wang, G. & Beier, F. Regulation of chondrocyte differentiation by the actin cytoskeleton and adhesive interactions. *J Cell Physiol* **213**, 1-8 (2007). https://doi.org/10.1002/jcp.21110

22   Bell-Hensley, A., Zheng, H. & McAlinden, A. Modulation of MicroRNA Expression During In Vitro Chondrogenesis. *Methods Mol Biol* **2598**, 197-215 (2023). https://doi.org/10.1007/978-1-0716-2839-3_15

23   Jiang, L. *et al.* Downregulation of the Rho GTPase signaling pathway is involved in the microRNA-138-mediated inhibition of cell migration and invasion in tongue squamous cell carcinoma. *Int J Cancer* **127**, 505-512 (2010). https://doi.org/10.1002/ijc.25320

24   Chunlei, H. *et al.* Down-regulation of MiR-138-5p Protects Chondrocytes ATDC5 and CHON-001 from IL-1 β-induced Inflammation. *Curr Pharm Des* **25**, 4613-4621 (2020). https://doi.org/10.2174/1381612825666190905163046

25   Wang, X. *et al.* LncRNA-RP11-296A18.3/miR-138/HIF1A Pathway Regulates the Proliferation ECM Synthesis of Human Nucleus Pulposus Cells (HNPCs). *J Cell Biochem* **118**, 4862-4871 (2017). https://doi.org/10.1002/jcb.26166

26   Shi, J. *et al.* Long non-coding RNA MCM3AP-AS1 protects chondrocytes ATDC5 and CHON-001 from IL-1β-induced inflammation via regulating miR-138-5p/SIRT1. *Bioengineered* **12**, 1445-1456 (2021). https://doi.org/10.1080/21655979.2021.1905247

27   Anderson, D. E., Markway, B. D., Bond, D., McCarthy, H. E. & Johnstone, B. Responses to altered oxygen tension are distinct between human stem cells of high and low chondrogenic capacity. *Stem Cell Res Ther* **7**, 154 (2016). https://doi.org/10.1186/s13287-016-0419-8

28   Anderson, D. E., Markway, B. D., Weekes, K. J., McCarthy, H. E. & Johnstone, B. Physioxia Promotes the Articular Chondrocyte-Like Phenotype in Human Chondroprogenitor-Derived Self-Organized Tissue. *Tissue Eng Part A* **24**, 264-274 (2018). https://doi.org/10.1089/ten.TEA.2016.0510

Chapter 5: Future Directions: MicroRNA-Mediated Osteochondral Engineering

5.1 Conclusions and Future Directions

CPCs are widely recognized as a promising candidate for osteochondral engineering due to their inherent chondrogenicity. Several groups have developed three-dimensional scaffolds containing chondro-inductive biochemical cues to successfully stimulate CPC chondrogenesis[1-4]. However, to produce native-like cartilage tissue, it is necessary to improve mimicry of the *in vivo* cartilage development environment. Studies on the evolutionary conservation of miRNAs have shown that the number of miRNAs correlates with an organism's structural complexity[5,6]. This suggests that miRNAs evolved out of a need for genomic regulatory elements for rapid, error-free development. To scale up development of biomimetic tissue constructs, utilizing pro-differentiation miRNAs like miR-181a/b-1 will be critical for streamlining native-like tissue development.

Our finding that AQP9 is expressed highly in chondroprogenitors but tapers off during chondrogenic differentiation represents a novel biological pathway that may be critical during cartilage development. Given the wide array of molecules that can be transported by AQP9, it will be critical to confirm the location of AQP9 in chondroprogenitors and chondrocytes as well as the molecule(s) that it transports. In osteoclastogenesis, it has been proposed that AQP9 plays a critical role in osteoclast cell size by regulating the uptake of water into the cytosol during monocyte fusion[7]. It will be interesting to see if it plays a similar role in mitochondrial fusion in chondrocytes, or if it helps regulate cell size during chondrocyte hypertrophy. Further investigation of the inverse relationship between anabolic cartilage pathways and AQP9

expression must be completed to better define the role of this membrane channel protein in chondrogenesis.

While the role of miR-138 in chondrogenesis remains unclear, its differential expression in the microarray from McAlinden *et al* suggests a functional role[8]. Further studies involving different pro-chondrogenic induction medias, different progenitor cells, or different culture systems may be necessary to better understand the impact of miR-138. Its reported anti-proliferation, anti-cytoskeleton remodeling, and anti-osteogenic roles suggest that it may be more involved during terminal hypertrophic differentiation [9,10]. The CPCs used in our studies did not express detectable levels of hypertrophic chondrocyte markers *COL10A1* mRNA or COLX protein suggesting that our cells did not reach that stage of differentiation. It would be interesting to upregulate miR-138 during the later stages of MSC chondrogenesis when MSCs typically undergo hypertrophy to see if it regulates terminal chondrocyte differentiation.

While CPCs have shown promising results in chondrogenic assays, proliferative cells isolated from osteoarthritic cartilage using differential adhesion to fibronectin (DAF) were not consistent in their multilineage differentiation potential. Others have used manual [3,11] or automated [12] clonal selection to choose cells based on proliferation rate and cell morphology or selected migratory cells from cartilage explants [13,14]. These approaches may be more efficient than DAF for selecting multipotent CPCs, but they dramatically reduce initial cell count which extends the time necessary to expand the cells for tissue engineering studies. This tradeoff between cell differentiation consistency and expansion timeline must be rectified for CPCs to become a clinically viable and cost-efficient biological tool.

Our proof-of-concept study utilizing a bi-culture system to geographically restrict osteogenic differentiation on a three-dimensional scaffold serves as an important foundation for future

osteochondral tissue construct development. Others have used similar a bi-culture design to maintain osteochondral explants[15,16] or multi-compartmental design to develop a joint microtissue model[17,18]. Our design allows for a continuous osteochondral tissue to form if appropriate progenitor cells and biochemical cues are applied. To complement the bi-culture system design, the Guilak lab has developed a scaffold and coating combination that can immobilize lentivirus onto geographically restricted regions of a scaffold[19,20]. This technology will allow scaffold-mediated, spatially restricted delivery of pro-chondrogenic and pro-osteogenic biochemical cues to further enhance layered differentiation of osteochondral tissue in future studies.

In all, the miR-181a/b-1 cluster can be used to upregulate anabolic pathways during *in vitro* CPC chondrogenesis. It does this while severely downregulating *AQP9* expression, though the signaling mechanism that connects miR-181a/b-1 to *AQP9* is yet unclear. Future studies of AQP9 should be conducted during *in vitro* chondrogenic assays to better understand its functional role during chondrocyte differentiation. Information learned from AQP9 may be critical for understanding *in vitro* and possibly *in vivo* chondrogenesis, or it may serve as a biomarker for chondroprogenitors. Lentiviral delivery of miR-181a/b-1 may be useful in combination with the bi-culture system we developed. However, methods for multipotent CPC selection and expansion must be advanced before they can be confidently used in osteochondral and cartilage tissue engineering.

5.2 References

1   Jiang, Y. *et al.* Human Cartilage-Derived Progenitor Cells From Committed Chondrocytes for Efficient Cartilage Repair and Regeneration. *Stem Cells Transl Med* **5**, 733-744 (2016). https://doi.org/10.5966/sctm.2015-0192

2   Levato, R. *et al.* The bio in the ink: cartilage regeneration with bioprintable hydrogels and articular cartilage-derived progenitor cells. *Acta Biomater* **61**, 41-53 (2017). https://doi.org/10.1016/j.actbio.2017.08.005

3   Anderson, D. E., Markway, B. D., Weekes, K. J., McCarthy, H. E. & Johnstone, B. Physioxia Promotes the Articular Chondrocyte-Like Phenotype in Human Chondroprogenitor-Derived Self-Organized Tissue. *Tissue Eng Part A* **24**, 264-274 (2018). https://doi.org/10.1089/ten.TEA.2016.0510

4   Neumann, A. J. *et al.* Human Articular Cartilage Progenitor Cells Are Responsive to Mechanical Stimulation and Adenoviral-Mediated Overexpression of Bone-Morphogenetic Protein 2. *PLoS One* **10**, e0136229 (2015). https://doi.org/10.1371/journal.pone.0136229

5   Lee, C. T., Risom, T. & Strauss, W. M. Evolutionary conservation of microRNA regulatory circuits: an examination of microRNA gene complexity and conserved microRNA-target interactions through metazoan phylogeny. *DNA Cell Biol* **26**, 209-218 (2007). https://doi.org/10.1089/dna.2006.0545

6   Berezikov, E. Evolution of microRNA diversity and regulation in animals. *Nat Rev Genet* **12**, 846-860 (2011). https://doi.org/10.1038/nrg3079

7   Aharon, R. & Bar-Shavit, Z. Involvement of aquaporin 9 in osteoclast differentiation. *J Biol Chem* **281**, 19305-19309 (2006). https://doi.org/10.1074/jbc.M601728200

8   McAlinden, A., Varghese, N., Wirthlin, L. & Chang, L. W. Differentially expressed microRNAs in chondrocytes from distinct regions of developing human cartilage. *PLoS One* **8**, e75012 (2013). https://doi.org/10.1371/journal.pone.0075012

9   Reichenberger, E., Aigner, T., von der Mark, K., Stöss, H. & Bertling, W. In situ hybridization studies on the expression of type X collagen in fetal human cartilage. *Dev Biol* **148**, 562-572 (1991). https://doi.org/10.1016/0012-1606(91)90274-7

10   Woods, A., Wang, G. & Beier, F. Regulation of chondrocyte differentiation by the actin cytoskeleton and adhesive interactions. *J Cell Physiol* **213**, 1-8 (2007). https://doi.org/10.1002/jcp.21110

11   Williams, R. *et al.* Identification and clonal characterisation of a progenitor cell sub-population in normal human articular cartilage. *PLoS One* **5**, e13246 (2010). https://doi.org/10.1371/journal.pone.0013246

12   Mantripragada, V. P. *et al.* Progenitor cells from different zones of human cartilage and their correlation with histopathological osteoarthritis progression. *J Orthop Res* **36**, 1728-1738 (2018). https://doi.org/10.1002/jor.23829

13   Koelling, S. *et al.* Migratory chondrogenic progenitor cells from repair tissue during the later stages of human osteoarthritis. *Cell Stem Cell* **4**, 324-335 (2009). https://doi.org/10.1016/j.stem.2009.01.015

14   Seol, D. *et al.* Chondrogenic progenitor cells respond to cartilage injury. *Arthritis Rheum* **64**, 3626-3637 (2012). https://doi.org/10.1002/art.34613

15   Kleuskens, M. W. A., van Donkelaar, C. C., Kock, L. M., Janssen, R. P. A. & Ito, K. An ex vivo human osteochondral culture model. *J Orthop Res* **39**, 871-879 (2021). https://doi.org/10.1002/jor.24789

16   Maglio, M., Tschon, M., Sicuro, L., Lolli, R. & Fini, M. Osteochondral tissue cultures: Between limits and sparks, the next step for advanced in vitro models. *J Cell Physiol* **234**, 5420-5435 (2019). https://doi.org/10.1002/jcp.27457

17   Lozito, T. P. *et al.* Three-dimensional osteochondral microtissue to model pathogenesis of osteoarthritis. *Stem Cell Res Ther* **4 Suppl 1**, S6 (2013). https://doi.org/10.1186/scrt367

18   Wendt, D., Jakob, M. & Martin, I. Bioreactor-based engineering of osteochondral grafts: from model systems to tissue manufacturing. *J Biosci Bioeng* **100**, 489-494 (2005). https://doi.org/10.1263/jbb.100.489

19   Brunger, J. M. *et al.* Scaffold-mediated lentiviral transduction for functional tissue engineering of cartilage. *Proc Natl Acad Sci U S A* **111**, E798-806 (2014). https://doi.org/10.1073/pnas.1321744111

20   Rowland, C. R. *et al.* Regulation of decellularized tissue remodeling via scaffold-mediated lentiviral delivery in anatomically-shaped osteochondral constructs. *Biomaterials* **177**, 161-175 (2018). https://doi.org/10.1016/j.biomaterials.2018.04.049

Chapter 6: Background and Motivation: DNA Methyltransferase 3a in Skeletal Development

6.1 Overgrowth and Intellectual Disabilities

Section 6.1 and its subsections have been adapted from a research article published in *Bone* by

Bell-Hensley *et al*[1].

While miRNAs offer one approach for guiding skeletal development, there are countless other

factors required to navigate the complexities of skeletal development. Recent clinical studies

identified causative mutations in a variety of epigenetic regulators in patients living with

overgrowth and intellectual disability (OGID) syndromes[2].

6.1.1 Clinical Characteristics

OGID syndromes are typified by length/height and/or head circumference ≥ 2 standard

deviations above the mean in addition to intellectual disabilities, such as autism-spectrum

disorders and anxiety[3,4]. Several neurodevelopmental disorders – including Tatton-Brown-

Rahman, Sotos, Malan, Weaver, Homocystinuria, 22q13 deletion, and Bannayan-Riley-

Ruvalcaba syndromes – meet the criteria for OGID[5]. While OGID syndromes share a few

hallmark phenotypes, there is a high degree of heterogeneity associated with OGID patients that

is poorly understood.

6.1.2 Causal Mutations

As multi-omic approaches become more accessible clinically, exome and genome sequencing

data have been collected from OGID patients to identify associated genetic variants. DNA

sequencing on a population of 710 individuals with OGID identified that ~44% of OGID

disorders are caused by mutations in 6 epigenetic genes: *NSD1*, *EZH2*, *EED*, *CHD8*, *HIST1H1E*,

and *DNMT3A*[2]. Epigenetic mechanisms affected by these causal mutations include regulation of transcription by modifying DNA methylation (*DNMT3A*), the methylation of histones (*NSD1*, *EZH2*, *EED*), and chromatin structure (*CHD8*, *HIST1H1E*)[2]. Each of these epigenetic regulators is involved in modulating the expression of numerous genes, making it difficult to identify a therapeutic approach that targets specific dysregulated genes. Further complicating mechanistic studies, diverse causal mutations have been identified in each of these genes including nonsense, missense, and frameshift mutations[2]. These complications necessitate comparing multiple mutations within each gene to better understand the molecular underpinnings associated with OGID phenotypes.

6.1.3 Tatton-Brown-Rahman Syndrome

One of the most commonly mutated genes in OGID patients is DNA methyltransferase 3A (*DNMT3A*)[2], a *de novo* methyl transferase that is critical for embryonic and postnatal development[6]. The first publications that identified[7] and confirmed[8] *DNMT3A* as a gene of interest for OGID found a number of different mutations in regions encoding the functional domains of *DNMT3A*. Patients with mutations in *DNMT3A* who exhibit OGID symptoms are diagnosed with Tatton-Brown-Rahman Syndrome (TBRS), also known as *DNMT3A* Overgrowth Syndrome (DOS)[4]. Methylomic analysis of peripheral blood cells from patients with TBRS found that different variants in *DNMT3A* result in differential disruption of DNA methylation. Missense mutations at the Arg882 (R882) position result in severe genome-wide demethylation while other *DNMT3A* mutations, including missense mutations and a 135 kb gene deletion, cause a more moderate reduction of methylation[9]. However, the severity of neurodevelopmental and skeletal abnormalities did not correlate strongly with mutation or methylomic profile, a phenomenon that is not well understood. *In vitro* models have demonstrated that the disease-

associated R882H and P904L mutations cause reductions in DNA methylation[10], and mouse models engineered to express *Dnmt3a* mutations (*Dnmt3a$^{R878H/+}$* and *Dnmt3a$^{P900L/+}$*; homologous to the human *DNMT3A$^{R882H/+}$* and *DNMT3A$^{P904L/+}$* mutations, respectively) have been generated to better understand the molecular mechanisms that cause TBRS. These mutant animals recapitulate many aspects of the human disorder, such as obesity, long bone overgrowth, and behavioral alterations[9,11]. While transcriptomics and methylomics have been used to characterize neuronal and hematopoietic phenotypes of these mouse models, the molecular underpinnings of skeletal overgrowth remain poorly understood.

6.2 DNA Methyl Transferases

To delineate molecular mechanisms responsible for the methylomic profiles and phenotypes associated with *DNMT3A* mutations in TBRS patients, we must understand how wild-type DNMTs function.

6.2.1 Types of DNA Methyltransferases

As previously noted, DNMT3A is a *de novo* methyl transferase. The broader DNMT family encompasses *de novo* and maintenance methyl transferases. In humans, there are two *de novo* DNMTs (DNMT3A and DNMT3B) and one maintenance DNMT (DNMT1). These classes are distinguished by their responsibilities: *de novo* DNMTs add new methyl groups while maintenance DNMTs preserve symmetry of methylation during DNA replication[12,13]. *De novo* DNMTs are most highly expressed during the embryonic development and the early stages of post-natal development while maintenance DNMTs are upregulated during early post-natal development and are sustained at a moderate level throughout life[6,12,14]. Both classes of DNMTs have been studied extensively, primarily in the context of development[14] and cancer[15].

6.2.2 Molecular Mechanism

There are several active domains present in DNMT enzymes[12,13]. There are six elements in the catalytic C-terminus domains (I, IV, VI, VIII, IX, and X) shared by all DNMTs that enable them to the target DNA and transfer methylation onto the DNA sequence. In the regulatory N-terminus domain, three elements are shared by all three DNMTs: the cysteine-rich ATRX zinc finger DNA-binding motif, the polybromo homology domain (PHD) which targets areas of DNA replication, and a chromatin binding element, nicknamed the PWWP domain based on its amino acid sequence (proline-tyrosine-tyrosine-proline). The maintenance DNMT (DNMT1) has two additional regulatory elements including a proliferating cell nuclear antigen-binding domain (PBD) and a nuclear localization signal (NLS). These domains allow DNMTs to regulate and maintain DNA methylation. The advent of whole genome bisulfite sequencing[16] and mapping[17] radically advanced studies of DNMTs by enabling researchers to quantify the impact of DNMTs on methylation at a whole genome level.

6.2.3 Role in Skeletal Tissues

DNMTs have been studied extensively in skeletal tissues during both development[6] and homeostasis[18,19]. Developmental studies in genetic knockout mice demonstrated that *Dnmt3b*[6] and *Dnmt1*[20] are necessary for embryos to survive until birth. In contrast, *Dnmt3a*^{-/-} mice survived for a few weeks after birth but were skeletally runted and exhibited symptoms of kyphosis[6]. *Dnmt3b*^{-/-} mice also showed embryonic growth defects with a significant reduction in size at embryonic day 11[6]. However, there have been many mouse models with heterozygous knockouts and mutations that result in mouse models of diseases[21]. The primary skeletal developmental disorder associated with the DNMT family is TBRS[1,7-9,11,22].

However, others have found dysregulation of methylation during skeletal disorders related to disruption of homeostasis such as OA, osteoporosis, and cancer[18,19]. Shen *et al* demonstrated that

Dnmt3b loss-of-function resulted in a progressive OA phenotype while its gain-of-function protected against OA[23]. Interestingly, Shen *et al* also found that treating chondrocytes with the pro-inflammatory cytokine IL-1β, which mimics the inflammatory OA joint environment, reduced expression of *Dnmt3b* in chondrocytes. Li *et al* found that mechanical unloading resulted in upregulation of *Dnmt1* which impaired osteogenesis in a mouse model of disuse osteoporosis[24]. Meanwhile, Zhang *et al* found that knocking down *Dnmt3a* in an *in vitro* model of disuse osteoporosis promoted osteogenic differentiation by upregulating key osteogenic regulators Runx2 and Opn as well as Wnt/β-catenin signaling[25]. Moreover, *Nishikawa* et al have indicated that osteoclast-specific *Dnmt3a* deficiency resulted in impaired osteoclastogenesis and caused mice to have a significant increase in trabecular bone volume and bone mass and protected against osteoporosis[26]. Combing the effects of enhanced osteogenesis and impaired osteoclastogenesis from the *Dnmt3a* knockout studies, there is a strong rationale to investigate bone properties in mouse models of TBRS that has *Dnmt3a* loss-of-function.

6.3 Summary of Aims

Here, we aim to characterize skeletal phenotypes and cellular underpinnings for those phenotypes in mouse models of TBRS, one of the many OGID syndromes. The most robust skeletal phenotype in OGID patients is skeletal overgrowth, but, due to a lack of OGID animal models, cellular mechanisms of overgrowth have not yet been studied in OGID syndromes. We hypothesized that there may be dysregulation of the growth plate during early periods of rapid post-natal skeletal growth that result in skeletal overgrowth (Chapter 7). Moreover, we predicted that there may be additional skeletal abnormalities caused by OGID-inducing mutations that have not yet been characterized because of the lack of OGID animal models (Chapter 8).

6.4 References

1 Bell-Hensley, A. *et al.* Skeletal abnormalities in mice with Dnmt3a missense mutations. *Bone* **183**, 117085 (2024). https://doi.org/10.1016/j.bone.2024.117085

2 Tatton-Brown, K. *et al.* Mutations in Epigenetic Regulation Genes Are a Major Cause of Overgrowth with Intellectual Disability. *Am J Hum Genet* **100**, 725-736 (2017). https://doi.org/10.1016/j.ajhg.2017.03.010

3 Manor, J. & Lalani, S. R. Overgrowth Syndromes-Evaluation, Diagnosis, and Management. *Front Pediatr* **8**, 574857 (2020). https://doi.org/10.3389/fped.2020.574857

4 Ostrowski, P. J. & Tatton-Brown, K. in *GeneReviews(®)* (eds M. P. Adam *et al.*) (© 1993-2023, University of Washington, Seattle. GeneReviews is a registered trademark of the University of Washington, Seattle, 1993).

5 Sabin, M. A., Werther, G. A. & Kiess, W. Genetics of obesity and overgrowth syndromes. *Best Pract Res Clin Endocrinol Metab* **25**, 207-220 (2011). https://doi.org/10.1016/j.beem.2010.09.010

6 Okano, M., Bell, D. W., Haber, D. A. & Li, E. DNA methyltransferases Dnmt3a and Dnmt3b are essential for de novo methylation and mammalian development. *Cell* **99**, 247-257 (1999). https://doi.org/10.1016/s0092-8674(00)81656-6

7 Tatton-Brown, K. *et al.* Mutations in the DNA methyltransferase gene DNMT3A cause an overgrowth syndrome with intellectual disability. *Nat Genet* **46**, 385-388 (2014). https://doi.org/10.1038/ng.2917

8 Tatton-Brown, K. *et al.* The Tatton-Brown-Rahman Syndrome: A clinical study of 55 individuals with. *Wellcome Open Res* **3**, 46 (2018). https://doi.org/10.12688/wellcomeopenres.14430.1

9 Smith, A. M. *et al.* Functional and epigenetic phenotypes of humans and mice with DNMT3A Overgrowth Syndrome. *Nat Commun* **12**, 4549 (2021). https://doi.org/10.1038/s41467-021-24800-7

10 Christian, D. L. *et al.* DNMT3A Haploinsufficiency Results in Behavioral Deficits and Global Epigenomic Dysregulation Shared across Neurodevelopmental Disorders. *Cell Rep* **33**, 108416 (2020).

11   Beard, D. C. *et al.* Distinct disease mutations in DNMT3A result in a spectrum of behavioral, epigenetic, and transcriptional deficits. *Cell Rep* **42**, 113411 (2023). https://doi.org/10.1016/j.celrep.2023.113411

12   Turek-Plewa, J. & Jagodziński, P. P. The role of mammalian DNA methyltransferases in the regulation of gene expression. *Cell Mol Biol Lett* **10**, 631-647 (2005).

13   Bestor, T. H. The DNA methyltransferases of mammals. *Hum Mol Genet* **9**, 2395-2402 (2000). https://doi.org/10.1093/hmg/9.16.2395

14   Chen, Z. & Zhang, Y. Role of Mammalian DNA Methyltransferases in Development. *Annu Rev Biochem* **89**, 135-158 (2020). https://doi.org/10.1146/annurev-biochem-103019-102815

15   Zhang, J., Yang, C., Wu, C., Cui, W. & Wang, L. DNA Methyltransferases in Cancer: Biology, Paradox, Aberrations, and Targeted Therapy. *Cancers (Basel)* **12** (2020). https://doi.org/10.3390/cancers12082123

16   Feil, R., Charlton, J., Bird, A. P., Walter, J. & Reik, W. Methylation analysis on individual chromosomes: improved protocol for bisulphite genomic sequencing. *Nucleic Acids Res* **22**, 695-696 (1994). https://doi.org/10.1093/nar/22.4.695

17   Xi, Y. & Li, W. BSMAP: whole genome bisulfite sequence MAPping program. *BMC Bioinformatics* **10**, 232 (2009). https://doi.org/10.1186/1471-2105-10-232

18   Shen, J., Abu-Amer, Y., O'Keefe, R. J. & McAlinden, A. Inflammation and epigenetic regulation in osteoarthritis. *Connect Tissue Res* **58**, 49-63 (2017). https://doi.org/10.1080/03008207.2016.1208655

19   Delgado-Calle, J. & Riancho, J. A. The role of DNA methylation in common skeletal disorders. *Biology (Basel)* **1**, 698-713 (2012). https://doi.org/10.3390/biology1030698

20   Li, E., Bestor, T. H. & Jaenisch, R. Targeted mutation of the DNA methyltransferase gene results in embryonic lethality. *Cell* **69**, 915-926 (1992). https://doi.org/10.1016/0092-8674(92)90611-f

21   Lyko, F. The DNA methyltransferase family: a versatile toolkit for epigenetic regulation. *Nat Rev Genet* **19**, 81-92 (2018). https://doi.org/10.1038/nrg.2017.80

22   Tovy, A. *et al.* Constitutive loss of DNMT3A causes morbid obesity through misregulation of adipogenesis. *Elife* **11** (2022). https://doi.org/10.7554/eLife.72359

23   Shen, J. *et al.* DNA methyltransferase 3b regulates articular cartilage homeostasis by altering metabolism. *JCI Insight* **2** (2017). https://doi.org/10.1172/jci.insight.93612

24   Li, B. *et al.* Overexpression of DNMT1 leads to hypermethylation of H19 promoter and inhibition of Erk signaling pathway in disuse osteoporosis. *Bone* **111**, 82-91 (2018). https://doi.org/10.1016/j.bone.2018.03.017

25   Zhang, M. *et al.* Downregulation of DNA methyltransferase-3a ameliorates the osteogenic differentiation ability of adipose-derived stem cells in diabetic osteoporosis via Wnt/β-catenin signaling pathway. *Stem Cell Res Ther* **13**, 397 (2022). https://doi.org/10.1186/s13287-022-03088-4

26   Nishikawa, K. *et al.* DNA methyltransferase 3a regulates osteoclast differentiation by coupling to an S-adenosylmethionine-producing metabolic pathway. *Nat Med* **21**, 281-287 (2015). https://doi.org/10.1038/nm.3774

Chapter 7: Dnmt3a Mutations Cause Skeletal Overgrowth

This chapter has been adapted from a research article published in *Bone* by Bell-Hensley *et al*[1].

7.1 Abstract

Irregular skeletal development has been linked to mutations in epigenetic regulators in overgrowth and intellectual disability syndromes. Overgrowth and intellectual disability syndromes in humans are typified by length/height and/or head circumference ≥ 2 standard deviations above the mean as well as intellectual disability and behavioral comorbidities, including autism and anxiety. Tatton-Brown-Rahman Syndrome is one type of overgrowth and intellectual disability syndrome caused by heterozygous missense mutations in epigenetic regulator DNA methyltransferase 3A (*DNMT3A*). Numerous *DNMT3A* mutations have been identified in Tatton-Brown-Rahman Syndrome patients and may be associated with varying phenotype severities of clinical presentation. Two such mutations are the R882H and P904L mutations which result in severe and mild methylation phenotypes, respectively. Mice with paralogous mutations (*Dnmt3a$^{P900L/+}$* and *Dnmt3a$^{R878H/+}$*) exhibit overgrowth in their long bones (e.g., femur, humerus), but the mechanisms responsible for their skeletal overgrowth remain unknown. We report that mature mice with the *Dnmt3a$^{P900L/+}$* or *Dnmt3a$^{R878H/+}$* mutation also exhibit tibial overgrowth. To understand the potential cellular mechanisms underlying this overgrowth, growth plate chondrocytes were assessed in juvenile mutant mice using quantitative static histomorphometry. These studies reveal that growth plate thickening is present during post-natal skeletal development and suggests a cellular lineage to investigate in future mechanistic studies. These findings may be also informative for skeletal characterization of other mouse models for overgrowth and intellectual disability syndromes.

7.2 Introduction

Mechanisms of overgrowth are understudied in mouse models of OGID, despite being highlighted as a hallmark phenotype in humans with these disorders. Early researchers predicted that overgrowth may result from increased proliferation, hypertrophy, or extracellular matrix production in growth plate chondrocytes[2]. More recent work has advanced the clinical understanding of genotype-phenotype correlations in OGID disorders, suggesting that the overgrowth may be caused by disruption of the PI3K/mTOR signaling pathway which can inhibit apoptosis and promote cell growth and proliferation[3,4]. However, the limited availability of well-characterized mouse models has made studying these mechanisms difficult. Given the overlap of skeletal phenotypes among OGID disorders, skeletal characterization of mouse models will play an important role in understanding biological mechanisms responsible for skeletal abnormalities associated with these diseases. Thus, studies of TBRS mouse models can provide a basis for studying skeletal overgrowth in mouse models of OGID.

In this study, biological mechanisms for overgrowth were examined in the $Dnmt3a^{R878H/+}$ and $Dnmt3a^{P900L/+}$ mouse models of TBRS. Previous work has reported overgrowth in long bones (e.g., femur, humerus), but studies to decipher the mechanisms driving these skeletal phenotypes are limited. Here, we report that mature mice harboring $Dnmt3a^{R878H/+}$ and $Dnmt3a^{P900L/+}$ mutations have tibia overgrowth. To determine the developmental origins of the skeletal overgrowth, growth plate chondrocytes were assessed in skeletally developing juvenile mice. Through analysis of mouse models of $Dnmt3a$ mutations, the role of this DNA methyltransferase in bone development and growth can be better understood, and this can be used as a case study for understanding skeletal phenotypes in other OGID disorders.

7.3 Methods

7.3.1 Animal Husbandry

Mice were housed in a room on a 12:12 hour light/dark cycle, with controlled room temperature (20-22°C) and relative humidity (50%). Individually ventilated home cages (36.2 x 17.1 x 13 cm) were supplied with corncob bedding and free access to water and standard laboratory chow (PicoLab Irradiated Rodent Diet 5053). Adequate measures were taken to minimize animal pain or discomfort, and all mice were group-housed in mixed-genotype, single-sex cages. All animal protocols were approved by the Institutional Animal Care and Use Committee and the Animal Studies Committee of Washington University in St. Louis, and in accordance with guidelines from the National Institutes of Health (NIH).

7.3.2 Transgenic animals

Dnmt3a$^{R878H/+}$ and *Dnmt3a$^{P900L/+}$* animals were generated as previously described[5,6]. Both mutant strains were backcrossed to C57BL6/J females (JAX Stock No. 000664) and propagated separately. Mutant males and WT females were used for the generation of experimental animals to avoid any differences in mothering from mutant dams. Mice were genotyped with ear DNA by PCR for either *Dnmt3a$^{R878H/+}$* or *Dnmt3a$^{P900L/+}$* mutations as previously described[5,6].

7.3.3 EchoMRI

Body composition was measured with whole-body quantitative magnetic resonance using an EchoMRI Body Composition Analyzer at the Washington University Diabetes Research Center, and experiments were performed as previously described[7]. In brief, live animals were placed in a plastic cylinder tube with a solid insert to limit movement, and the signal in response to a low-intensity electromagnetic field was used to measure the relaxation of spin curves, allowing for the quantification of fat and lean tissue volume. To standardize between recording days, measurements were calibrated to Canola oil prior to each recording session.

7.3.4 Tissue Collection

Animals were weighed prior to euthanasia, and hindlimbs were harvested from juvenile animals at postnatal day 27 (P27), and from mature animals at 30- to 36-weeks of age. Whole right hindlimbs from juvenile and mature mice were fixed and decalcified for paraffin-embedded histology. Left hindlimbs dissected from mature mice and left tibias from juvenile mice were wrapped in PBS-wetted gauze and frozen at -20°C. Left femurs from juvenile mice were stored in 70% ethanol at 4°C.

7.3.5 Bone length assessment

Bone length was measured in left tibias and femurs from mature mice. Before imaging, left hindlimbs from mature mice were thawed at room temperature for 2 hours and hindlimb bones were isolated by scalpel dissection. X-ray radiographs were taken with 6 s exposures at 45 kV (Faxitron Ultrafocus 100; Faxitron Bioptics, LLC) and the bones were measured using the "Measure" tool on Faxitron Vision Software (Version 2.3.1). As a secondary measure, bone lengths were also measured using a Vernier caliper which yielded similar results (data not shown). After X-ray radiography, tibias and femurs were wrapped in PBS-wetted gauze and frozen at -20°C.

7.3.6 Histology

Right hindlimbs from juvenile mice were dissected by cutting through the hip joint with a scalpel and dislocating the femoral head out of the joint. The hindlimbs were fixed in 10% neutral buffered formalin for 24-48 hours at room temperature. After fixation, the samples were briefly rinsed in PBS then decalcified in 14% EDTA for 14 days, refreshing the EDTA every 3-4 days. The decalcified hindlimbs were rinsed in distilled water then stored in DPBS at 4°C for up to 3 weeks or until they could be embedded in paraffin blocks. Paraffin-embedded tissues were sectioned in the sagittal plane to generate 10 μm thick tissue slices which were then mounted

onto glass microscopy slides. Mounted tissues were stained with toluidine blue or designated for immunohistochemistry (IHC). IHC staining was completed for proliferating cell nuclear antigen (PCNA) using a monoclonal antibody (Cell Signaling #13110) and a polyclonal goat anti-rabbit HRP secondary antibody (Agilent #P044801-2). After both types of staining, samples were covered with a mounting medium (Cytoseal™ XYL; Richard-Allan Scientific) and a glass coverslip. Brightfield imaging of stained slides was completed on a whole slide imaging system (Hamamatsu Photonics Nanozoomer 2.0-HT System) using a 20X magnification lens.

7.3.7 Growth plate analysis

Images of the toluidine blue-stained proximal tibia and distal femur growth plates from juvenile right hindlimbs were exported at 5X magnification. The images were imported into ImageJ software for analysis. Using a scale of 0.542 pixels/micron (verified by measuring scale bar), the thickness of the whole growth plate and each zone within the growth plate (resting, proliferating, and hypertrophic) were quantified. Since the growth plate thickness is not uniform across the entire growth plate, ten measurements were taken, evenly spaced across the width of the growth plate, for the full growth plate thickness as well as each zone within the growth plate. The average of the ten measurements was used as a representative thickness of the growth plate or growth plate zone. The sum of the thicknesses for the three zones (resting, proliferating, and hypertrophic) of each growth plate was compared to the total growth plate thickness and was required to have $\leq 5\%$ difference. For zones that added up to $> 5\%$ difference from the total growth plate thickness, all three zones were re-measured. Measurements were taken by one blinded assessor.

7.3.8 Proliferating Cell Nuclear Antigen Analysis

Images of the PCNA stained proximal tibia and distal femoral growth plate tissue sections from juvenile right hindlimbs were exported at 5X magnification. The images were imported into

ImageJ software for analysis. Using a scale of 0.542 pixels/micron (verified by measuring scale bar), the PCNA$^+$ cell density and average cross-sectional area were quantified. Briefly, the growth plate was selected using the ImageJ "Polygon Selection" tool and then the cross-sectional area of the growth plate was measured. Within the growth plate, PCNA$^-$ cells were removed using ImageJ tools (e.g., threshold, median filter, fill holes, wand, clear, fill, watershed). Remaining PCNA$^+$ cells were analyzed with the "Particle Analyzer" by filtering for particles size 0 to 500 μm and circularity 0.0 to 1.0. The total number of PCNA$^+$ cells and the area of each individual PCNA$^+$ cell were recorded, then the average PCNA$^+$ cell area and PCNA$^+$ cell density were calculated. Measurements were taken by one blinded assessor.

7.3.9 Statistical Analysis

Data were analyzed and plotted using GraphPad Prism 9.4.0. All analyses were performed using two-way ANOVAs using sex and genotype as sources of variation. Multiple comparisons were made between equal numbers of sex-matched, littermate-paired animals after correcting for multiple comparisons using the Šídák method unless otherwise noted. While *Dnmt3a* mutations are not known to cause prominent sexually dimorphic phenotypes in mice[6], significance testing was performed using two-way ANOVA to test for sexually-dimorphic and genotype effects, given the known sexual dimorphism in C57BL/6J skeletal development[8]. Unless indicated otherwise, ANOVA analysis results are displayed above each graph. Unless specified, descriptive statistics for each graph indicate mean with individual values represented as solid circles or square frames. Significance is indicated for comparisons that meet the threshold $p \leq 0.05$ unless otherwise indicated.

7.4 Results

7.4.1 Mutations in *Dnmt3a* cause long bone overgrowth in mature mice

The first publications characterizing heterozygous $Dnmt3a^{R878H/+}$ and $Dnmt3a^{P900L/+}$ mouse

models of TBRS report significantly longer femurs in male and female mutant mice compared to

wild-type (WT) littermates at 30- to 36-weeks old [5,6]. To fully assess the impact of *Dnmt3a*

mutations in long bones of the leg, we performed analysis of femur and tibia length in mature 30-

to 36-week-old male and female $Dnmt3a^{R878H/+}$ and $Dnmt3a^{P900L/+}$ mice by digital X-ray (Fig.

7.1A-D) and physically via Vernier caliper (data not shown). We observe a small significant

length increase in femurs and tibias in $Dnmt3a^{R878H/+}$ mutants and $Dnmt3a^{P900L/+}$ female mutants.

While there seems to be a genotype effect detected by ANOVA analysis for either mutation,

there is also a genotype-sex interaction effect in the $Dnmt3a^{P900L/+}$ group, indicating that there is

a larger effect size in the femur and tibia overgrowth in female $Dnmt3a^{P900L/+}$ mice. In summary,

the $Dnmt3a^{R878H/+}$ mutation causes robust femoral and tibial overgrowth while the $Dnmt3a^{P900L/+}$

mutation has a more severe overgrowth phenotype in female mice.
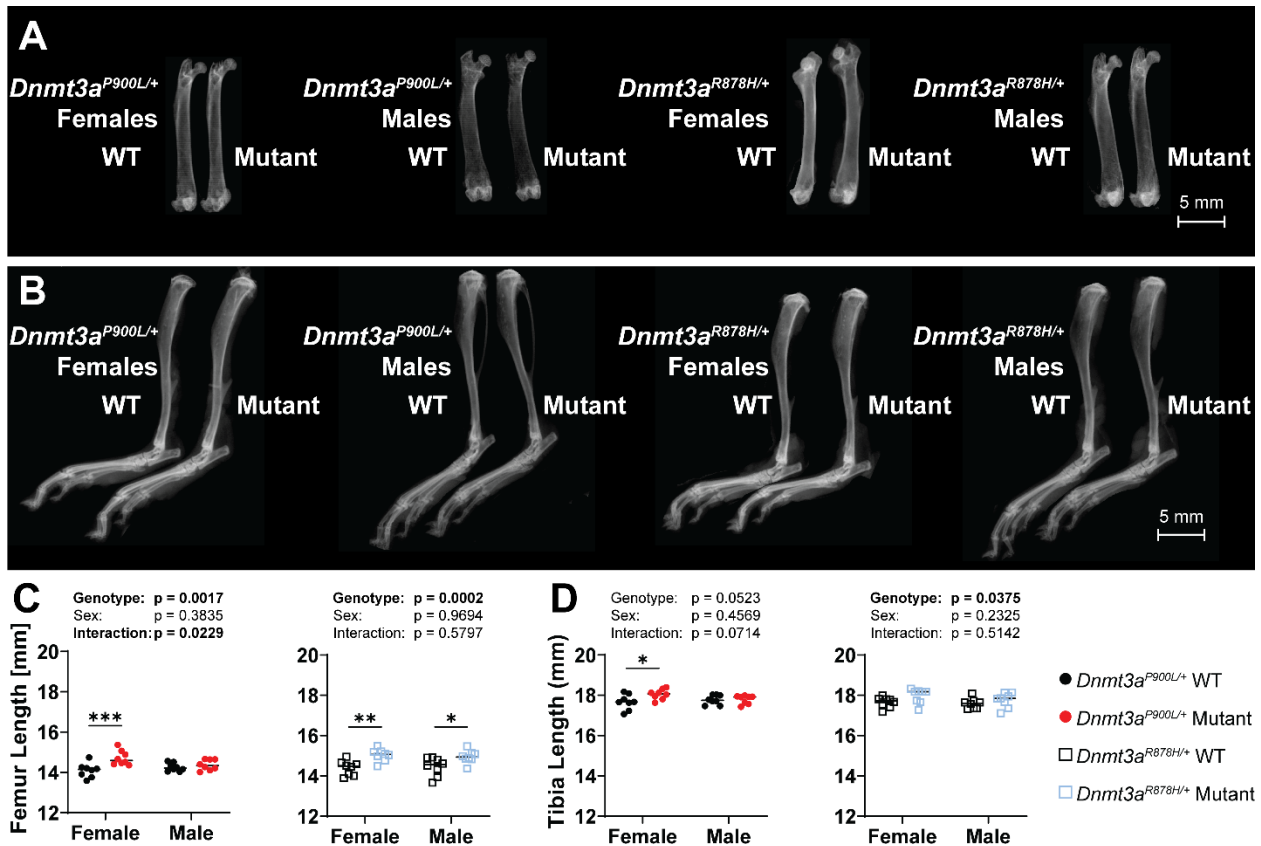
Figure 7.1. Mice with *Dnmt3a^P900L/+* or *Dnmt3a^R878H/+* mutation exhibit hindlimb long bone overgrowth. (A-B) Representative X-ray images of A) femurs and B) tibias from wild-type (WT) and mutant (*Dnmt3a^P900L/+* or *Dnmt3a^R878H/+*) mice aged 30-36 weeks. (C-D) Graphical representation of bone lengths for C) femurs and D) tibias. Symbols indicate significance in post hoc testing: * $p < 0.05$, ** $p < 0.01$, *** $p < 0.001$. n = 8/mutation/sex/strain. ANOVA terms are displayed above the graphs, bolded terms have $p < 0.05$.

7.4.2 Hindlimb long bone overgrowth is not driven by body weight

Given that increases in body weight can affect numerous skeletal phenotypes[9], and progressive obesity phenotypes have been reported in *Dnmt3a* mutants[5,6,10], we evaluated body weight in the mature mice to confirm that the *Dnmt3a* mutations were causing the limb overgrowth. Comparing body weights of mature mice, we found no difference in body weight between sex-matched pairs of *Dnmt3a^P900L/+* mice but a significant genotype effect in the *Dnmt3a^R878H/+* mice (Fig. 7.2A). The body weight for each mouse was plotted against its femur and tibia length (Fig. 7.2B, C). Clear correlations between body weight and tibia length were observed in both sexes of both mutants, and a positive correlation was observed between body weight and femur length in *Dnmt3a^R878H/+* mutants. Statistical analysis of linear regression was carried out for each group

and significant correlations between body weight and tibia length were identified in male and female $Dnmt3a^{R878H/+}$ mutants as well as male WT littermates of the $Dnmt3a^{R878H/+}$ mutants (Table 7.1). Considering that mice with longer bones are likely to have a larger body size and thus body weight, this was a predictable correlation between bone length and body size and did not show that skeletal overgrowth is purely a function of increased mechanical loading. To further investigate the role of mechanical loading on bone overgrowth, we measured body weight and body composition (via EchoMRI) in 27-day old mice to assess the potential role of loading on limb length. The $Dnmt3a^{R878H/+}$ mutants had small reductions in body weights and decreased lean mass, while the $Dnmt3a^{P900L/+}$ mutant mice had no change in overall weight, lean mass, or fat mass (Fig. 7.3). This shows that the mutants were not overweight at this developmental timepoint, and that bone length analyses should be indicative of genotype effects. Taken together, these results indicate that increased body weight is not responsible for the skeletal overgrowth observed in mice with either $Dnmt3a$ mutation.
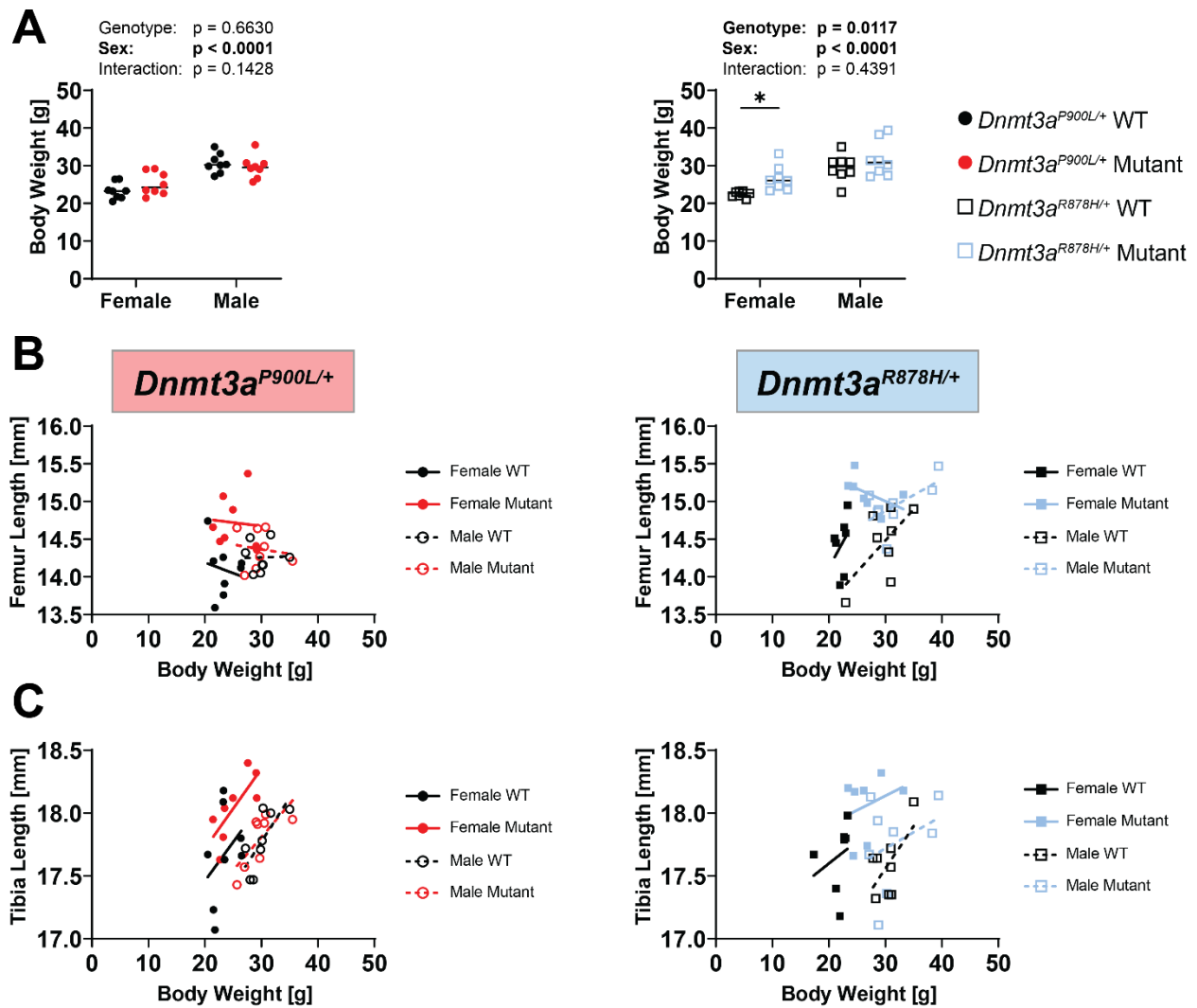
Figure 7.2. Hindlimb bone overgrowth in mice with *Dnmt3a^{P900L/+}* mutation correlates with body weight. A) Graphical representation of body weight in 30–36-week-old wild-type (WT) and mutant (*Dnmt3a^{P900L/+}* or *Dnmt3a^{R878H/+}*) mice. (B-C) Linear regression models assessing the correlation between body weight and bone length for B) femurs and C) tibias in WT and mutant mice. Symbols indicate significance in post hoc testing: * p < 0.05. n = 7-8/mutation/sex/strain. ANOVA terms are displayed above the graphs, bolded terms have p < 0.05. Linear regression statistics are available in Table 7.1.

Table 7.1 Linear regression analysis between bone length and body weight. Simple linear regression analysis for 30–36-week-old wild-type (WT) and mutant (*Dnmt3a^{P900L/+}* or *Dnmt3a^{R878H/+}*) mice. Bolded terms indicate p < 0.05.

Bone	Background	Sex	Genotype	p-value	R^2	Slope	Y-Intercept
FEMUR	*Dnmt3a^{P900L/+}*	Female	WT	0.6789	0.030540	0.06500	1.5220
			Mutant	0.8520	0.006287	0.04831	1.2250
		Male	WT	0.9292	0.001430	0.03327	1.0040
			Mutant	0.7421	0.019420	0.03562	1.0620
	Dnmt3a^{R878H/+}	Female	WT	0.4782	0.105000	0.17890	3.9890

TIBIA							
			Mutant	0.2409	0.26140	0.02487	0.6711
		Male	WT	0.0984	0.38900	0.04247	1.2710
			Mutant	0.1104	0.36860	0.02248	0.7235
TIBIA	$Dnmt3a^{P900L/+}$	Female	WT	0.3893	0.12550	0.06663	1.5610
			Mutant	**0.0286**	**0.57760**	**0.02219**	**0.5627**
		Male	**WT**	**0.0370**	**0.54300**	**0.02628**	**0.7929**
			Mutant	**0.0423**	**0.52410**	**0.02055**	**0.6129**
	$Dnmt3a^{R878H/+}$	Female	WT	0.5635	0.07099	0.05766	1.2590
			Mutant	0.5045	0.09363	0.03181	0.8583
		Male	WT	0.1105	0.36850	0.03619	1.1030
			Mutant	0.4064	0.11730	0.02890	0.9168
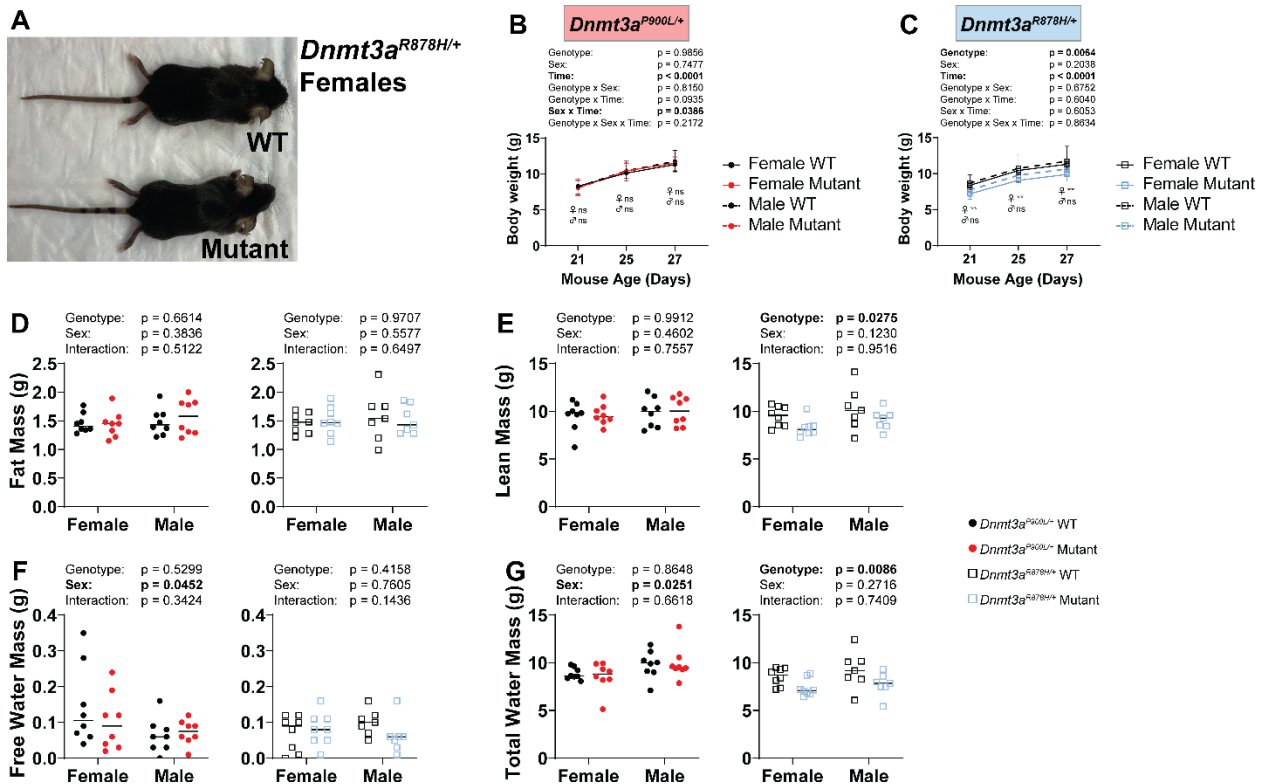
Figure 7.3. Juvenile *Dnmt3a* mutant mice do not have increased body weight. A) Gross morphology of a littermate pair of female wild-type (WT) and $Dnmt3a^{R878H/+}$ (mutant) mice. (B-C) Mouse weights from WT and mutant mice for B) $Dnmt3a^{P900L/+}$ and C) $Dnmt3a^{R878H/+}$ genotypes from 21 to 27 days old. (D-G) Graphical representation of EchoMRI body composition analysis of D) fat, E) lean, F) free water, and G) total water mass in $Dnmt3a^{P900L/+}$ and $Dnmt3a^{R878H/+}$ mice. Symbols indicate significance in post hoc testing: ** $p < 0.01$. $n = 8$/mutation/sex/strain.

7.4.3 Growth plate thickening is present in juvenile mice with *Dnmt3a* mutations

To identify developmental mechanisms involved in the skeletal overgrowth found in the mature mutant mice, juvenile mice were assessed. Male and female C57BL/6J mice begin a period of rapid growth around 4 weeks of age, suggesting that this would be an appropriate time point for growth plate analysis[11,12]. To better understand the mechanisms responsible for the observed femoral and tibial overgrowth trends in the mature mice, the thickness and proliferative activity in the growth plates of 27-day-old mutant mice were quantified as these are highly correlated with bone length and bone growth rate[13]. There was a slight trend toward growth plate thickening in the distal femur growth plate (Fig. 7.4A-B), though it was difficult to identify a consistent, representative thickness measurement in the irregularly shaped femoral growth plates. Growth plates in the proximal tibias of mutant juvenile mice were slightly thicker in mice with either the *Dnmt3a*$^{R878H/+}$ or *Dnmt3a*$^{P900L/+}$ mutation (Fig. 7.4C, E), suggesting that growth plate regulation was responsible for the tibial overgrowth observed in the mature mutant mice. This increase in thickness was not specific to the resting zone, proliferating zone, or hypertrophic zone of the growth plate, as each zone maintained a consistent proportion of the total growth plate thickness (Fig. 7.4D). In summary, the proximal tibial growth plate was significantly thicker in juvenile mutant mice and may explain the overgrowth observed in the tibias of mature mice.
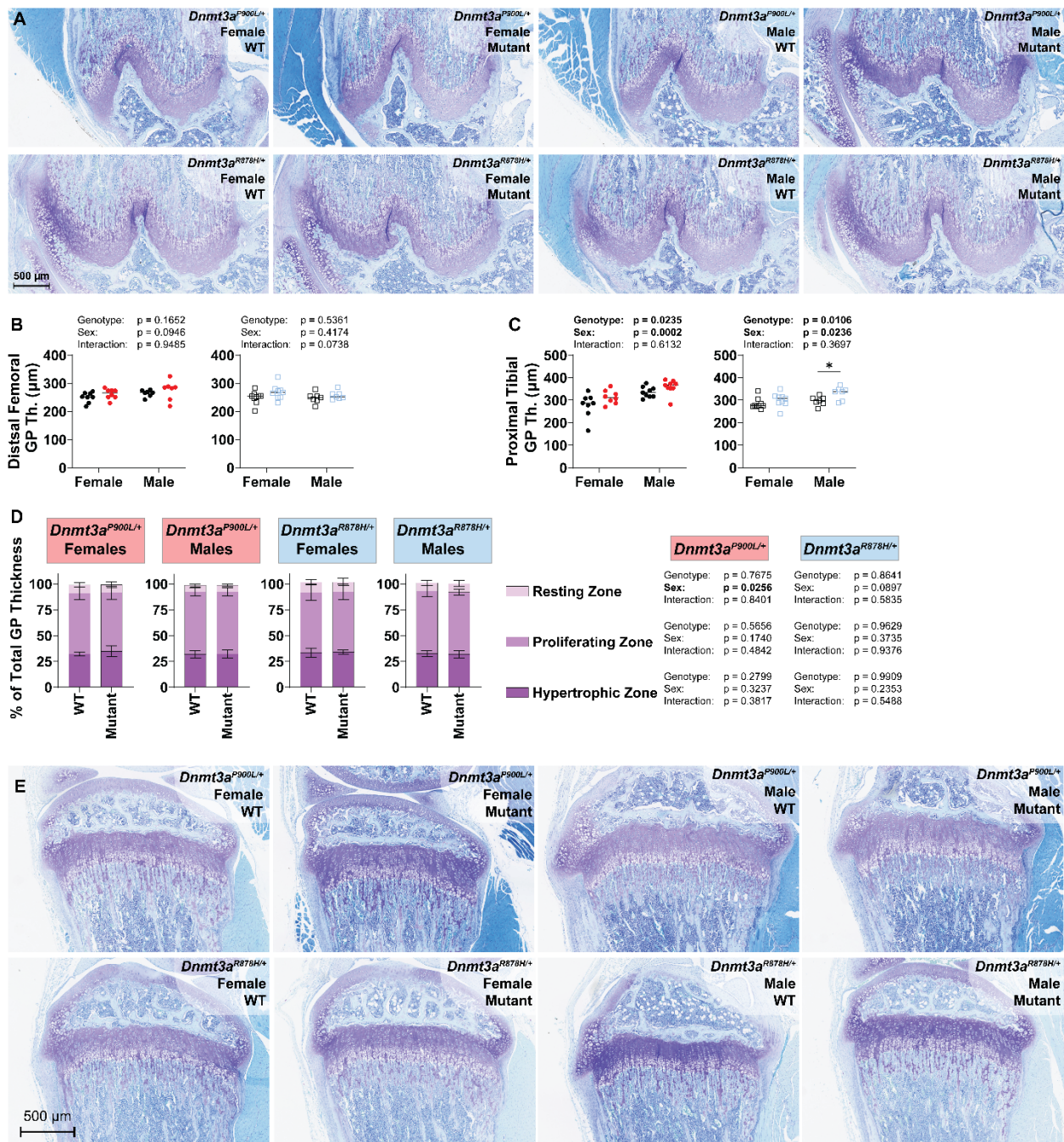
Figure 7.4. Growth plate thickening occurs in hindlimb long bones of *Dnmt3a* mutant mice at post-natal day 27. A) Representative toluidine blue histology images of distal femur growth plates from wild-type (WT) and mutant (*Dnmt3a^{P900L/+}* or *Dnmt3a^{R878H/+}*) mice at post-natal day 27. (B-C) Graphical representation of growth plate thickness for B) the distal femoral growth plate and C) the proximal tibial growth plate. D) Zonal proportions for the Resting Zone, Proliferating Zone, and Hypertrophic Zone in female and male mice. E) Representative toluidine blue histology images of proximal tibia growth plates from WT and mutant mice at post-natal day 27. Symbols indicate significance in post hoc testing: * $p < 0.05$. n = 8/mutation/sex/strain. Two-way ANOVA terms are displayed above the graphs and three-way ANOVA terms are displayed beside graph legends; bolded terms have $p < 0.05$.

7.4.4 Proliferating cell nuclear antigen does not explain growth plate thickening in juvenile mice

To further investigate growth plate activity, proliferation of growth plate chondrocytes was assessed via Proliferating Cell Nuclear Antigen (PCNA) staining in 27-day-old mice. In the distal femur growth plates, males with either the $Dnmt3a^{P900L/+}$ or the $Dnmt3a^{R878H/+}$ mutation trended towards having larger PCNA$^+$ cells with higher density than their WT littermates. However, PCNA$^+$ cells in the distal femur growth plate of females with either mutation trended towards being smaller and had lower cell density than their controls (Fig. 7.5A-C). Meanwhile, in the proximal tibia growth plate, there was no change in the density or cross-sectional area of PCNA$^+$ cells in mutant mice (Fig. 7.5D-F). These findings indicate that proliferative activity in the growth plate is unchanged at this time point and is not likely to be responsible for the skeletal overgrowth phenotype observed in mature $Dnmt3a$ mutant mice.
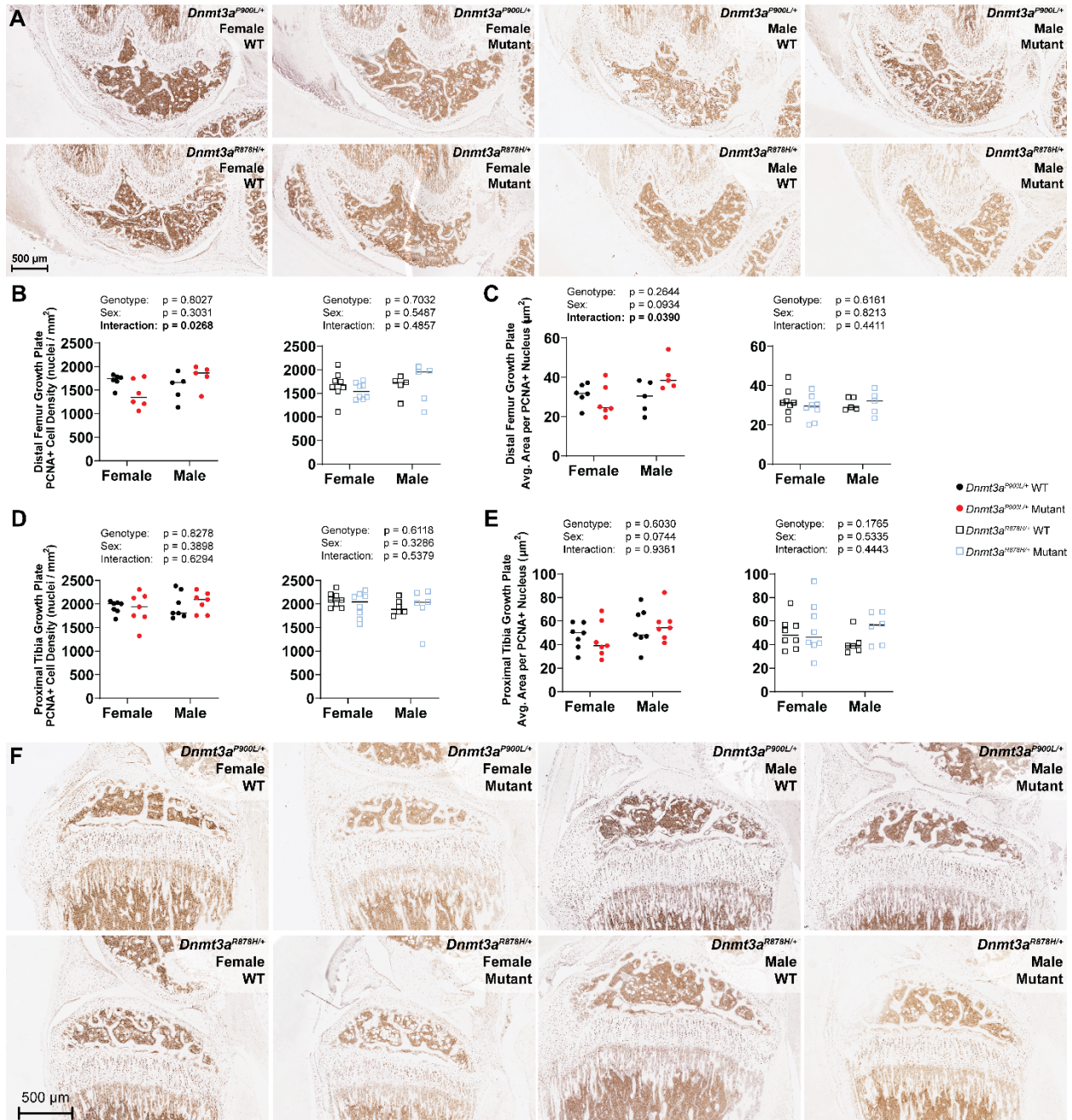
Figure 7.5. Proliferating cell nuclear antigen expression unchanged in *Dnmt3a* mutant mice at post-natal day 27. A) Representative PCNA IHC images from the distal femur growth plate WT and mutant mice. (B-C) Quantification of distal femur growth plate B) PCNA$^+$ cell density and C) PCNA$^+$ cell cross-sectional area. (D-E) Quantification of proximal tibia growth plate D) PCNA$^+$ cell density and E) PCNA$^+$ cell cross-sectional area. F) Representative PCNA IHC images from the proximal tibia growth plate WT and mutant mice. $n = 8$/mutation/sex/strain. ANOVA terms are displayed above the graphs, bolded terms have $p < 0.05$.

7.5 Discussion

The cellular and molecular mechanisms of skeletal overgrowth in OGIDs are poorly understood.

Genetic mouse models show promise in recapitulating skeletal, behavioral, and hematopoietic

changes observed in TBRS patients. The TBRS mouse models described herein can be used to study skeletal overgrowth associated with OGID and begin to identify the biological mechanisms responsible for their skeletal phenotypes. Previous *Dnmt3a* knockout studies have highlighted a critical role for this DNA methyltransferase enzyme in regulating musculoskeletal development[14]. Mice with homozygous *Dnmt3a* knockout are severely runted and have poor survival beyond 4 weeks of age while heterozygous *Dnmt3a* knockout mice survive to maturity, but develop obesity, extended long bones, and behavioral abnormalities[10,15]. Here, we use two genetic mouse models, *Dnmt3a$^{P900L/+}$* and *Dnmt3a$^{R878H/+}$*, to identify potential cellular mechanisms that may be driving their skeletal overgrowth.

There is hindlimb long bone overgrowth in 30- to 36-week-old *Dnmt3a$^{R878H/+}$* and *Dnmt3a$^{P900L/+}$* mutants, similar to the humerus and femur overgrowth that has been previously reported[5,6]. In both the femur[5,6] and tibia, a slightly larger effect size in female mutant mice suggests a potential sex-related effect of these mutations. Bone length is known to correlate with body mass suggesting that tibial overgrowth may be a result of increased body mass[9]. Earlier studies have reported that *Dnmt3a* mutant mice accumulate fat mass and overall body weight more quickly than WT littermates, particularly for female mice fed a high fat diet[6,10]. Meanwhile, it has been reported that male and female *Dnmt3a$^{P900L/+}$* mice have a trend towards increase in overall body weight driven by an increase in fat mass[6]. However, the analysis of body weights for mice fed standard chow reported here showed no increase in *Dnmt3a$^{P900L/+}$* mutants at 30- to 36- weeks of age, suggesting that the femoral and tibial overgrowth may be a result of other biological phenomena. While the overgrowth effect size is larger in the femurs[6], future skeletal evaluations of these TBRS mouse models, and perhaps other OGID mouse models, can study overgrowth in either the femur or the tibia.

Analyses in 27-day-old, skeletally developing mice show that this overgrowth may be driven by dysregulation of growth plate thickness during skeletal maturation. Mice with either the $Dnmt3a^{P900L/+}$ or $Dnmt3a^{R878H/+}$ mutation show growth plate thickening in the proximal tibia. PCNA staining suggests that there is no change in proliferating cell density or cell size with either mutation in the proximal tibia growth plate. However, this is only indicative that there is no change in PCNA positive cells at the one specific time point that was analyzed in this study (P27). Others have shown differences in tibial growth plate PCNA staining at post-natal day 7[16] and 14[17] and tibial epiphysis chondrocyte PCNA staining at embryonic days 16.5 and 18.5[18] in C57Bl/6 mice. Therefore, it is possible that with analysis of earlier or later time points, significant differences in PCNA positive cells may be found.

While there are differences in growth plate thickness, the cellular processes responsible for that overgrowth are unclear. Future studies to analyze *in vivo* BrdU incorporation may shed additional light on the involvement of proliferating growth plate cells in the overgrowth of tibias and femurs. It may also be interesting, in future studies, to examine ECM accumulation in the growth plate as another potential explanation for the observed increase in growth plate thickness. Due to the irregular shape of the distal femoral growth plate, future animal studies of TBRS and other OGID syndromes that focus on the proximal tibial growth plate may be most fruitful.

7.6 References

1   Bell-Hensley, A. *et al.* Skeletal abnormalities in mice with Dnmt3a missense mutations. *Bone* **183**, 117085 (2024). https://doi.org/10.1016/j.bone.2024.117085

2   Cohen, M. M. in *Clinical Genetics*   (eds Ann M. Willey, Thomas P. Carter, Sally Kelly, & Ian H. Porter) 153-169 (Academic Press, 1982).

3   Tatton-Brown, K. & Weksberg, R. Molecular mechanisms of childhood overgrowth. *Am J Med Genet C Semin Med Genet* **163C**, 71-75 (2013). https://doi.org/10.1002/ajmg.c.31362

4   Cytrynbaum, C. S., Smith, A. C., Rubin, T. & Weksberg, R. Advances in overgrowth syndromes: clinical classification to molecular delineation in Sotos syndrome and Beckwith-Wiedemann syndrome. *Curr Opin Pediatr* **17**, 740-746 (2005). https://doi.org/10.1097/01.mop.0000187191.74295.97

5   Smith, A. M. *et al.* Functional and epigenetic phenotypes of humans and mice with DNMT3A Overgrowth Syndrome. *Nat Commun* **12**, 4549 (2021). https://doi.org/10.1038/s41467-021-24800-7

6   Beard, D. C. *et al.* Distinct disease mutations in DNMT3A result in a spectrum of behavioral, epigenetic, and transcriptional deficits. *Cell Rep* **42**, 113411 (2023). https://doi.org/10.1016/j.celrep.2023.113411

7   Nixon, J. P. *et al.* Evaluation of a quantitative magnetic resonance imaging system for whole body composition analysis in rodents. *Obesity (Silver Spring)* **18**, 1652-1659 (2010). https://doi.org/10.1038/oby.2009.471

8   Glatt, V., Canalis, E., Stadmeyer, L. & Bouxsein, M. L. Age-related changes in trabecular architecture differ in female and male C57BL/6J mice. *J Bone Miner Res* **22**, 1197-1207 (2007). https://doi.org/10.1359/jbmr.070507

9   Jepsen, K. J., Silva, M. J., Vashishth, D., Guo, X. E. & van der Meulen, M. C. Establishing biomechanical mechanisms in mouse models: practical guidelines for systematically evaluating phenotypic changes in the diaphyses of long bones. *J Bone Miner Res* **30**, 951-966 (2015). https://doi.org/10.1002/jbmr.2539

10   Christian, D. L. *et al.* DNMT3A Haploinsufficiency Results in Behavioral Deficits and Global Epigenomic Dysregulation Shared across Neurodevelopmental Disorders. *Cell Rep* **33**, 108416 (2020).

11   Ferguson, V. L., Ayers, R. A., Bateman, T. A. & Simske, S. J. Bone development and age-related bone loss in male C57BL/6J mice. *Bone* **33**, 387-398 (2003). https://doi.org/10.1016/s8756-3282(03)00199-6

12   Brodt, M. D., Ellis, C. B. & Silva, M. J. Growing C57Bl/6 mice increase whole bone mechanical properties by increasing geometric and material properties. *J Bone Miner Res* **14**, 2159-2166 (1999). https://doi.org/10.1359/jbmr.1999.14.12.2159

13   Wilson, K. *et al.* Analysis of Association between Morphometric Parameters of Growth Plate and Bone Growth of Tibia in Mice and Humans. *Cartilage* **13**, 315S-325S (2021). https://doi.org/10.1177/1947603519900800

14   Nguyen, S., Meletis, K., Fu, D., Jhaveri, S. & Jaenisch, R. Ablation of de novo DNA methyltransferase Dnmt3a in the nervous system leads to neuromuscular defects and shortened lifespan. *Dev Dyn* **236**, 1663-1676 (2007). https://doi.org/10.1002/dvdy.21176

15   Tovy, A. *et al.* Constitutive loss of DNMT3A causes morbid obesity through misregulation of adipogenesis. *Elife* **11** (2022). https://doi.org/10.7554/eLife.72359

16   Eswarakumar, V. P. & Schlessinger, J. Skeletal overgrowth is mediated by deficiency in a specific isoform of fibroblast growth factor receptor 3. *Proc Natl Acad Sci U S A* **104**, 3937-3942 (2007). https://doi.org/10.1073/pnas.0700012104

17   Kondo, E. *et al.* Skeletal analysis of the long bone abnormality (lbab/lbab) mouse, a novel chondrodysplastic C-type natriuretic peptide mutant. *Calcif Tissue Int* **90**, 307-318 (2012). https://doi.org/10.1007/s00223-011-9567-0

18   Miao, D. *et al.* Impaired endochondral bone development and osteopenia in Gli2-deficient mice. *Exp Cell Res* **294**, 210-222 (2004). https://doi.org/10.1016/j.yexcr.2003.10.021

Chapter 8: Other Skeletal Anomalies in *Dnmt3a* Mutant Mice

This chapter has been adapted from a research article published in *Bone* by Bell-Hensley *et al*[1].

8.1 Abstract

Skeletal overgrowth is commonly reported in Tatton-Brown-Rahman syndrome patients along with several other skeletal developmental disorders such as joint hypermobility and kyphoscoliosis. These macroscopic disorders raise questions about what other skeletal abnormalities occur in Tatton-Brown-Rahman Syndrome patients. Earlier work from our group showed that growth plate chondrocyte activity is dysregulated in genetic mouse models of Tatton-Brown-Rahman Syndrome. When traced back to their cellular origin, growth plate chondrocytes are derived from the embryonic mesoderm. Given that *DNMT3A*, the gene that causes Tatton-Brown-Rahman Syndrome when mutated, is expressed in the embryonic mesoderm, we hypothesized that other mesoderm-derived cells may also be dysregulated during development. The goal of this study was to characterize skeletal phenotypes in genetic mouse models of Tatton-Brown-Rahman Syndrome and identify potential cellular mechanisms involved in any skeletal abnormalities. We report that mature mice with the $Dnmt3a^{P900L/+}$ or $Dnmt3a^{R878H/+}$ mutation exhibit cortical bone thinning and weakened bone mechanical properties. $Dnmt3a^{R878H/+}$ mutants also contain larger bone marrow adipocytes while $Dnmt3a^{P900L/+}$ mutants show no adipocyte phenotype compared to control animals. To understand the potential cellular mechanisms regulating these phenotypes, osteoblasts and osteoclasts were assessed in juvenile mutant mice using static and dynamic histomorphometry. These studies reveal new skeletal phenotypes in genetic mouse models of Tatton-Brown-Rahman

Syndrome and provide a rationale to extend clinical assessments of patients with this condition to include bone density and quality testing.

8.2 Introduction

While overgrowth is the most common skeletal abnormality reported in patients with Tatton-Brown-Rahman-Syndrome (TBRS), numerous comorbidities have been reported in individuals with TBRS or other OGID disorders, including musculoskeletal issues like joint hypermobility and kyphoscoliosis[2]. These complex phenotypes may have thus far obscured the recognition of additional skeletal phenotypes.

Developmentally, skeletal tissue is derived from the mesoderm (axial and appendicular skeleton) and neural crest (craniofacial skeleton)[3]. Developmental studies have shown that Dnmt3a expression is endogenously low in the mesoderm and much higher in the ectoderm at mouse embryonic day 7.5. However, Dnmt3a expression is ubiquitous by embryonic day 8.5[4]. Mesoderm-derived progenitor cells give rise to chondrocytes, adipocytes, and osteoblasts[5] while the ectoderm gives rise to the epidermis, the central nervous system, and peripheral nervous system[6]. TBRS patients present with skeletal and neural abnormalities, so it is logical to believe that this dysregulation stems from a developmental timepoint when the mutated *DNMT3A* is expressed in both the ectoderm and mesoderm. We have previously shown that growth plate chondrocytes are dysregulated by mutations in *Dnmt3a* which suggests that other mesoderm-derived cells, such as adipocytes and osteoblasts, may also be afflicted.

In this study, the *Dnmt3a^{R878H/+}* and *Dnmt3a^{P900L/+}* mouse models of TBRS were examined for skeletal abnormalities other than overgrowth. Here, we report that mature mice harboring *Dnmt3a^{R878H/+}* and *Dnmt3a^{P900L/+}* mutations have thinner femoral and tibial cortical bone and weakened femoral mechanical properties. We also report a mutation-specific increase in tibial

117

bone marrow adipocyte size. To determine the developmental origins of these phenotypes, osteoblasts and osteoclasts were assessed in skeletally developing juvenile mice. Through analysis of mouse models with *Dnmt3a* mutations, the role of this DNA methyltransferase in bone development and growth can be better understood. This can be used as a case study for understanding skeletal phenotypes in other OGID disorders.

8.3 Methods

8.3.1 Animal Husbandry
Mice were housed as previously described in *Section 7.3.1* (Animal Husbandry).

8.3.2 Transgenic animals
Dnmt3a$^{R878H/+}$ and *Dnmt3a$^{P900L/+}$* animals were generated and genotyped as previously described in *Section 7.3.2* (Transgenic animals).

8.3.3 Tissue Collection
Animals were weighed prior to euthanasia, and hindlimbs was harvested from juvenile animals at postnatal day 27 (P27), and from mature animals at 30- to 36-weeks of age. Whole right hindlimbs from mature mice were fixed and decalcified for paraffin-embedded histology. Left hindlimbs dissected from mature mice were wrapped in PBS-wetted gauze and frozen at -20°C for micro-computed tomography assessment, biomechanical testing, and osmium staining. Left femurs from juvenile mice were stored in 70% ethanol at 4°C until they were embedded in methyl methacrylate (MMA) for histology.

8.3.4 Micro-computed tomography
Whole bone 3D micro-computed tomography (µCT) was performed on left femurs and tibias from mature mice using standard methods[7]. Before imaging, left hindlimbs from mature mice previously dissected for bone length assessments were thawed at room temperature for 2 hours. Up to 5 femurs or 5 tibias were embedded in 2% agarose gel (w/v in distilled water) and scanned

in a cabinet µCT scanner (Scanco µCT50; SCANCO Medical AG, Brüttisellen, Switzerland) and the images were analyzed with Scanco Eval Program with a lower threshold of 350. Analyzed regions for the femur include the mid-diaphysis (midpoint of bone +/- 50 slices) for cortical bone outcomes and the distal metaphysis (150 slices leading up to the most proximal slice of the distal growth plate) for trabecular bone outcomes. For the tibia, the whole bones were analyzed for total volume, bone volume, and marrow volume for mid-diaphysis (midpoint of bone +/- 50 slices) cortical bone indices. After µCT radiography, tibias and femurs were wrapped in PBS-wetted gauze and frozen at -20°C for subsequent biomechanical analysis or osmium staining.

8.3.5 Biomechanical analysis

Three-point bend testing was performed on left femurs from mature mice after scans were taken for bone length and µCT analyses, following published guidelines[8]. Before testing, the femurs were thawed at room temperature for 2 hours. Excess tissues were removed from the femurs using forceps and gauze. Femur length was measured with a Vernier caliper and the midpoint of the bone was marked with a pencil. A material testing machine (ElectroPuls E1000; Instron) was set up with a 7mm span and femurs were placed into the load frame with the femoral condyles facing up and the proximal end of the bone positioned on the left side. Femurs were manually positioned and loaded to approximately -0.3N before switching to the machine's load control. A pre-load of -0.5 N was applied for 5 seconds then a sine wave function (1 Hz frequency, 3.75N amplitude, 5 cycles, 90° starting phase) was used to help pre-condition the bone. Immediately after pre-conditioning, the machine applied a ramp to failure test with a ramp rate of 0.1 mm/s. Each femur was observed during testing to ensure the bone did not shift or experience other phenomena that could affect mechanical readouts. Bones were loaded until complete fracture then the loading program was manually stopped, and the test data was saved. Force-displacement

data were analyzed to determine structural mechanical properties (e.g., maximum load) and were also used to estimate material properties (e.g., maximum stress) as described[8].

8.3.6 Osmium staining and analysis

Osmium staining was performed on left tibias from mature mice as described in previous publications[9,10]. Prior to fixation, left hindlimbs from mature mice previously dissected for bone length and μCT assessments were thawed at room temperature for 2 hours. Excess tissues were removed from the tibias using forceps and gauze. Bones were then fixed in 10% NBF for 24 hours at room temperature. Fixed bones were rinsed in distilled water and then decalcified using 14% EDTA (pH 7.4) for 14 days, refreshing the EDTA every 3-4 days. Decalcified bones were rinsed in distilled water and then stored in DPBS at 4°C until osmium staining (< 2 weeks). Decalcified bones were stained in 1 mL of a 1% osmium tetroxide (Electron Microscopy Services), 2.5% potassium dichromate (Sigma-Aldrich) solution in 1X PBS for 48 hours at room temperature, then rinsed with distilled water. Osmium-stained samples were stored in 1X PBS at 4°C until μCT scanning (< 2 weeks). Up to 11 tibias were embedded in 2% agarose gel (w/v in distilled water) and scanned with 10 μm voxel resolution using a Scanco μCT50 (SCANCO Medical AG), and the radiographs were analyzed with Scanco Eval Program. The entire lengths of the tibias were scanned and the proximal metaphysis (200 slices distal to the proximal growth plate) of each tibia was contoured and analyzed with a lower threshold of 400. This threshold detects osmium-stained bone marrow adipose tissue without detecting any of the demineralized bone. Contours and analyses were completed by one blinded assessor. After μCT scanning, the bones were stored in 1X PBS at 4°C for future analysis.

8.3.7 Dynamic histomorphometry

Dynamic histomorphometry was performed on left femurs from juvenile mice following established protocols[11,12]. Briefly, the mice were given intraperitoneal injections of calcein

(10 mg/kg; Sigma–Aldrich) at 21 days of age and alizarin (30 mg/kg; Sigma–Aldrich) at 25 days of age to label the endosteal and periosteal surfaces. Bones were stored in 70% ethanol at 4°C until MMA embedding. These femurs were embedded in MMA as previously described[13], and measured using a Vernier caliper to locate the mid-diaphysis. Three transverse sections were cut from the mid-diaphysis region using a saw microtome (SP1600 Saw Microtome; Leica) and mounted onto glass microscopy slides using a mounting medium (Cytoseal™ XYL; Richard-Allan Scientific) and a glass coverslip. Sections were imaged using a confocal microscope (DMi8; Leica) with the following settings: 10X lens, 2048x2048 resolution, 400 Hz scan speed, 20 µm z-stack size, and 5 z-stack images. Images were analyzed using BIOQUANT OSTEO (BIOQUANT Image Analysis). Analysis was completed by one blinded assessor.

8.3.8 Osteoclast assessment

To analyze osteoclast number, additional transverse sections were cut from the left femurs of juvenile mice that were embedded in MMA for dynamic histomorphometry. These slides were cut at thickness of 10 µm and mounted onto glass microscopy slides. Mounted tissues were stained using a standard tartrate-resistant acid phosphatase (TRAP) staining technique, then covered with a mounting medium (Cytoseal™ XYL; Richard-Allan Scientific) and a glass coverslip. Brightfield imaging of stained slides was completed on a whole slide imaging system (Hamamatsu Photonics Nanozoomer 2.0-HT System) using a 20X magnification lens. Images of the TRAP-stained femur mid-diaphysis from each juvenile left femur were exported at 10X magnification. The images were imported into ImageJ software for analysis. Using a scale of 1.084 pixels/micron (verified by measuring scale bar), periosteal bone surface, number of osteoclasts, and bone surface area of each osteoclast were quantified. Briefly, the endocortical surface of the bone was outlined using the ImageJ "Polygon Selection" tool and then the

perimeter of the endocortical surface was measured. Along the endocortical surface, the bone surface area of each osteoclast was traced using the ImageJ "Freehand Line" tool and the length of the line was measured. The total number of osteoclasts and the bone surface are of each osteoclast was recorded, then the osteoclast number per bone surface and osteoclast surface per bone surface were calculated. Measurements were taken by one blinded assessor.

8.3.9 Histology

Right hindlimbs from mature mice were dissected by cutting through the hip joint with a scalpel and dislocating the femoral head out of the joint. The hindlimbs were fixed in 10% neutral buffered-formalin for 24-48 hours at room temperature. After fixation, the samples were decalcified in formic acid (ImmunoCal™ Decalcifier; StatLab) for 3-4 days, refreshing the EDTA every 1-2 days. The decalcified hindlimbs were rinsed in distilled water then stored in DPBS at 4°C for up to 3 weeks or until they could be embedded in paraffin blocks. Paraffin-embedded tissues were sectioned in the sagittal plane to generate 10 µm thick tissue slices which were then mounted onto glass microscopy slides. Mounted tissues were stained using a standard hematoxylin and eosin (H&E) staining technique, then covered with a mounting medium (Cytoseal™ XYL; Richard-Allan Scientific) and a glass coverslip. Brightfield imaging of stained slides was completed on a whole slide imaging system (Hamamatsu Photonics Nanozoomer 2.0-HT System) using a 20X magnification lens.

8.3.10 Bone marrow adipose tissue quantification

Images of the H&E-stained proximal tibia metaphysis from the right hindlimb were exported at 10X magnification. The images were imported into ImageJ software for analysis. Using a scale of 1.084 pixels/micron (verified by measuring scale bar), the bone marrow adipocyte cell density and average cross-sectional area were quantified. Briefly, the bone marrow cavity was selected using ImageJ tools (e.g., threshold, median filter, fill holes, wand) and then the cross-sectional

area of the marrow cavity was measured. Within the bone marrow cavity, the ImageJ tool "Particle Analyzer" was used to select adipocyte-like shapes in the image by filtering for particles sized 100 to "infinity" µm and circularity 0.0 to 1.0. Non-adipocytes were manually removed using ImageJ tools (e.g., median filter, fill holes, wand, clear, fill, watershed). This manual selection step was repeated by three independent, blinded assessors. Remaining adipocytes were analyzed with the "Particle Analyzer" by filtering for particles sized 100 to 4,000 µm and circularity 0.5 to 1.0. The total number of adipocytes and the area of each individual adipocyte were recorded, then the average adipocyte area was calculated. Values recorded by each of the three assessors were averaged to give an accurate representation.

8.3.11 Statistical Analysis

Data were analyzed and plotted using GraphPad Prism 9.4.0. All analyses were performed using two-way ANOVAs using sex and genotype as sources of variation. Multiple comparisons were made between equal numbers of sex-matched, littermate-paired animals after correcting for multiple comparisons using the Šídák method unless otherwise noted. While *Dnmt3a* mutations are not known to cause prominent sexually dimorphic phenotypes in mice[14], significance testing was performed using two-way ANOVA to test for sexually-dimorphic and genotype effects, given the known sexual dimorphism in C57BL/6J skeletal development[15]. Unless indicated otherwise, ANOVA analysis results are displayed above each graph. Unless specified, descriptive statistics for each graph indicate mean with individual values represented as solid circles or square frames. Significance is indicated for comparisons that meet the threshold $p \leq 0.05$ unless otherwise indicated.

8.4 Results

8.4.1 Cortical bone thinning in mature mice with *Dnmt3a* mutations

To investigate if additional skeletal abnormalities occurred in $Dnmt3a^{P900L/+}$ and $Dnmt3a^{R878H/+}$ mutant mice[14,16], micro-computed tomography (μCT) analysis was carried out on 30- to 36-week-old mice. Femoral mid-diaphysis cortical bone thickness was significantly reduced in mice with either the $Dnmt3a^{P900L/+}$ or the $Dnmt3a^{R878H/+}$ heterozygous mutation (Fig. 8.1A, B). Cortical tissue mineral density and marrow volume were unchanged with either mutation (Fig. 8.1C, D). While there were sex differences in this data, these differences were expected given the known sexual dimorphism in the skeletal development of C57BL/6J mice[15]. As such, post-hoc comparisons were not made between male and female groups. Similar trends in mid-diaphysis cortical bone thickness and tissue mineral density were also observed in tibias from both the $Dnmt3a^{P900L/+}$ and the $Dnmt3a^{R878H/+}$ mutant mice (Fig. 8.2A-C). However, there was a reduction in tibia marrow volume found only in the $Dnmt3a^{R878H/+}$ female mice (Fig. 8.2D). In summary, mice with either the $Dnmt3a^{P900L/+}$ or $Dnmt3a^{R878H/+}$ mutation had thinner cortical bone in the mid-diaphysis of their femurs and tibias, and female mice with the $Dnmt3a^{R878H/+}$ mutation had reduced tibia marrow volume.
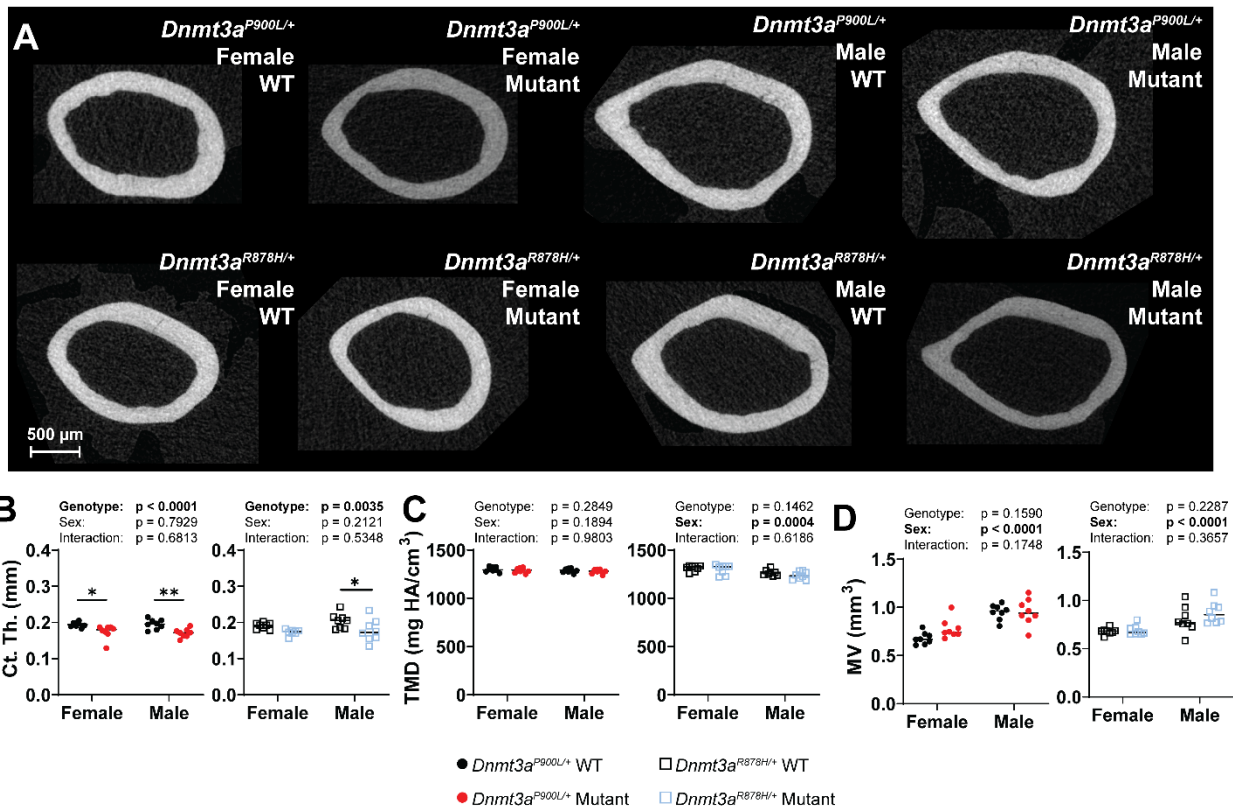
Figure 8.1. Mature mice with Dnmt3a mutations have thinner cortical bone in the femur mid-diaphysis. A) Representative images of cortical bone from femurs of wild-type (WT) and mutant (*Dnmt3a$^{P900L/+}$* or *Dnmt3a$^{R878H/+}$*) mice. (B-D) Graphical representation of μCT B) cortical thickness, C) cortical tissue mineral density and D) marrow volume data. Symbols indicate significance in post hoc testing: * $p < 0.05$, ** $p < 0.01$. *n* = 8/mutation/sex/strain. ANOVA terms are displayed above the graphs, bolded terms have $p < 0.05$.
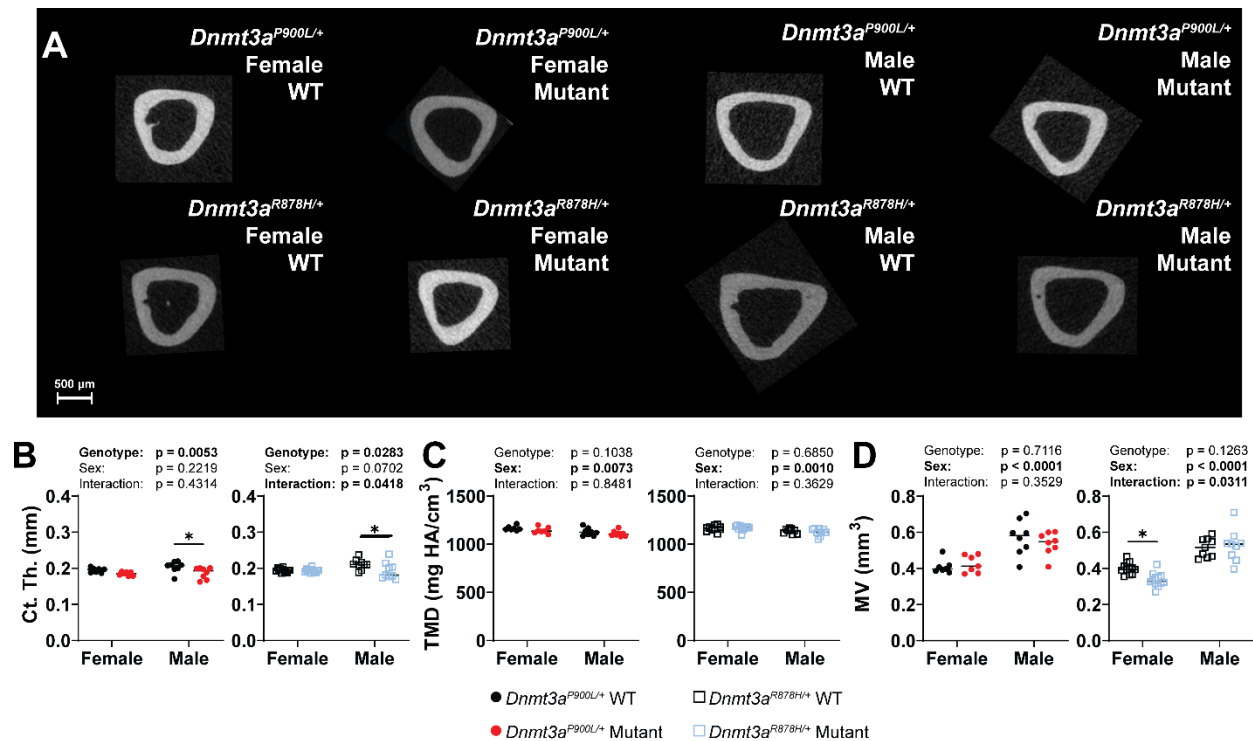
Figure 8.2. Mature mice with Dnmt3a mutations have thinner cortical bone in the tibia mid-diaphysis. A) Representative images of cortical bone from tibias of wild-type (WT) and mutant ($Dnmt3a^{P900L/+}$ or $Dnmt3a^{R878H/+}$) mice. (B-D) Graphical representation of μCT B) cortical thickness, C) cortical tissue mineral density and D) marrow volume data. Symbols indicate significance in post hoc testing: * $p < 0.05$. n = 7-12/mutation/sex/strain. ANOVA terms are displayed above the graphs, bolded terms have $p < 0.05$.

8.4.2 Mature mice with *Dnmt3a* mutations have altered bone biomechanics

To assess if the thinner cortical bone phenotype translates to altered bone mechanical properties,

ex vivo three-point bend testing was carried out on femurs from 30- to 36-week-old mice. Bones

from mutant mice had significantly lower stiffness, yield load, and maximum load than the

femurs of WT littermates (Fig. 8.3A-E). ANOVA on the $Dnmt3a^{P900L/+}$ yield load data indicated

a significant genotype-sex interaction effect indicating that the $Dnmt3a^{P900L/+}$ mutation had a

larger effect size in females than it did in males. Biomechanical properties were normalized to

the femoral mid-diaphysis cross-sectional area (measured using μCT) to estimate material

properties. When normalized, mutant mice had reduced Young's modulus, yield stress, and

ultimate stress (Fig. 8.3F-H). Of note, the post-yield displacement and work-to-fracture for these

mice remained the same (Fig. 8.3I, J) suggesting that the brittleness of the bones was unchanged.

In summary, the femurs of mutant mice were less stiff and weaker than those of WT mice,

consistent with their reduced cortical bone thickness.
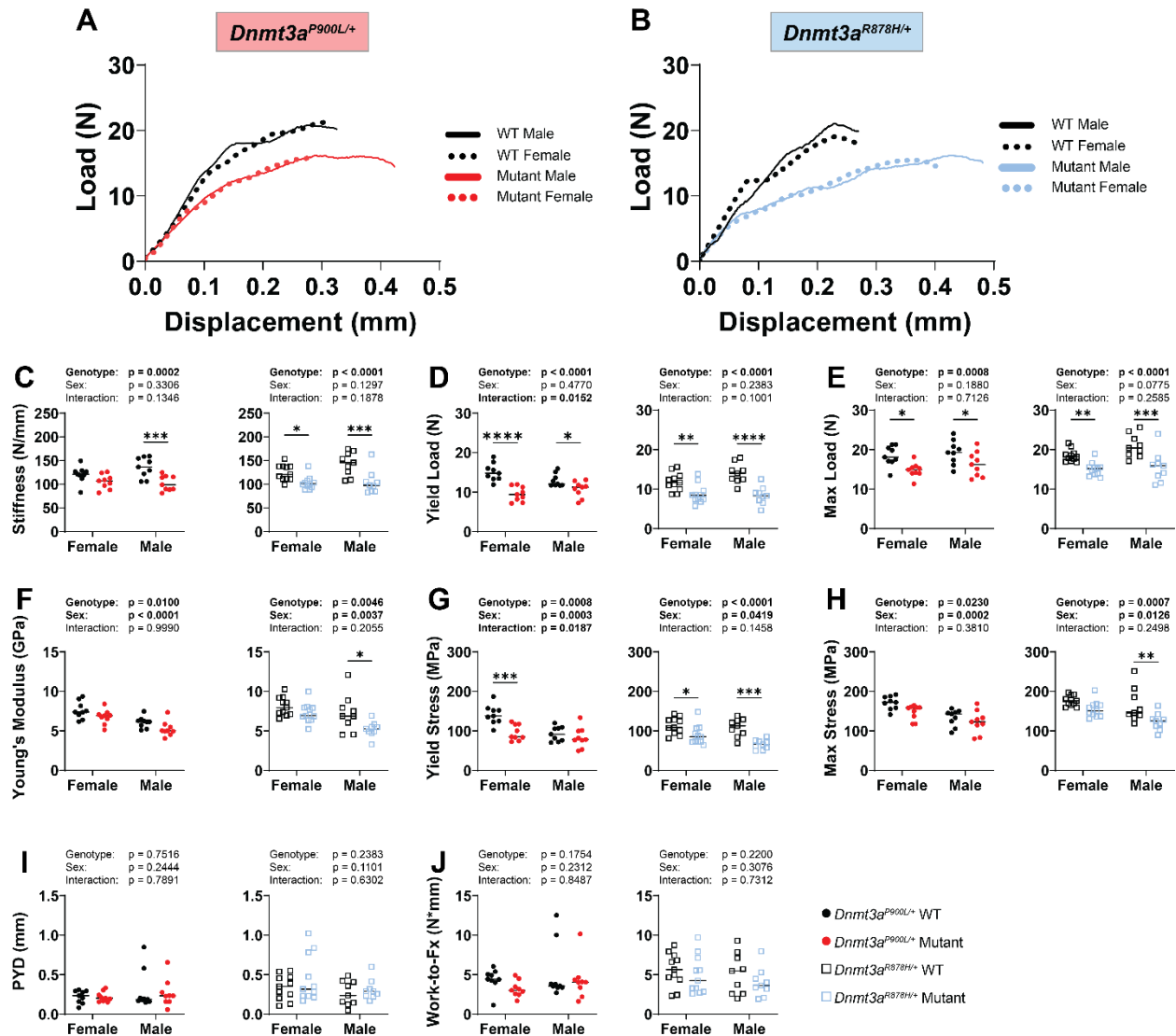
Figure 8.3. Mechanical and material properties are altered in mature mice with mutations in *Dnmt3a*. (A-B) Representative load-displacement curves from three-point bend testing of A) *Dnmt3a$^{P900L/+}$* and B) *Dnmt3a$^{R878H/+}$* littermate pairs aged 30-36 weeks. (C-E) Graphical representation of C) stiffness, D) yield load, and E) maximum load. F-G) Mechanical properties normalized to the femur mid-diaphysis cross-sectional area to measure F) Young's Modulus, G) Yield Stress, and H) Max Stress. (I-J) Graphical representation of I) post-yield displacement and J) work-to-fracture data. Symbols indicate significance in post hoc testing: * $p < 0.05$, ** $p < 0.01$, *** $p < 0.001$, **** $p < 0.0001$. $n = 9\text{-}11$/mutation/sex/strain. ANOVA terms are displayed above the graphs, bolded terms have $p < 0.05$.

8.4.3 Osteoblast activity and osteoclast number unchanged in juvenile *Dnmt3a* mutants

Mice were analyzed at 3- to 4-weeks of age to discern the cellular basis for cortical thinning.

TRAP staining of transverse sections at the femur mid-diaphysis indicated that there was no

significant change in osteoclast number or osteoclast surface per bone surface on the endocortical surface (Fig. 8.4A-C). On the other hand, dynamic histomorphometry on the femur mid-diaphysis in these juvenile mice indicated that there was no change in bone formation indices in mutant mice, suggesting that there was no difference in osteoblast activity between WT and mutant mice (Fig. 8.5A-C). Of note, the WT and mutant mice in the $Dnmt3a^{R878H/+}$ litters did not consistently take up the alizarin dye (red color in Fig. 8.5A) which made it difficult to draw conclusions about these mice. Mice that did not take up the alizarin dye had their bone formation rate (BFR) for both the endocortical (Ec.) and periosteal (Ps.) surface set to 0.15 µm/day based on minimum values established by Foldes *et al*[17]. Mineral apposition rate and mineralizing surface per bone surface values are also unchanged between WT and mutant animals (Fig. 8.5D-G). In summary, it was unclear if osteoblasts or osteoclasts were responsible for the cortical thinning phenotype observed in mature *Dnmt3a* mutant mice.
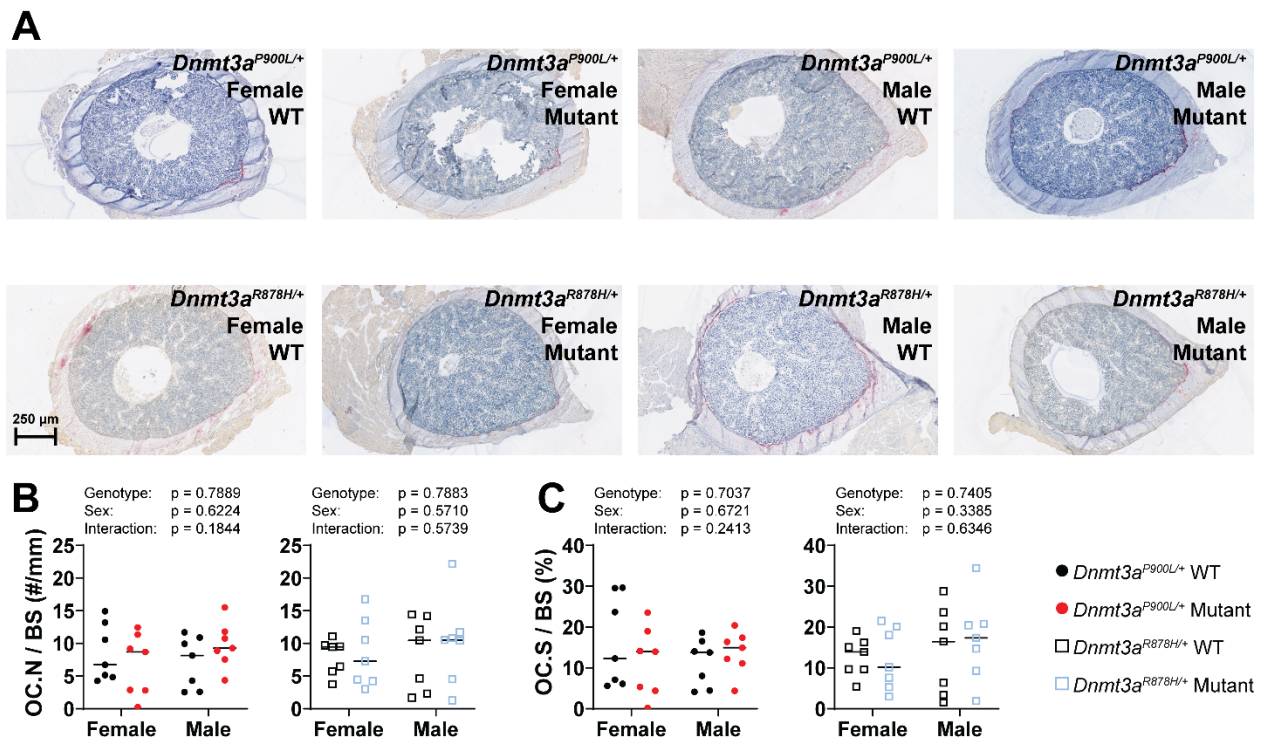
Figure 8.4. Osteoclast number is unchanged in juvenile *Dnmt3a* mutants. A) Representative TRAP images from the femur mid-diaphysis of wild-type (WT) and mutant ($Dnmt3a^{P900L/+}$ or $Dnmt3a^{R878H/+}$) mice. (B-C) Graphical

representation of B) osteoclast number per bone surface (Oc.N/BS) and C) osteoclast surface per bone surface (Oc.S/BS). ANOVA terms are displayed above the graphs, bolded terms have p < 0.05.
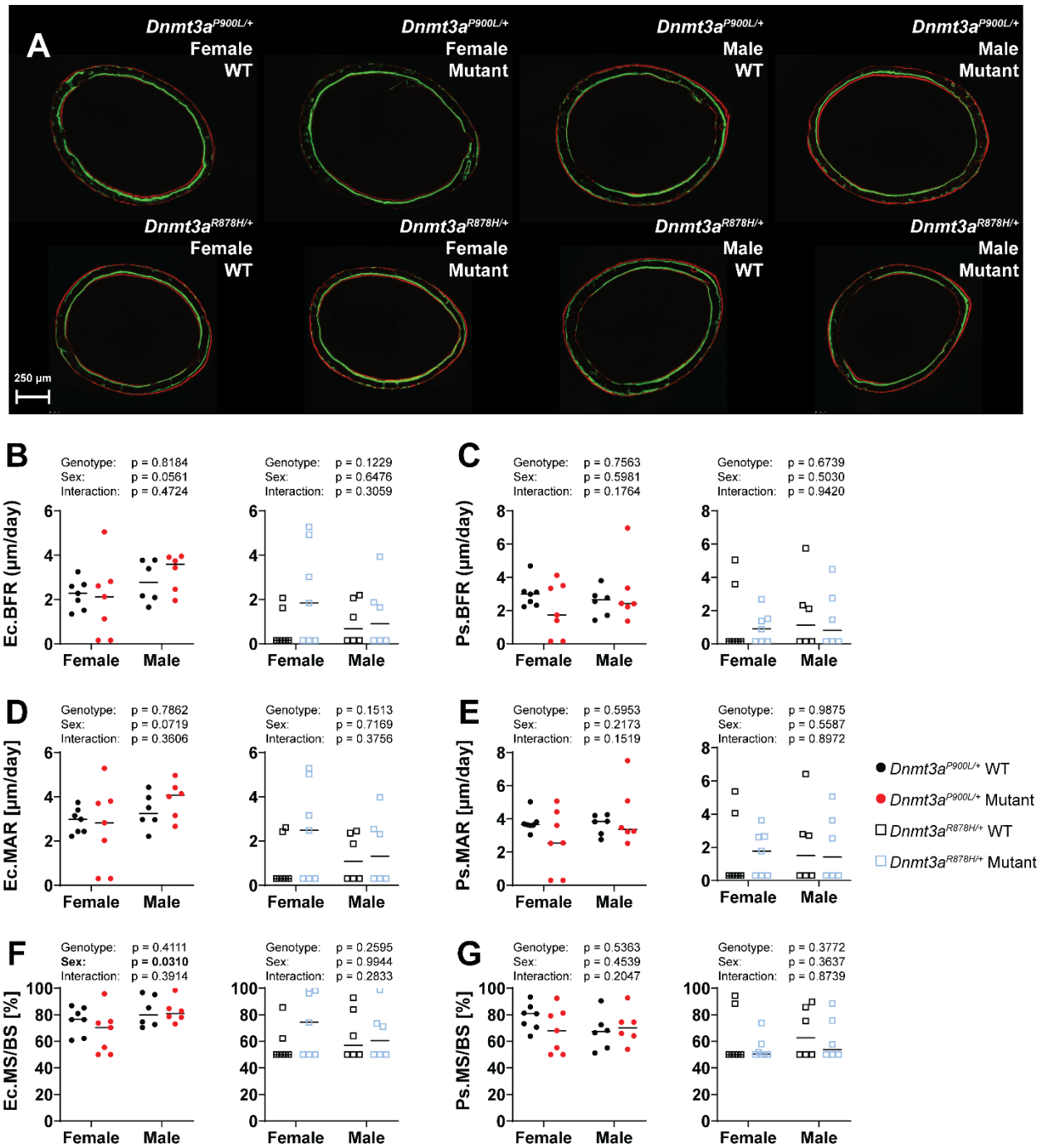
Figure 8.5. Osteoblast activity is unchanged in juvenile _Dnmt3a_ mutant mice. A) Representative dynamic histomorphometry images from the femur mid-diaphysis of wild-type (WT) and mutant (_Dnmt3a$^{P900L/+}$_ or _Dnmt3a$^{R878H/+}$_) mice. (B-G) Graphical representation of B) endocortical bone formation rate (Ec.BFR) and C) periosteal bone formation rate (Ps.BFR), D) endocortical mineral apposition rate (Ec.MAR) and E) periosteal mineral apposition rate (Ps.MAR), and F) endocortical mineralizing surface per bone surface (Ec.MS/BS) and G) periosteal mineralizing surface per bone surface (Ps.MS/BS). Samples with no double labeled surfaces were set to BFR = 0.15 µm/day, MAR = 0.30 µm/day, and MS/BS = 50%. _n_ = 5-7/mutation/sex/strain. ANOVA terms are displayed above the graphs, bolded terms have p < 0.05.

8.4.4 Trabecular bone unaffected but bone marrow adipose tissue increased in mature mice with *Dnmt3a* mutations

To determine if changes in skeletal development were isolated to overgrowth and cortical bone properties, we also examined trabecular bone properties in the distal femur metaphysis. In stark contrast to the cortical bone indices, no significant differences in femoral trabecular bone properties were observed between WT and mutant mice (Fig. 8.6). However, when assessing hematoxylin and eosin (H&E) staining in trabecular bone in the proximal tibia metaphysis, a clear difference was identified in bone marrow adipose tissue (BMAT) with an apparent increase in female *Dnmt3a^{R878H/+}* mutant mice (Fig. 8.7A). Quantification of bone marrow adipocyte cross-sectional area indicated a significant genotype effect by the *Dnmt3a^{R878H/+}* mutation but not the *Dnmt3a^{P900L/+}* mutation (Fig. 8.7B). Rather than quantifying the total BMAT area in the H&E-stained slides, three-dimensional BMAT volume was assessed using osmium tetroxide staining followed by µCT scanning. This approach allowed for quantification of BMAT volume across the entire marrow space. Osmium tetroxide staining showed that a group (2 out of 9; 22%) of *Dnmt3a^{R878H/+}* mutant female mice displayed a robust (>1 mm^3) increase in BMAT volume in the proximal tibia metaphysis. However, this increase was not present in all *Dnmt3a^{R878H/+}* mutant females and was not found in the males (Fig. 8.7C, D). There was a trend towards an increase in BMAT volume in the *Dnmt3a^{P900L/+}* mutants, but the effect size was more modest than the upregulation seen in the *Dnmt3a^{R878H/+}* mutants. In summary, bone marrow adipocyte cross-sectional area and bone marrow adipose tissue volume were increased in the proximal tibia metaphysis in female *Dnmt3a^{R878H/+}* mutants, but not in *Dnmt3a^{P900L/+}* mutants.
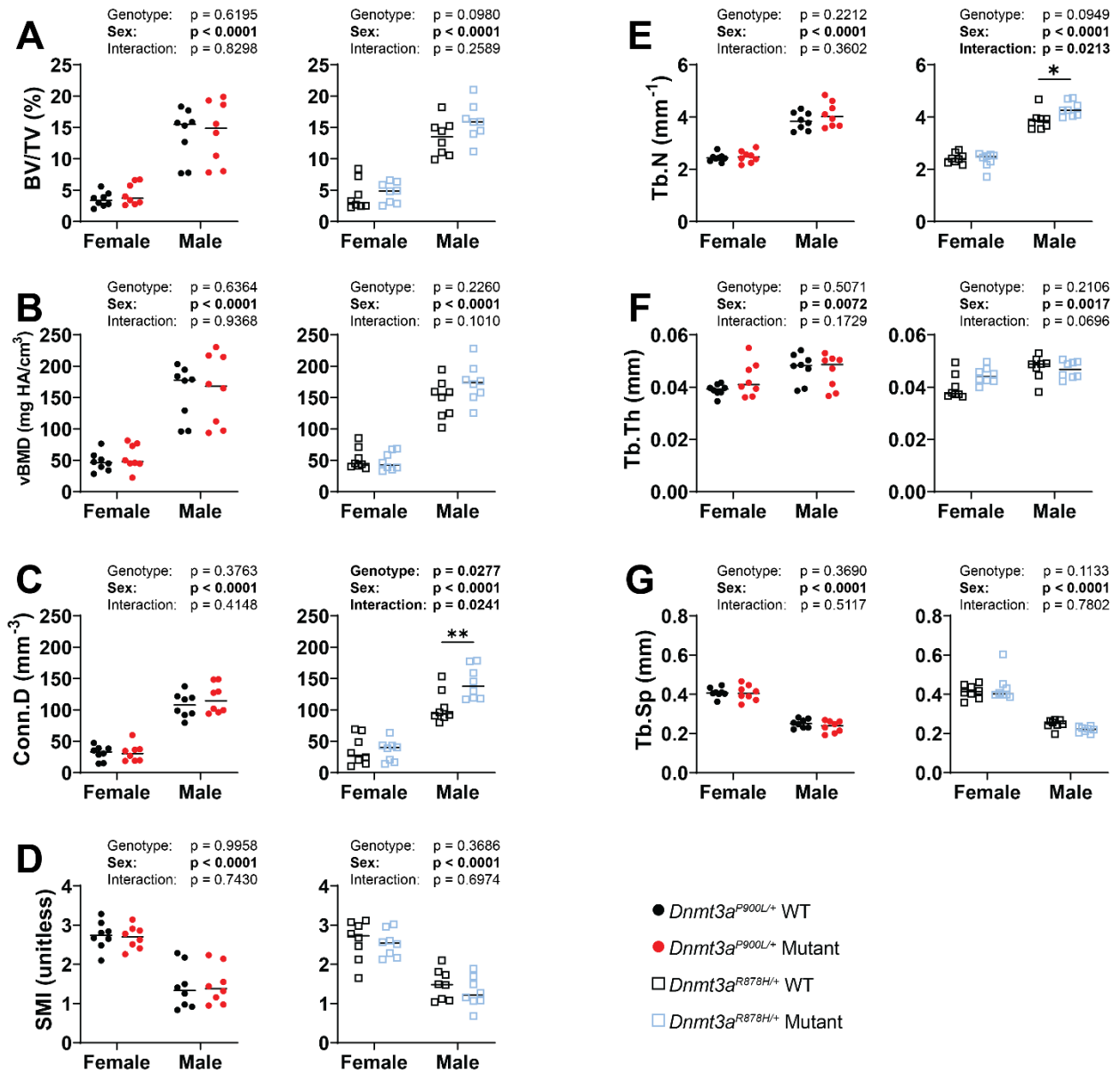
Figure 8.6. Trabecular bone properties are unchanged in mature mice with *Dnmt3a* mutations. (A-G) Graphical representation of trabecular bone properties for 30–36-week-old wild-type (WT) and mutant (*Dnmt3a*$^{P900L/+}$ or *Dnmt3a*$^{R878H/+}$) mice. A) Bone volume per tissue volume (BV/TV). B) Volumetric bone mineral density (vBMD). C) Connectivity density (Conn.D). D) Structure model index (SMI). E) Trabecular number (Tb.N). F) Trabecular thickness (Tb.Th). G) Trabecular spacing (Tb.Sp). Symbols indicate significance in post hoc testing: * p < 0.05, ** p < 0.01. *n* = 8/mutation/sex/strain. ANOVA terms are displayed above the graphs, bolded terms have p < 0.05.
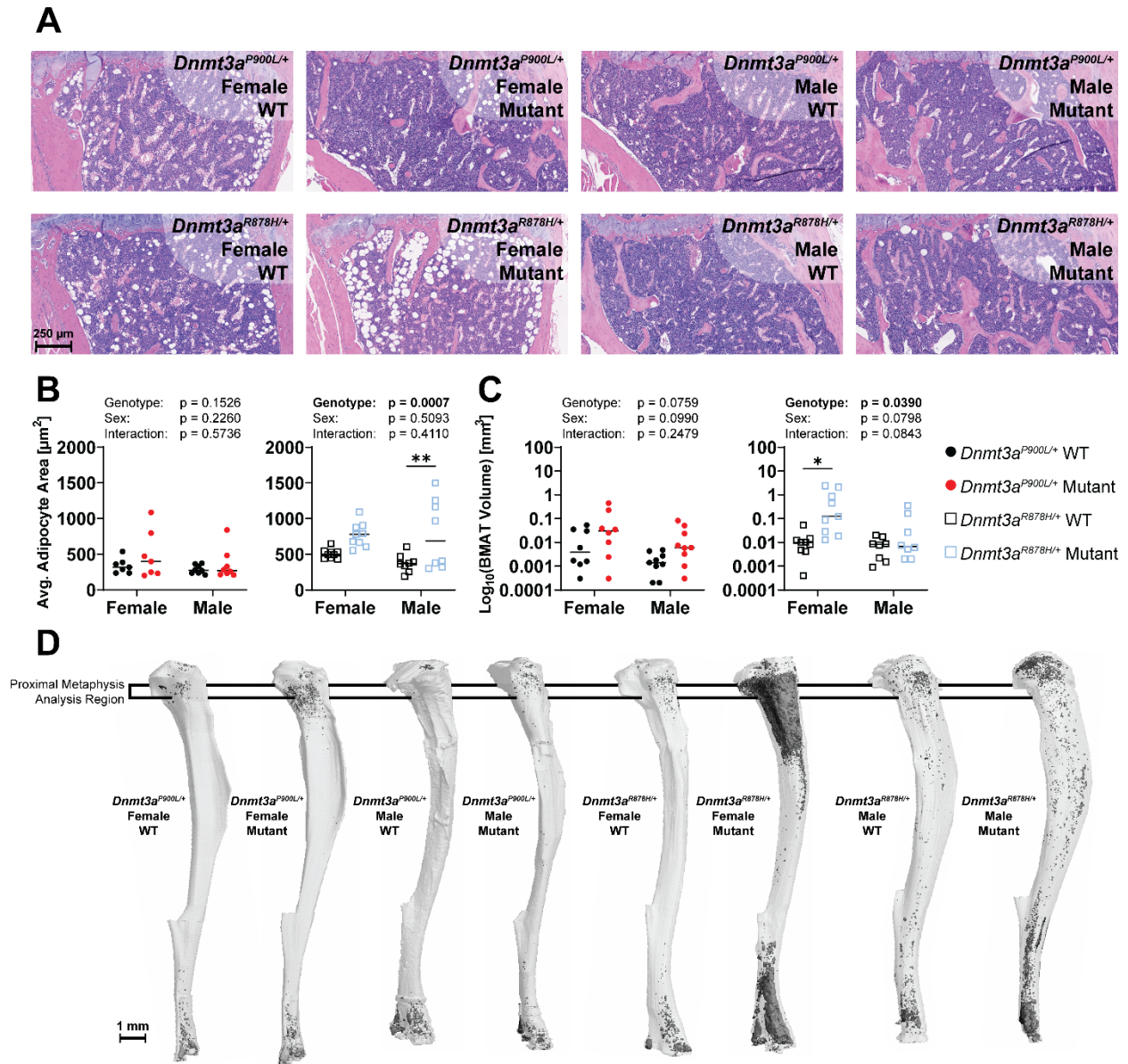
Figure 8.7. Bone marrow adipose tissue is increased in mice with _Dnmt3a$^{R878H/+}$_ mutation. A) Representative H&E images of the proximal tibial metaphyses from littermate pairs of male and female mice from wild-type (WT) and mutant (_Dnmt3a$^{P900L/+}$_ or _Dnmt3a$^{R878H/+}$_) genotypes. B) Average cross-sectional area of bone marrow adipocytes in H&E images. C) Osmium quantification in the proximal metaphyses of tibias from mature mice using a logarithmic scale (base 10). D) Representative 3D reconstructions from μCT scans of osmium-stained tibias from WT and mutant mice. Symbols indicate significance in post hoc testing:* $p < 0.05$, ** $p < 0.01$. n = 7-9/mutation/sex/strain. ANOVA terms are displayed above the graphs, bolded terms have $p < 0.05$.

8.5 Discussion

Managing functional skeletal abnormalities in TBRS patients, such as overgrowth, joint

hypermobility, and kyphoscoliosis, has been a focus for clinical standards of care. However, the

132

cellular and molecular underpinnings for the dysfunctional skeletal development observed in TBRS patients is poorly understood. Here, we report that the most robust phenotype in two different genetic mouse models of TBRS was cortical bone thinning. This phenotype has not previously been reported in TBRS patients and has important implications, including possible reduced bone strength. Importantly, μCT analysis also shows that tissue mineral density is unchanged in mouse models of TBRS indicating that hydroxyapatite is being deposited similarly in WT and mutant animals. However, three-point bend testing showed reduced strength, yield load, and maximum load for femurs in mice with either the $Dnmt3a^{P900L/+}$ or the $Dnmt3a^{R878H/+}$ mutation. Reduced bone strength is commonly associated with increased fracture risk which has not been widely reported in TBRS patients or the broader OGID patient community. It would be worthwhile to assess cortical bone thickness and strength in these patient populations to inform clinical decision-making and improve patient quality of life.

We investigated bone formation and osteoclast number in juvenile mutant mice at 27 days of age to determine what cells may be responsible for creating thinner cortical bone. Mice with osteoclast specific $Dnmt3a$ knockout experience impaired osteoclastogenesis and exhibit a dramatic increase in trabecular bone volume per tissue volume[18], a phenotype that was not seen in this study. This suggests that the heterozygous mutations in $Dnmt3a^{R878H/+}$ and $Dnmt3a^{P900L/+}$ mice have a qualitatively different impact on osteoclast biology than complete knockout. *In vitro* studies in human cells found that $DNMT3A$ upregulation increased methylation on promotors for *RUNX2*, *OSX*, and *IRF8*, promoting osteoclast differentiation and inhibiting osteoblast differentiation[19], suggesting that partial loss of $Dnmt3a$ may increase cortical thickness. Given that our results conflict with these previous studies on $Dnmt3a$ knockout mice and $Dnmt3a$ overexpression *in vitro*, we believe that studying heterozygous mutations of $Dnmt3a$ that

precisely mimic the molecular etiology of TBRS is essential for understanding the potential impact on cortical thickness and bone length in OGID syndromes.

Since tissue mineral density of the bone was unchanged in the $Dnmt3a^{R878H/+}$ and $Dnmt3a^{P900L/+}$, we hypothesized that osteoclasts may be responsible for the changes in cortical thickness. Dynamic histomorphometry showed no significant differences in bone formation rate between the WT and mutant groups for either sex, suggesting that osteoblast activity may not be impacted. However, quantification of TRAP staining showed that there were also no apparent changes in osteoclast number or osteoclast surface area in mice with either the $Dnmt3a^{P900L/+}$ or the $Dnmt3a^{R878H/+}$ mutation. Future studies involving *in vitro* osteoblast and osteoclast functional assays in cells with these $Dnmt3a$ mutations may be informative. Given the crosstalk and regulatory feedback that occurs *in vivo* between skeletal cells (osteoblasts, osteocytes, osteoclasts, marrow resident skeletal progenitor cells), it may be difficult to decipher cellular mechanisms *in vitro* via analyses of one cell type in isolation. In addition, Cre-inducible $Dnmt3a^{fl-R878H}$ mice (JAX Stock No. 032289) may serve as a key tool for delineating the effects of $Dnmt3a$ mutations on the development of osteoblasts (Osterix-Cre), osteoclasts (Cathepsin K-Cre), and growth plate chondrocytes (Aggrecan-Cre). Bulk and single-cell transcriptomics and methylomics of bone and bone marrow cells will also be critical for identifying the gene networks and molecular mechanisms disrupted in skeletal tissues of $Dnmt3a$ mutants. Although no differences in tissue mineral density were observed, cortical bone thinning in the $Dnmt3a$ mutant animals is a reasonable explanation for the reduction in bone mechanical properties identified in this study (i.e. stiffness, maximum load, and load-to-fracture). However, we cannot rule out the possibility that the material composition of bones in the mutant animals may also be altered and contribute to the mechanical property defects[20,21]. Common approaches

for characterizing bone quality include Raman spectroscopy to measure mineral-to-matrix ratios and mineral maturity/crystallinity[22], nanoindentation to detect changes at the microscale level[23], and quantitative backscattered scanning electron imaging (qBEI) to assess calcium concentration and distribution[24]. Changes in the bone collagen extracellular matrix (collagen fiber size, alignment, cross-linking) may also contribute to altered mechanical properties[25-27]. These are all avenues for future studies to thoroughly characterize the bones of *Dnmt3a* mutant mice to further understand why the bones are mechanically compromised.

In the emerging field of musculoskeletal crosstalk, it has become clear that fat cells can communicate with bone and cartilage cells[28-30]. As such, we analyzed bone marrow adipose tissue (BMAT) as another potential mechanism regulating the observed skeletal phenotypes. We found an increase in bone marrow adipocyte size in the *Dnmt3a*$^{R878H/+}$ mutant mice that has not been associated with TBRS patients. Within bone marrow, *DNMT3A* has been studied extensively in the context of clonal hematopoiesis (CH) and acute myeloid leukemia (AML) where hematopoietic stem cells in bone marrow develop cancerous mutations. The *DNMT3A*$^{R882H/+}$ mutation found in TBRS patients is also the most prevalent mutation associated with AML[31,32], but spontaneous hematopoietic malignancies (including AML) have not been reported before 12 months of age in the *Dnmt3a*$^{R878H/+}$ mice used in this work[16]. This suggests that the changes in the bone observed here occur in advance of the impacts of AML. Studies suggest that hematopoietic bone marrow cells with the *DNMT3A*$^{R882H/+}$ mutation do not respond to inflammatory cytokines secreted by bone marrow adipocytes[33,34]. Bone marrow adiposity is another example of the *DNMT3A*$^{R882H/+}$ mutation causing a broader and more severe array of phenotypes compared to *DNMT3A*$^{P904L/+}$ and other mutations. This correlates with stronger methylation effects observed in peripheral blood cells from TBRS patients with the

135

$DNMT3A^{R882H/+}$ mutation[16]. Given that osteoclasts originate from hematopoietic progenitors, future studies of intercellular communication between hematopoietic progenitors and bone marrow adipocytes may help identify molecular mechanisms responsible for skeletal abnormalities typical of mice with the $Dnmt3a^{R878H/+}$ mutation.

The presence of overgrowth, cortical thinning, and compromised mechanical properties in both the $Dnmt3a^{P900L/+}$ and the $Dnmt3a^{R878H/+}$ mutant animals suggest a common mechanism. The more consistent phenotypes (long bone overgrowth and cortical bone thinning) may be set into motion in the mesoderm during early embryonic development. Meanwhile, the mutation-specific changes, such as bone marrow adipose tissue development and behavioral abnormalities[14,16], may compound during the later stages of gestation when the mutant $Dnmt3a$ enzyme is more abundant. A previous study indicated that $Wnt3a$-induced $DNMT3A$ expression methylates the $SOX9$ promotor in human limb bud mesenchymal cells, but $FGF2$ and $FGF8$ can block $DNMT3A$ methylation by activating ERK1/2 phosphorylation of $DNMT3A^{35}$. That study examined several mutations in $DNMT3A$ with modifications at the ERK1/2 docking site or phosphorylation site and found significant differences in $SOX9$ methylation in the presence of those mutants. Future work should investigate what binding sites are modified by the $Dnmt3a^{R878H/+}$ and $Dnmt3a^{P900L/+}$ mutations to identify what molecular mechanisms may be impacted. Future developmental studies will provide critical information for understanding the origins of skeletal abnormalities and neurodevelopmental disorders present in TBRS patients. While we have identified new skeletal phenotypes in specific $Dnmt3a$ OGID mouse models, questions about cellular and molecular mechanism remain unanswered. In our studies, we chose an early postnatal timepoint (P27) to study osteoblast activity and osteoclast number. Osteoblast activity and osteoclast size and number are unchanged at P27, leaving the cellular mechanism for

cortical thinning unresolved. Future studies involving DNA methylation profiling and RNA-Seq

transcriptomic analyses will be useful for determining the cells and molecular pathways that are

impacted by mutations in *Dnmt3a*. Moreover, studies of Cre-inducible *Dnmt3a$^{fl-R878H}$* mice (JAX

Stock No. 032289) can be useful for differentiating developmental effects of the mutation from

disruptions in homeostasis[36]. Additional studies investigating the *in vivo* differentiation timeline

of mesenchymal and neural crest cells may provide critical insights into identifying a common

mechanism for the skeletal and neurodevelopmental abnormalities present in OGID patients.

An additional shortcoming of the present study is the lack of direct comparison between mutant

groups. Breeding animals to generate wild-type, *Dnmt3a$^{P900L/+}$*, and *Dnmt3a$^{R878H/+}$* mice in the

same litter will allow direct comparisons between strains and can improve our understanding of

the similarities and differences between the two mutations. While previous studies have

characterized the effects of the *Dnmt3a$^{R878H/+}$* and *Dnmt3a$^{P900L/+}$* mutations on the methylome

and transcriptome, those studies have been carried out in peripheral blood cells and neurons

which are distinct from the cells involved in skeletal development. Future studies can address the

shortcomings mentioned herein and further elucidate the mechanisms responsible for causing

overgrowth in TBRS and other OGID-class disorders.

8.6 References

1   Bell-Hensley, A. *et al.* Skeletal abnormalities in mice with Dnmt3a missense mutations.
        Bone **183**, 117085 (2024). https://doi.org/10.1016/j.bone.2024.117085

2   Tatton-Brown, K. *et al.* The Tatton-Brown-Rahman Syndrome: A clinical study of 55
        individuals with. *Wellcome Open Res* **3**, 46 (2018).
        https://doi.org/10.12688/wellcomeopenres.14430.1

3   Nakashima, K. & de Crombrugghe, B. Transcriptional mechanisms in osteoblast
        differentiation and bone formation. *Trends Genet* **19**, 458-466 (2003).
        https://doi.org/10.1016/S0168-9525(03)00176-8

4   Okano, M., Bell, D. W., Haber, D. A. & Li, E. DNA methyltransferases Dnmt3a and Dnmt3b are essential for de novo methylation and mammalian development. *Cell* **99**, 247-257 (1999). https://doi.org/10.1016/s0092-8674(00)81656-6

5   Gao, Q. *et al.* Bone Marrow Mesenchymal Stromal Cells: Identification, Classification, and Differentiation. *Front Cell Dev Biol* **9**, 787118 (2021). https://doi.org/10.3389/fcell.2021.787118

6   Sasai, Y. & De Robertis, E. M. Ectodermal patterning in vertebrate embryos. *Dev Biol* **182**, 5-20 (1997). https://doi.org/10.1006/dbio.1996.8445

7   Bouxsein, M. L. *et al.* Guidelines for assessment of bone microstructure in rodents using micro-computed tomography. *J Bone Miner Res* **25**, 1468-1486 (2010). https://doi.org/10.1002/jbmr.141

8   Jepsen, K. J., Silva, M. J., Vashishth, D., Guo, X. E. & van der Meulen, M. C. Establishing biomechanical mechanisms in mouse models: practical guidelines for systematically evaluating phenotypic changes in the diaphyses of long bones. *J Bone Miner Res* **30**, 951-966 (2015). https://doi.org/10.1002/jbmr.2539

9   Scheller, E. L. *et al.* Use of osmium tetroxide staining with microcomputerized tomography to visualize and quantify bone marrow adipose tissue in vivo. *Methods Enzymol* **537**, 123-139 (2014). https://doi.org/10.1016/B978-0-12-411619-1.00007-0

10   Scheller, E. L. *et al.* Region-specific variation in the properties of skeletal adipocytes reveals regulated and constitutive marrow adipose tissues. *Nat Commun* **6**, 7808 (2015). https://doi.org/10.1038/ncomms8808

11   Dempster, D. W. *et al.* Standardized nomenclature, symbols, and units for bone histomorphometry: a 2012 update of the report of the ASBMR Histomorphometry Nomenclature Committee. *J Bone Miner Res* **28**, 2-17 (2013). https://doi.org/10.1002/jbmr.1805

12   Lawson, L. Y. *et al.* Osteoblast-Specific Wnt Secretion Is Required for Skeletal Homeostasis and Loading-Induced Bone Formation in Adult Mice. *J Bone Miner Res* **37**, 108-120 (2022). https://doi.org/10.1002/jbmr.4445

13   Erben, R. G. Embedding of bone samples in methylmethacrylate: an improved method suitable for bone histomorphometry, histochemistry, and immunohistochemistry. *J Histochem Cytochem* **45**, 307-313 (1997). https://doi.org/10.1177/002215549704500215

14   Beard, D. C. *et al.* Distinct disease mutations in DNMT3A result in a spectrum of behavioral, epigenetic, and transcriptional deficits. *Cell Rep* **42**, 113411 (2023). https://doi.org/10.1016/j.celrep.2023.113411

15   Glatt, V., Canalis, E., Stadmeyer, L. & Bouxsein, M. L. Age-related changes in trabecular architecture differ in female and male C57BL/6J mice. *J Bone Miner Res* **22**, 1197-1207 (2007). https://doi.org/10.1359/jbmr.070507

16   Smith, A. M. *et al.* Functional and epigenetic phenotypes of humans and mice with DNMT3A Overgrowth Syndrome. *Nat Commun* **12**, 4549 (2021). https://doi.org/10.1038/s41467-021-24800-7

17   Foldes, J., Shih, M. S. & Parfitt, A. M. Frequency distributions of tetracycline-based measurements: implications for the interpretation of bone formation indices in the absence of double-labeled surfaces. *J Bone Miner Res* **5**, 1063-1067 (1990). https://doi.org/10.1002/jbmr.5650051010

18   Nishikawa, K. *et al.* DNA methyltransferase 3a regulates osteoclast differentiation by coupling to an S-adenosylmethionine-producing metabolic pathway. *Nat Med* **21**, 281-287 (2015). https://doi.org/10.1038/nm.3774

19   Liu, H. *et al.* Thymidine phosphorylase exerts complex effects on bone resorption and formation in myeloma. *Sci Transl Med* **8**, 353ra113 (2016). https://doi.org/10.1126/scitranslmed.aad8949

20   Tice, M. J. L., Bailey, S., Sroga, G. E., Gallagher, E. J. & Vashishth, D. Non-Obese MKR Mouse Model of Type 2 Diabetes Reveals Skeletal Alterations in Mineralization and Material Properties. *JBMR Plus* **6**, e10583 (2022). https://doi.org/10.1002/jbm4.10583

21   Kawashima, Y. *et al.* Type 2 diabetic mice demonstrate slender long bones with increased fragility secondary to increased osteoclastogenesis. *Bone* **44**, 648-655 (2009). https://doi.org/10.1016/j.bone.2008.12.012

22   Morris, M. D. & Mandair, G. S. Raman assessment of bone quality. *Clin Orthop Relat Res* **469**, 2160-2169 (2011). https://doi.org/10.1007/s11999-010-1692-y

23   Lewis, G. & Nyman, J. S. The use of nanoindentation for characterizing the properties of mineralized hard tissues: state-of-the art review. *J Biomed Mater Res B Appl Biomater* **87**, 286-301 (2008). https://doi.org/10.1002/jbm.b.31092

24	Mabilleau, G., Perrot, R., Flatt, P. R., Irwin, N. & Chappard, D. High fat-fed diabetic mice present with profound alterations of the osteocyte network. *Bone* **90**, 99-106 (2016). https://doi.org/10.1016/j.bone.2016.06.008

25	Ma, C., Du, T., Niu, X. & Fan, Y. Biomechanics and mechanobiology of the bone matrix. *Bone Res* **10**, 59 (2022). https://doi.org/10.1038/s41413-022-00223-y

26	Silva, M. J. *et al.* Decreased collagen organization and content are associated with reduced strength of demineralized and intact bone in the SAMP6 mouse. *J Bone Miner Res* **21**, 78-88 (2006). https://doi.org/10.1359/JBMR.050909

27	Tang, S. Y., Herber, R. P., Ho, S. P. & Alliston, T. Matrix metalloproteinase-13 is required for osteocytic perilacunar remodeling and maintains bone fracture resistance. *J Bone Miner Res* **27**, 1936-1950 (2012). https://doi.org/10.1002/jbmr.1646

28	Collins, K. H. *et al.* Adipose tissue is a critical regulator of osteoarthritis. *Proc Natl Acad Sci U S A* **118** (2021). https://doi.org/10.1073/pnas.2021096118

29	Hawkes, C. P. & Mostoufi-Moab, S. Fat-bone interaction within the bone marrow milieu: Impact on hematopoiesis and systemic energy metabolism. *Bone* **119**, 57-64 (2019). https://doi.org/10.1016/j.bone.2018.03.012

30	Scheller, E. L. & Rosen, C. J. What's the matter with MAT? Marrow adipose tissue, metabolism, and skeletal health. *Ann N Y Acad Sci* **1311**, 14-30 (2014). https://doi.org/10.1111/nyas.12327

31	Ley, T. J. *et al.* DNMT3A mutations in acute myeloid leukemia. *N Engl J Med* **363**, 2424-2433 (2010). https://doi.org/10.1056/NEJMoa1005143

32	Jaiswal, S. *et al.* Age-related clonal hematopoiesis associated with adverse outcomes. *N Engl J Med* **371**, 2488-2498 (2014). https://doi.org/10.1056/NEJMoa1408617

33	Liao, M. *et al.* Aging-elevated inflammation promotes DNMT3A R878H-driven clonal hematopoiesis. *Acta Pharm Sin B* **12**, 678-691 (2022). https://doi.org/10.1016/j.apsb.2021.09.015

34	Zioni, N. *et al.* Inflammatory signals from fatty bone marrow support DNMT3A driven clonal hematopoiesis. *Nat Commun* **14**, 2070 (2023). https://doi.org/10.1038/s41467-023-36906-1

35   Kumar, D. & Lassar, A. B. Fibroblast growth factor maintains chondrogenic potential of limb bud mesenchymal cells by modulating DNMT3A recruitment. *Cell Rep* **8**, 1419-1431 (2014). https://doi.org/10.1016/j.celrep.2014.07.038

36   Loberg, M. A. *et al.* Sequentially inducible mouse models reveal that Npm1 mutation causes malignant transformation of Dnmt3a-mutant clonal hematopoiesis. *Leukemia* **33**, 1635-1649 (2019). https://doi.org/10.1038/s41375-018-0368-6

Chapter 9: Future Directions: Skeletal Dysregulation Caused by *Dnmt3a* Mutations

9.1 Conclusions and Future Directions

In conclusion, Dnmt3a plays a critical role in skeletal development, impacting growth plate thickness in juvenile mice and long bone length, cortical thickness, and bone marrow adipose tissue in mature mice. *Dnmt3a* point mutations $Dnmt3a^{R878H/+}$ and $Dnmt3a^{P900L/+}$, both of which are homologous to mutations found in human TBRS patients, dysregulate murine skeletal development in multiple ways, some of which are established phenotypes of TBRS patients. The findings reported in this project should be used as a groundwork for future studies in mouse models of TBRS and other OGID mouse models. Several of the reported findings have not yet been investigated in humans and assessment in the clinical population would be warranted. A better understanding of skeletal abnormalities in TBRS can potentially be useful in improving diagnosis, treatment, and quality of life for these patients.

The phenotypic overlap in patients with various OGID syndromes despite having distinct causal mutations suggests a convergence in causal molecular mechanism. While methylomic and transcriptomic analyses have been performed in peripheral blood cells form TBRS patients[1] and hepatocytes and neurons from TBRS rodent models[2,3], cells from the mesenchymal lineage have not yet been interrogated using multi-omic approaches. Other fields have completed multi-omic studies on hematopoietic bone marrow cells from $Dnmt3a^{R878H/+}$ mutant mice in the context of acute myeloid leukemia (AML)[4] – this mutation has been linked to both TBRS and AML[5,6]. It would be interesting to investigate the overlap between DEGs in neuronal, hematopoietic, and hepatocytic lineages to identify functions of *Dnmt3a* that are consistently dysregulated in

multiple systems. However, it will be necessary to perform multi-omic analysis on MSCs to understand the role of *Dnmt3a* in the development mesoderm-lineage tissues. Generation of additional OGID mouse models will be informative for delineating the common molecular mechanisms underlying the dysregulation of neurological and skeletal developmental processes. Others have generated mouse models of Sotos syndrome with mutations in *Nsd1*[7], Weaver syndrome with mutations in *Ezh2*[8], Malan syndrome with mutations in *Nfix*[9], and homocystinuria with mutations in *Cbs*[10], but there has been limited skeletal characterization on each of these mouse models. The techniques applied to the TBRS mouse models should be recapitulated on other OGID models to improve the spatiotemporal focus of future molecular investigations and therapeutic developments.

9.2 References

1   Smith, A. M. *et al.* Functional and epigenetic phenotypes of humans and mice with DNMT3A Overgrowth Syndrome. *Nat Commun* **12**, 4549 (2021). https://doi.org/10.1038/s41467-021-24800-7

2   Christian, D. L. *et al.* DNMT3A Haploinsufficiency Results in Behavioral Deficits and Global Epigenomic Dysregulation Shared across Neurodevelopmental Disorders. *Cell Rep* **33**, 108416 (2020).

3   Beard, D. C. *et al.* Distinct disease mutations in DNMT3A result in a spectrum of behavioral, epigenetic, and transcriptional deficits. *Cell Rep* **42**, 113411 (2023). https://doi.org/10.1016/j.celrep.2023.113411

4   Li, Y. *et al.* Rapid and accurate remethylation of DNA in D*nmt3a*- deficient hematopoietic cells with restoration of DNMT3A activity. *Sci Adv* **10**, eadk8598 (2024). https://doi.org/10.1126/sciadv.adk8598

5   Ley, T. J. *et al.* DNMT3A mutations in acute myeloid leukemia. *N Engl J Med* **363**, 2424-2433 (2010). https://doi.org/10.1056/NEJMoa1005143

6   Tatton-Brown, K. *et al.* Mutations in the DNA methyltransferase gene DNMT3A cause an overgrowth syndrome with intellectual disability. *Nat Genet* **46**, 385-388 (2014). https://doi.org/10.1038/ng.2917

7   Oishi, S. *et al.* Investigating cortical features of Sotos syndrome using mice heterozygous for Nsd1. *Genes Brain Behav* **19**, e12637 (2020). https://doi.org/10.1111/gbb.12637

8   Lui, J. C. *et al.* Ezh2 Mutations Found in the Weaver Overgrowth Syndrome Cause a Partial Loss of H3K27 Histone Methyltransferase Activity. *J Clin Endocrinol Metab* **103**, 1470-1478 (2018). https://doi.org/10.1210/jc.2017-01948

9   Kooblall, K. G. *et al.* A Mouse Model with a Frameshift Mutation in the Nuclear Factor I/X (*JBMR Plus* **7**, e10739 (2023). https://doi.org/10.1002/jbm4.10739

10   Maclean, K. N. *et al.* A novel transgenic mouse model of CBS-deficient homocystinuria does not incur hepatic steatosis or fibrosis and exhibits a hypercoagulative phenotype that is ameliorated by betaine treatment. *Mol Genet Metab* **101**, 153-162 (2010). https://doi.org/10.1016/j.ymgme.2010.06.010

Appendix A: Safranin-O staining of chondrogenic pellet micromasses with and without over-expression of miR-181a/b-1 cluster.

CPC cartilage progenitor cell, NT non-transduced, LV-NS transduced with a lentivirus containing a non-silencing sequence, LV-181 transduced with a lentivirus containing the sequence for pre-miR-181a/b-1. Scale bar: 1 mm.

[145]

Appendix B: Type II collagen immunostaining of chondrogenic pellet micromasses with and without over-expression of miR-181a/b-1 cluster.

CPC cartilage progenitor cell, NT non-transduced, LV-NS transduced with a lentivirus containing a non-silencing sequence, LV-181 transduced with a lentivirus containing the sequence for pre-miR-181a/b-1. Scale bar: 1 mm.

[146]

Appendix C: Type IIA collagen immunostaining of chondrogenic pellet micromasses with and without over-expression of miR-181a/b-1 cluster.
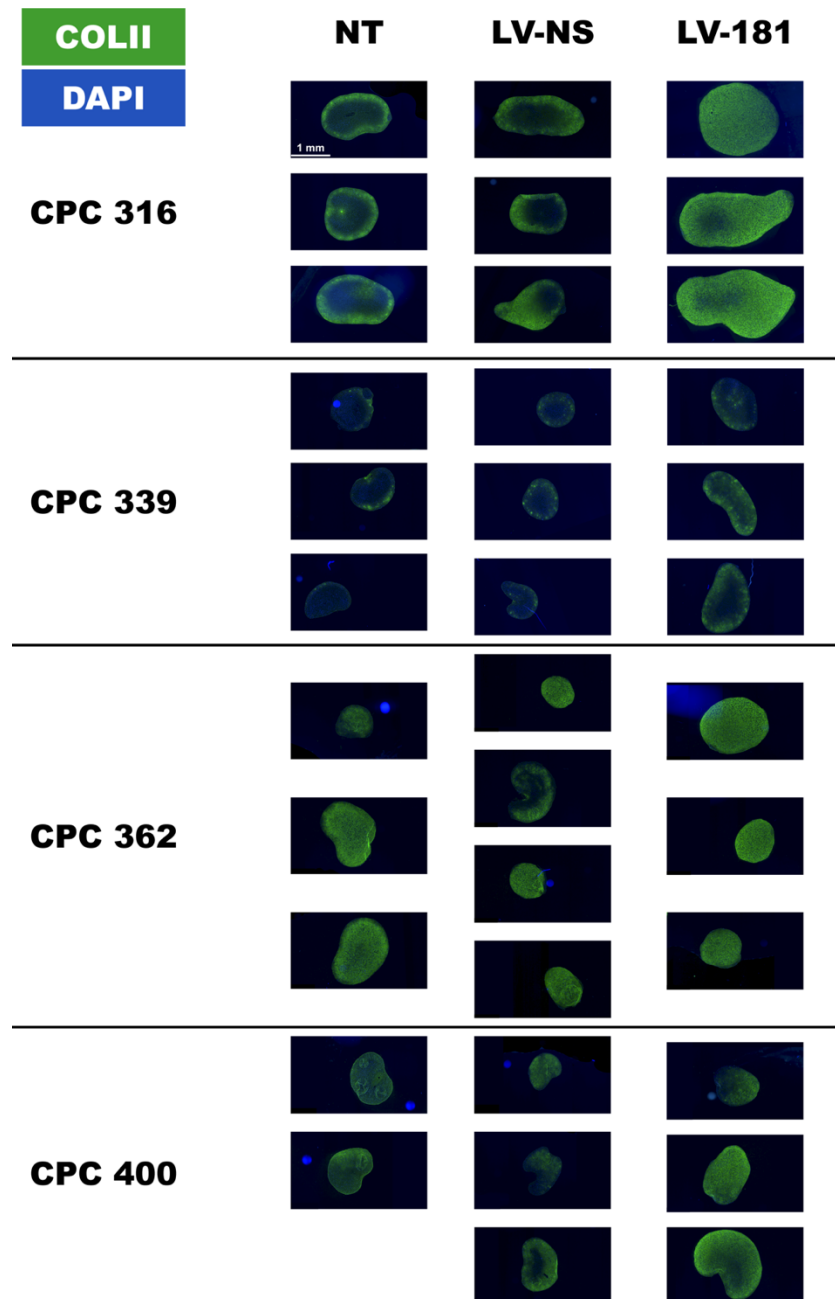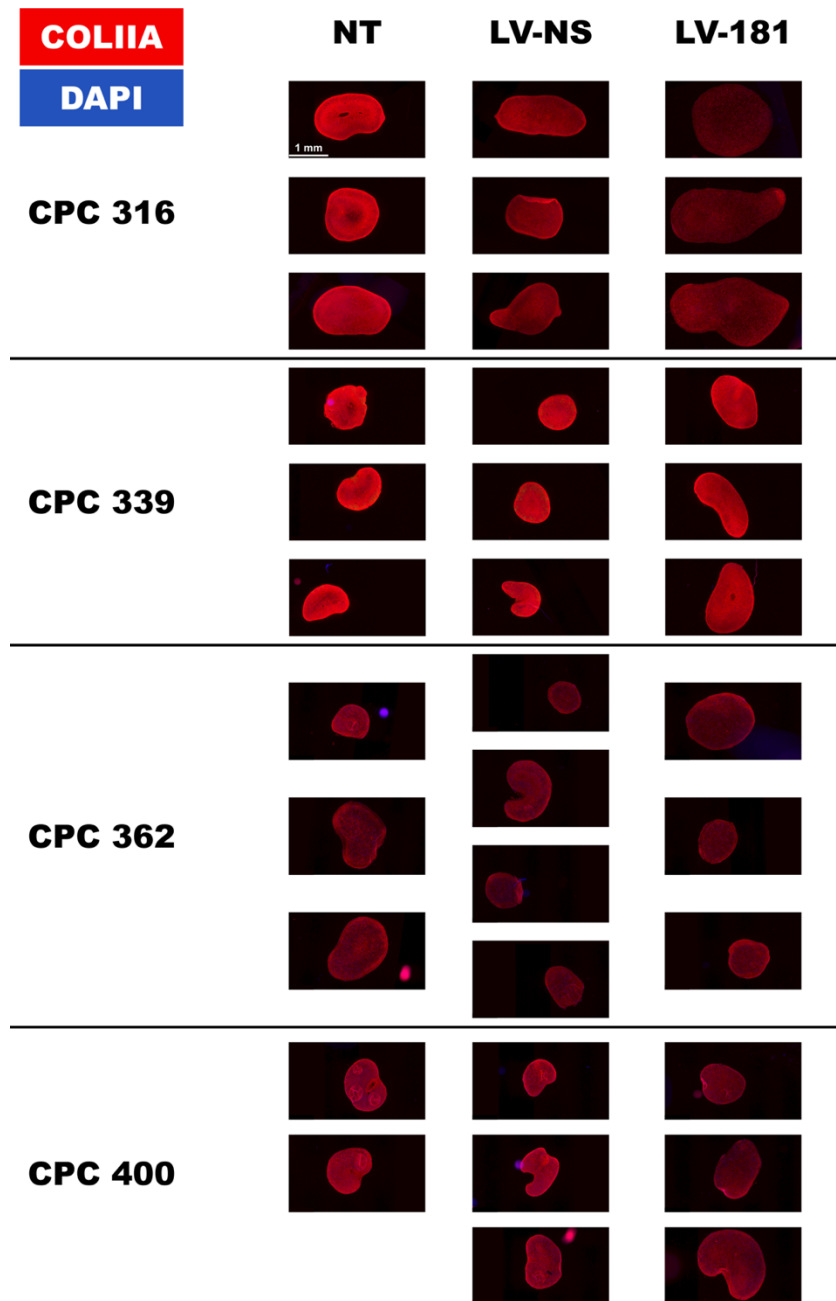
CPC cartilage progenitor cell, NT non-transduced, LV-NS transduced with a lentivirus containing a non-silencing sequence, LV-181 transduced with a lentivirus containing the sequence for pre-miR-181a/b-1. Scale bar: 1 mm.

Appendix D: Significantly upregulated genes in cartilage progenitor cell chondrogenesis following miR-181a/b-1 over-expression.

Gene	Description	Linear FC	Adj. P-Value
CCDC107	coiled-coil domain containing 107	24.53	1.84E-02
MATN4	matrilin 4	11.08	4.93E-03
COL2A1	collagen type II alpha 1 chain	11.06	1.63E-03
TMEM121	transmembrane protein 121	10.55	9.12E-03
COL9A3	collagen type IX alpha 3 chain	8.66	1.68E-03
PCBP1	poly(rC) binding protein 1	8.40	1.87E-02
SCAND1	SCAN domain containing 1	7.27	2.49E-02
CCDC85B	coiled-coil domain containing 85B	7.12	1.03E-02
H2AC16	H2A clustered histone 16	7.07	2.57E-02
BAD	BCL2 associated agonist of cell death	7.01	6.88E-03
COL9A2	collagen type IX alpha 2 chain	6.79	4.38E-03
CHADL	chondroadherin like	6.38	8.21E-03
SNORC	secondary ossification center associated regulator of chondrocyte maturation	6.19	1.27E-04
SCX	scleraxis bHLH transcription factor	6.16	1.88E-02
ANTKMT	adenine nucleotide translocase lysine methyltransferase	6.04	3.17E-02
CILP2	cartilage intermediate layer protein 2	5.63	1.96E-02
COL11A2	collagen type XI alpha 2 chain	5.41	1.69E-03
CKB	creatine kinase B	5.26	2.52E-03
PRR7	proline rich 7, synaptic	5.26	2.24E-02
ZNF205	zinc finger protein 205	5.24	2.12E-02
SSTR5	somatostatin receptor 5	5.04	2.41E-02
CDKN1C	cyclin dependent kinase inhibitor 1C	4.94	4.26E-03
CAPN6	calpain 6	4.84	1.99E-02
ZNF628	zinc finger protein 628	4.74	3.40E-02
HSPB6	heat shock protein family B (small) member 6	4.67	2.53E-02
RAB43	RAB43, member RAS oncogene family	4.54	4.97E-02
CNMD	chondromodulin	4.51	3.34E-02
ZNF837	zinc finger protein 837	4.42	5.92E-03
MAPK8IP2	mitogen-activated protein kinase 8 interacting protein 2	4.37	1.30E-02
PROK1	prokineticin 1	4.25	5.98E-03
RAMP1	receptor activity modifying protein 1	4.18	1.97E-02
CLEC3B	C-type lectin domain family 3 member B	4.17	2.28E-03
SOX8	SRY-box transcription factor 8	4.15	4.79E-02
CLIC3	chloride intracellular channel 3	4.00	1.06E-02
SCARF2	scavenger receptor class F member 2	3.95	8.77E-03

VASN	vasorin	3.69	2.14E-02
LRFN4	leucine rich repeat and fibronectin type III domain containing 4	3.65	1.34E-02
C1QTNF8	C1q and TNF related 8	3.63	1.88E-02
SIX5	SIX homeobox 5	3.61	2.68E-02
CLEC3A	C-type lectin domain family 3 member A	3.60	3.41E-02
CAPN15	calpain 15	3.59	1.37E-02
ALDOA	aldolase, fructose-bisphosphate A	3.55	1.81E-02
RNF208	ring finger protein 208	3.55	1.73E-02
JUND	JunD proto-oncogene, AP-1 transcription factor subunit	3.54	1.73E-02
C1QTNF3	C1q and TNF related 3	3.53	1.49E-02
FZD9	frizzled class receptor 9	3.37	2.92E-02
GDF15	growth differentiation factor 15	3.33	1.71E-02
CCDC124	coiled-coil domain containing 124	3.30	1.38E-02
ZNF469	zinc finger protein 469	3.30	5.66E-03
SELENOH	selenoprotein H	3.30	1.82E-02
RABAC1	Rab acceptor 1	3.30	6.88E-03
EMILIN1	elastin microfibril interfacer 1	3.29	6.92E-03
CHPF	chondroitin polymerizing factor	3.28	9.11E-03
MDFI	MyoD family inhibitor	3.26	1.63E-02
RAVER1	ribonucleoprotein, PTB binding 1	3.26	1.51E-02
FGFR3	fibroblast growth factor receptor 3	3.25	1.73E-02
TNNT3	troponin T3, fast skeletal type	3.25	1.46E-02
SLC39A4	solute carrier family 39 member 4	3.22	1.86E-02
H2AX	H2A.X variant histone	3.22	1.18E-02
TUBB2B	tubulin beta 2B class IIb	3.19	5.92E-03
MXD3	MAX dimerization protein 3	3.18	1.63E-02
PPP1R16A	protein phosphatase 1 regulatory subunit 16A	3.17	3.99E-03
C11orf96	chromosome 11 open reading frame 96	3.17	1.10E-02
C19orf71	chromosome 19 open reading frame 71	3.13	1.98E-02
PENK	proenkephalin	3.12	3.01E-03
FRZB	frizzled related protein	3.11	3.01E-02
PITX1	paired like homeodomain 1	3.10	4.22E-02
PKMYT1	protein kinase, membrane associated tyrosine/threonine 1	3.07	3.79E-02
EPYC	epiphycan	3.07	4.32E-02
PPDPF	pancreatic progenitor cell differentiation and proliferation factor	3.07	1.18E-02
CHTF18	chromosome transmission fidelity factor 18	3.03	2.38E-02
YDJC	YdjC chitooligosaccharide deacetylase homolog	3.01	4.76E-03
TAS1R1	taste 1 receptor member 1	3.01	2.17E-02
ZNF503	zinc finger protein 503	3.01	2.52E-03
SLC25A10	solute carrier family 25 member 10	2.99	9.15E-03
CDT1	chromatin licensing and DNA replication factor 1	2.97	1.05E-02
H2AC12	H2A clustered histone 12	2.96	1.30E-02
NDUFS7	NADH:ubiquinone oxidoreductase core subunit S7	2.94	3.55E-02

[149]

PWWP2B	PWWP domain containing 2B	2.90	2.09E-02
PANX2	pannexin 2	2.89	3.19E-02
IER5L	immediate early response 5 like	2.88	8.53E-03
GPC1	glypican 1	2.88	7.86E-03
PCSK4	proprotein convertase subtilisin/kexin type 4	2.87	1.90E-02
PPP1R35	protein phosphatase 1 regulatory subunit 35	2.84	4.50E-02
PKD1	polycystin 1, transient receptor potential channel interacting	2.83	3.19E-02
RASSF7	Ras association domain family member 7	2.82	9.37E-03
HHIP	hedgehog interacting protein	2.82	8.06E-03
SDK2	sidekick cell adhesion molecule 2	2.81	5.85E-03
CPLX1	complexin 1	2.79	2.23E-02
FGFRL1	fibroblast growth factor receptor like 1	2.78	1.32E-03
ICAM5	intercellular adhesion molecule 5	2.77	3.37E-02
CEBPD	CCAAT enhancer binding protein delta	2.77	1.34E-02
EFHD1	EF-hand domain family member D1	2.75	2.27E-02
NUDT22	nudix hydrolase 22	2.74	3.93E-02
NUBP2	nucleotide binding protein 2	2.69	4.51E-02
TMUB1	transmembrane and ubiquitin like domain containing 1	2.69	2.17E-02
LOXL2	lysyl oxidase like 2	2.68	4.26E-03
MIB2	mindbomb E3 ubiquitin protein ligase 2	2.65	2.98E-02
ZNHIT2	zinc finger HIT-type containing 2	2.64	4.97E-02
MMP28	matrix metallopeptidase 28	2.63	1.65E-02
FAM43B	family with sequence similarity 43 member B	2.63	6.58E-03
CPTP	ceramide-1-phosphate transfer protein	2.63	1.85E-02
JOSD2	Josephin domain containing 2	2.62	3.08E-02
RGCC	regulator of cell cycle	2.62	4.74E-03
FBXL15	F-box and leucine rich repeat protein 15	2.61	2.09E-02
CRIP2	cysteine rich protein 2	2.61	3.79E-02
HS3ST3A1	heparan sulfate-glucosamine 3-sulfotransferase 3A1	2.59	1.91E-02
H2BC7	H2B clustered histone 7	2.58	1.51E-02
CBARP	CACN subunit beta associated regulatory protein	2.58	4.79E-02
AHDC1	AT-hook DNA binding motif containing 1	2.57	1.35E-02
NYAP1	neuronal tyrosine phosphorylated phosphoinositide-3-kinase adaptor 1	2.55	2.25E-03
MACROD1	mono-ADP ribosylhydrolase 1	2.55	1.27E-02
TMC6	transmembrane channel like 6	2.55	3.18E-02
STBD1	starch binding domain 1	2.54	2.18E-02
GDF10	growth differentiation factor 10	2.53	3.73E-02
SMOC2	SPARC related modular calcium binding 2	2.53	4.74E-03
PLXNB3	plexin B3	2.52	2.77E-02
RRS1	ribosome biogenesis regulator 1 homolog	2.50	1.03E-02
FTH1	ferritin heavy chain 1	2.50	1.35E-02
WDR24	WD repeat domain 24	2.48	3.86E-02
ITIH6	inter-alpha-trypsin inhibitor heavy chain family member 6	2.48	2.17E-02

[150]

FBXL19	F-box and leucine rich repeat protein 19	2.46	1.81E-02
SLC7A5	solute carrier family 7 member 5	2.46	1.52E-03
FGFBP2	fibroblast growth factor binding protein 2	2.46	2.23E-03
VWA1	von Willebrand factor A domain containing 1	2.45	2.98E-02
SCRIB	scribble planar cell polarity protein	2.42	4.79E-02
TSC22D4	TSC22 domain family member 4	2.42	1.06E-02
LMO1	LIM domain only 1	2.41	3.18E-02
SHROOM2	shroom family member 2	2.41	1.63E-02
MAMDC4	MAM domain containing 4	2.41	4.29E-02
DSG3	desmoglein 3	2.40	4.74E-03
IGSF9	immunoglobulin superfamily member 9	2.39	2.03E-02
ZNF579	zinc finger protein 579	2.39	8.72E-03
METRNL	meteorin like, glial cell differentiation regulator	2.39	1.32E-02
C1orf159	chromosome 1 open reading frame 159	2.38	2.56E-02
CEP170B	centrosomal protein 170B	2.38	1.65E-02
CBX4	chromobox 4	2.37	7.58E-03
PTP4A3	protein tyrosine phosphatase 4A3	2.36	4.82E-02
GAS2L1	growth arrest specific 2 like 1	2.36	2.16E-02
H2AC11	H2A clustered histone 11	2.36	6.60E-03
PIM3	Pim-3 proto-oncogene, serine/threonine kinase	2.36	8.77E-03
APC2	APC regulator of WNT signaling pathway 2	2.35	2.24E-02
SAMD11	sterile alpha motif domain containing 11	2.35	3.48E-02
PRR12	proline rich 12	2.35	2.12E-02
DVL1	dishevelled segment polarity protein 1	2.33	4.37E-02
DOHH	deoxyhypusine hydroxylase	2.33	3.42E-02
CLEC11A	C-type lectin domain containing 11A	2.33	5.92E-03
NCLN	nicalin	2.32	9.35E-03
PDZD4	PDZ domain containing 4	2.32	2.60E-02
ZNF865	zinc finger protein 865	2.32	1.88E-02
TP53I13	tumor protein p53 inducible protein 13	2.31	2.20E-02
RGS19	regulator of G protein signaling 19	2.30	1.54E-02
TUBB2A	tubulin beta 2A class IIa	2.29	1.10E-02
FBLN2	fibulin 2	2.29	5.92E-03
GPSM1	G protein signaling modulator 1	2.29	3.36E-02
NUDT8	nudix hydrolase 8	2.28	4.77E-02
BCAR1	BCAR1 scaffold protein, Cas family member	2.28	2.85E-02
FBRSL1	fibrosin like 1	2.28	3.70E-02
ZNF598	zinc finger protein 598, E3 ubiquitin ligase	2.27	1.40E-02
EPN1	epsin 1	2.25	7.10E-03
METRN	meteorin, glial cell differentiation regulator	2.25	7.68E-03
SLC2A4RG	SLC2A4 regulator	2.24	2.65E-02
ISM1	isthmin 1	2.23	3.62E-02
B3GNT7	UDP-GlcNAc:betaGal beta-1,3-N-acetylglucosaminyltransferase 7	2.23	5.36E-03

CSPG4	chondroitin sulfate proteoglycan 4	2.22	2.28E-03
ZFPM1	zinc finger protein, FOG family member 1	2.22	2.93E-02
RAI1	retinoic acid induced 1	2.22	1.56E-02
PRRX2	paired related homeobox 2	2.21	4.35E-02
TSPO	translocator protein	2.21	3.37E-02
MAFK	MAF bZIP transcription factor K	2.21	2.10E-02
RAB24	RAB24, member RAS oncogene family	2.21	1.88E-02
MYORG	myogenesis regulating glycosidase (putative)	2.21	1.06E-02
ZNF385B	zinc finger protein 385B	2.20	1.32E-03
HIC1	HIC ZBTB transcriptional repressor 1	2.20	1.03E-02
COL1A1	collagen type I alpha 1 chain	2.20	2.98E-02
DEGS2	delta 4-desaturase, sphingolipid 2	2.20	2.12E-02
HRCT1	histidine rich carboxyl terminus 1	2.20	2.88E-02
FAM110A	family with sequence similarity 110 member A	2.20	9.67E-03
MYPOP	Myb related transcription factor, partner of profilin	2.19	4.30E-03
H2BC15	H2B clustered histone 15	2.19	1.00E-02
SLC25A22	solute carrier family 25 member 22	2.19	2.66E-02
JUNB	JunB proto-oncogene, AP-1 transcription factor subunit	2.18	3.88E-02
TLNRD1	talin rod domain containing 1	2.18	5.61E-03
AMOTL2	angiomotin like 2	2.18	6.46E-03
ZBTB45	zinc finger and BTB domain containing 45	2.17	2.48E-02
H2BC17	H2B clustered histone 17	2.17	3.57E-02
STUB1	STIP1 homology and U-box containing protein 1	2.16	8.06E-03
FLYWCH2	FLYWCH family member 2	2.16	3.65E-02
NKX3-2	NK3 homeobox 2	2.16	2.50E-02
GATD3B	glutamine amidotransferase like class 1 domain containing 3B	2.16	3.12E-02
SSBP4	single stranded DNA binding protein 4	2.15	2.60E-02
AJM1	apical junction component 1 homolog	2.15	4.97E-02
S100A1	S100 calcium binding protein A1	2.14	1.44E-02
PCDHB6	protocadherin beta 6	2.13	2.68E-02
CYBA	cytochrome b-245 alpha chain	2.12	7.53E-03
COL6A1	collagen type VI alpha 1 chain	2.12	1.65E-02
TTYH3	tweety family member 3	2.12	3.79E-02
CSNK1G2	casein kinase 1 gamma 2	2.12	2.53E-02
SLPI	secretory leukocyte peptidase inhibitor	2.11	7.86E-03
ZGPAT	zinc finger CCCH-type and G-patch domain containing	2.11	3.66E-02
GNG5	G protein subunit gamma 5	2.11	3.77E-02
TRABD	TraB domain containing	2.10	4.51E-02
CHAD	chondroadherin	2.10	4.90E-02
DOT1L	DOT1 like histone lysine methyltransferase	2.10	7.27E-03
MZT2A	mitotic spindle organizing protein 2A	2.10	3.43E-02
PKP3	plakophilin 3	2.10	3.31E-02
NPDC1	neural proliferation, differentiation and control 1	2.10	4.10E-02

[152]

MEGF8	multiple EGF like domains 8	2.10	2.23E-03
DOK1	docking protein 1	2.10	5.85E-03
CCN2	cellular communication network factor 2	2.09	1.49E-02
SAC3D1	SAC3 domain containing 1	2.09	3.44E-02
PLEC	plectin	2.09	2.11E-02
PLD4	phospholipase D family member 4	2.09	3.31E-02
PIEZO1	piezo type mechanosensitive ion channel component 1	2.08	8.77E-03
REEP4	receptor accessory protein 4	2.07	7.10E-03
ARMC5	armadillo repeat containing 5	2.07	2.44E-02
MRPL2	mitochondrial ribosomal protein L2	2.07	1.87E-02
TAFA5	TAFA chemokine like family member 5	2.07	4.80E-02
FASN	fatty acid synthase	2.07	4.06E-02
COL5A1	collagen type V alpha 1 chain	2.06	6.53E-03
MRPL57	mitochondrial ribosomal protein L57	2.06	1.83E-02
SPHK2	sphingosine kinase 2	2.06	2.18E-02
HSPB1	heat shock protein family B (small) member 1	2.06	2.63E-02
COPE	COPI coat complex subunit epsilon	2.06	1.37E-02
GPAA1	glycosylphosphatidylinositol anchor attachment 1	2.06	1.73E-02
MN1	MN1 proto-oncogene, transcriptional regulator	2.06	1.34E-02
GPRC5C	G protein-coupled receptor class C group 5 member C	2.05	3.83E-02
FSCN1	fascin actin-bundling protein 1	2.05	1.33E-02
GNA11	G protein subunit alpha 11	2.05	1.30E-02
GFER	growth factor, augmenter of liver regeneration	2.05	1.09E-02
DDIT4	DNA damage inducible transcript 4	2.04	2.80E-02
MTLN	mitoregulin	2.04	9.64E-03
FBXO46	F-box protein 46	2.03	2.35E-02
CARNS1	carnosine synthase 1	2.03	7.53E-03
CTSD	cathepsin D	2.03	8.37E-03
TPRN	taperin	2.03	3.43E-02
EPS8L2	EPS8 like 2	2.03	1.34E-02
TRMT61A	tRNA methyltransferase 61A	2.03	3.13E-02
NDOR1	NADPH dependent diflavin oxidoreductase 1	2.02	3.43E-02
P2RY6	pyrimidinergic receptor P2Y6	2.02	1.81E-02
TRPV4	transient receptor potential cation channel subfamily V member 4	2.01	3.05E-03
SLC44A2	solute carrier family 44 member 2	2.01	1.75E-02
FLRT1	fibronectin leucine rich transmembrane protein 1	2.01	4.78E-02
GABRE	gamma-aminobutyric acid type A receptor subunit epsilon	2.01	1.73E-02
SCAF1	SR-related CTD associated factor 1	2.01	2.16E-02
SPPL2B	signal peptide peptidase like 2B	2.01	3.09E-02
ITIH5	inter-alpha-trypsin inhibitor heavy chain 5	2.00	7.74E-03
SRPK3	SRSF protein kinase 3	2.00	2.45E-02
TONSL	tonsoku like, DNA repair protein	2.00	4.47E-02

Appendix E: Significantly downregulated genes in cartilage progenitor cell chondrogenesis following miR-181a/b-1 over-expression.

Gene	Description	Linear FC	Adj. P-Value
AQP9	aquaporin 9	-14.54	2.52E-03
SLC6A15	solute carrier family 6 member 15	-10.27	7.22E-03
OASL	2prime-5prime-oligoadenylate synthetase like	-7.84	1.76E-03
RSAD2	radical S-adenosyl methionine domain containing 2	-7.67	3.28E-03
APOL3	apolipoprotein L3	-6.93	2.43E-04
GBP4	guanylate binding protein 4	-5.96	8.69E-03
DOCK2	dedicator of cytokinesis 2	-4.98	1.09E-02
TNFSF10	TNF superfamily member 10	-4.63	6.58E-03
RTP4	receptor transporter protein 4	-4.51	7.86E-03
SAMD12	sterile alpha motif domain containing 12	-4.47	4.03E-02
BST2	bone marrow stromal cell antigen 2	-4.35	1.39E-03
HERC6	HECT and RLD domain containing E3 ubiquitin protein ligase family member 6	-4.25	5.85E-03
OAS1	2prime-5prime-oligoadenylate synthetase 1	-4.09	9.46E-03
S100A7A	S100 calcium binding protein A7A	-4.09	2.52E-03
IFIT2	interferon induced protein with tetratricopeptide repeats 2	-3.92	1.64E-02
NLGN4X	neuroligin 4 X-linked	-3.70	6.50E-03
KLKB1	kallikrein B1	-3.61	3.91E-02
DRAXIN	dorsal inhibitory axon guidance protein	-3.59	4.10E-02
MX2	MX dynamin like GTPase 2	-3.57	1.30E-02
PRXL2A	peroxiredoxin like 2A	-3.37	1.83E-02
SELENOP	selenoprotein P	-3.36	4.26E-03
CMPK2	cytidine/uridine monophosphate kinase 2	-3.32	2.19E-02
ABCA6	ATP binding cassette subfamily A member 6	-3.32	5.21E-03
HSD11B1	hydroxysteroid 11-beta dehydrogenase 1	-3.31	7.10E-03
DDO	D-aspartate oxidase	-3.28	1.85E-02
IFI27	interferon alpha inducible protein 27	-3.27	1.92E-02
ANKRD29	ankyrin repeat domain 29	-3.25	9.34E-03
IFIT3	interferon induced protein with tetratricopeptide repeats 3	-3.25	2.38E-02
IFI44L	interferon induced protein 44 like	-3.11	1.73E-02
DDX58	DExD/H-box helicase 58	-3.11	1.27E-02
S1PR1	sphingosine-1-phosphate receptor 1	-3.10	1.84E-02
BATF2	basic leucine zipper ATF-like transcription factor 2	-3.10	3.62E-02
ZNF597	zinc finger protein 597	-3.09	4.26E-03

CADM3	cell adhesion molecule 3	-3.04	2.42E-02
OAS2	2prime-5prime-oligoadenylate synthetase 2	-3.02	3.12E-02
IFIT1	interferon induced protein with tetratricopeptide repeats 1	-2.99	3.46E-02
HERC5	HECT and RLD domain containing E3 ubiquitin protein ligase 5	-2.91	1.54E-02
IFIH1	interferon induced with helicase C domain 1	-2.86	1.34E-02
ALDH1A2	aldehyde dehydrogenase 1 family member A2	-2.85	1.44E-02
EVI2A	ecotropic viral integration site 2A	-2.82	6.20E-03
SAA1	serum amyloid A1	-2.82	1.51E-02
IFI44	interferon induced protein 44	-2.80	1.29E-02
RGS4	regulator of G protein signaling 4	-2.77	1.47E-02
IFIT1B	interferon induced protein with tetratricopeptide repeats 1B	-2.77	3.67E-02
DDX60L	DExD/H-box 60 like	-2.75	1.33E-02
C3	complement C3	-2.71	1.92E-03
SAMD9	sterile alpha motif domain containing 9	-2.67	1.68E-02
VAV3	vav guanine nucleotide exchange factor 3	-2.62	2.30E-02
DDX60	DExD/H-box helicase 60	-2.59	1.99E-02
APOL1	apolipoprotein L1	-2.57	8.34E-03
IFITM1	interferon induced transmembrane protein 1	-2.57	2.42E-02
CBX7	chromobox 7	-2.57	1.39E-03
FSIP1	fibrous sheath interacting protein 1	-2.56	1.23E-02
OAS3	2prime-5prime-oligoadenylate synthetase 3	-2.55	4.98E-02
ZMAT1	zinc finger matrin-type 1	-2.52	1.10E-02
CHI3L1	chitinase 3 like 1	-2.52	4.38E-03
ZNF483	zinc finger protein 483	-2.52	1.63E-03
SP110	SP110 nuclear body protein	-2.50	1.10E-02
CLIC2	chloride intracellular channel 2	-2.50	2.41E-02
PARP12	poly(ADP-ribose) polymerase family member 12	-2.47	9.60E-03
HOPX	HOP homeobox	-2.47	4.26E-03
REPS2	RALBP1 associated Eps domain containing 2	-2.46	4.24E-02
KCNMB1	potassium calcium-activated channel subfamily M regulatory beta subunit 1	-2.44	3.96E-02
SLC22A4	solute carrier family 22 member 4	-2.44	2.23E-03
DTNA	dystrobrevin alpha	-2.38	2.42E-02
PHLDB2	pleckstrin homology like domain family B member 2	-2.38	3.28E-03
SOD2	superoxide dismutase 2	-2.36	3.01E-03
PCSK1	proprotein convertase subtilisin/kexin type 1	-2.36	1.16E-02
PSMB9	proteasome 20S subunit beta 9	-2.34	7.68E-03
GBP1	guanylate binding protein 1	-2.32	9.73E-03
MMP1	matrix metallopeptidase 1	-2.30	4.55E-02
TLR3	toll like receptor 3	-2.29	7.73E-03
TLR2	toll like receptor 2	-2.27	3.21E-02
PLAAT3	phospholipase A and acyltransferase 3	-2.25	5.92E-03
TGFBR3	transforming growth factor beta receptor 3	-2.25	8.63E-04
TMEM26	transmembrane protein 26	-2.24	1.95E-02

VIT	vitrin	-2.24	9.12E-03
ZNF33B	zinc finger protein 33B	-2.23	9.87E-03
HSPE1	heat shock protein family E (Hsp10) member 1	-2.22	1.27E-02
RAB37	RAB37, member RAS oncogene family	-2.21	2.56E-02
GBP2	guanylate binding protein 2	-2.20	1.56E-03
ZNF124	zinc finger protein 124	-2.19	2.52E-03
DPYD	dihydropyrimidine dehydrogenase	-2.18	1.68E-03
ZNF670	zinc finger protein 670	-2.18	1.56E-02
CFB	complement factor B	-2.17	8.37E-03
PARP14	poly(ADP-ribose) polymerase family member 14	-2.17	1.88E-02
PLAAT4	phospholipase A and acyltransferase 4	-2.15	3.13E-02
SYT7	synaptotagmin 7	-2.13	8.06E-03
LPAR6	lysophosphatidic acid receptor 6	-2.12	1.90E-02
LRRK2	leucine rich repeat kinase 2	-2.11	7.74E-03
DRAM1	DNA damage regulated autophagy modulator 1	-2.10	1.38E-03
DTX3L	deltex E3 ubiquitin ligase 3L	-2.10	3.49E-02
GSKIP	GSK3B interacting protein	-2.08	4.38E-03
GBP3	guanylate binding protein 3	-2.08	5.76E-03
MME	membrane metalloendopeptidase	-2.08	6.92E-03
VCAM1	vascular cell adhesion molecule 1	-2.07	6.58E-03
TOM1L1	target of myb1 like 1 membrane trafficking protein	-2.06	2.57E-02
KCNT2	potassium sodium-activated channel subfamily T member 2	-2.06	4.26E-03
UBA7	ubiquitin like modifier activating enzyme 7	-2.06	7.87E-03
XAF1	XIAP associated factor 1	-2.06	2.23E-02
FAT3	FAT atypical cadherin 3	-2.06	1.12E-02
HSD17B11	hydroxysteroid 17-beta dehydrogenase 11	-2.05	1.75E-02
FAM124A	family with sequence similarity 124 member A	-2.05	1.09E-02
C5orf46	chromosome 5 open reading frame 46	-2.04	3.00E-02
ERAP2	endoplasmic reticulum aminopeptidase 2	-2.03	3.03E-02
NLRC5	NLR family CARD domain containing 5	-2.03	7.59E-03
PTPN22	protein tyrosine phosphatase non-receptor type 22	-2.03	9.15E-03
ZNF844	zinc finger protein 844	-2.03	1.35E-02
ABCA8	ATP binding cassette subfamily A member 8	-2.02	4.44E-02
TPRG1	tumor protein p63 regulated 1	-2.02	1.97E-02
AMPH	amphiphysin	-2.01	1.44E-02
SLC19A3	solute carrier family 19 member 3	-2.01	1.44E-02
IFI16	interferon gamma inducible protein 16	-2.00	7.10E-03
SCG5	secretogranin V	-2.00	4.26E-03

[156]

Appendix F: Significantly perturbed Reactome pathways in cartilage progenitor cell chondrogenesis following miR-181a/b-1 over-expression.

Term ID	Term Description from Reactome	Mean Log FC vs Background	Adj. P-value
R-HSA-1474244	Extracellular matrix organization	5.51	5.04E-05
R-HSA-1474290	Collagen formation	5.35	1.67E-04
R-HSA-5334118	DNA methylation	5.25	2.17E-04
R-HSA-1650814	Collagen biosynthesis and modifying enzymes	5.23	2.17E-04
R-HSA-2022090	Assembly of collagen fibrils and other multimeric structures	4.85	6.92E-04
R-HSA-8948216	Collagen chain trimerization	4.84	8.05E-04
R-HSA-2299718	Condensation of Prophase Chromosomes	4.82	6.28E-04
R-HSA-2559582	Senescence-Associated Secretory Phenotype (SASP)	4.70	6.28E-04
R-HSA-5625886	Activated PKN1 stimulates transcription of AR regulated genes KLK2 and KLK3	4.61	7.91E-04
R-HSA-3214815	HDACs deacetylate histones	4.58	7.91E-04
R-HSA-9616222	Transcriptional regulation of granulopoiesis	4.58	7.91E-04
R-HSA-9610379	HCMV Late Events	4.56	7.91E-04
R-HSA-427389	ERCC6 (CSB) and EHMT2 (G9a) positively regulate rRNA expression	4.55	7.91E-04
R-HSA-201722	Formation of the beta-catenin:TCF transactivating complex	4.46	8.94E-04
R-HSA-427359	SIRT1 negatively regulates rRNA expression	4.41	1.23E-03
R-HSA-1912422	Pre-NOTCH Expression and Processing	4.34	1.17E-03
R-HSA-3214858	RMTs methylate histone arginines	4.20	2.05E-03
R-HSA-2559583	Cellular Senescence	4.20	1.54E-03
R-HSA-212300	PRC2 methylates histones and DNA	4.16	2.37E-03
R-HSA-9609646	HCMV Infection	4.14	2.04E-03
R-HSA-5625740	RHO GTPases activate PKNs	4.08	2.57E-03
R-HSA-2559586	DNA Damage/Telomere Stress Induced Senescence	4.06	2.81E-03
R-HSA-5617472	Activation of anterior HOX genes in hindbrain development during early embryogenesis	4.05	2.57E-03
R-HSA-3000171	Non-integrin membrane-ECM interactions	3.96	4.44E-03
R-HSA-8936459	RUNX1 regulates genes involved in megakaryocyte differentiation and platelet function	3.93	4.10E-03
R-HSA-110330	Recognition and association of DNA glycosylase with site containing an affected purine	3.92	4.84E-03
R-HSA-3000178	ECM proteoglycans	3.91	4.84E-03
R-HSA-1474228	Degradation of the extracellular matrix	3.89	4.44E-03
R-HSA-1442490	Collagen degradation	3.88	5.73E-03
R-HSA-9609690	HCMV Early Events	3.82	4.84E-03

R-HSA-5250924	B-WICH complex positively regulates rRNA expression	3.81	5.27E-03
R-HSA-1971475	A tetrasaccharide linker sequence is required for GAG synthesis	3.81	1.23E-02
R-HSA-73929	Base-Excision Repair, AP Site Formation	3.75	6.61E-03
R-HSA-1630316	Glycosaminoglycan metabolism	3.75	5.73E-03
R-HSA-5250913	Positive epigenetic regulation of rRNA expression	3.72	6.15E-03
R-HSA-3560782	Diseases associated with glycosaminoglycan metabolism	3.60	1.28E-02
R-HSA-2559580	Oxidative Stress Induced Senescence	3.51	1.20E-02
R-HSA-977225	Amyloid fiber formation	3.46	1.38E-02
R-HSA-5578749	Transcriptional regulation by small RNAs	3.45	1.38E-02
R-HSA-73884	Base Excision Repair	3.45	1.38E-02
R-HSA-606279	Deposition of new CENPA-containing nucleosomes at the centromere	3.44	1.49E-02
R-HSA-195258	RHO GTPase Effectors	3.44	1.31E-02
R-HSA-9670095	Inhibition of DNA recombination at telomere	3.42	1.54E-02
R-HSA-9645723	Diseases of programmed cell death	3.38	1.59E-02
R-HSA-1793185	Chondroitin sulfate/dermatan sulfate metabolism	3.36	1.99E-02
R-HSA-73772	RNA Polymerase I Promoter Escape	3.35	1.75E-02
R-HSA-73864	RNA Polymerase I Transcription	3.29	1.99E-02
R-HSA-68875	Mitotic Prophase	3.26	2.07E-02
R-HSA-3214847	HATs acetylate histones	3.25	2.08E-02
R-HSA-3247509	Chromatin modifying enzymes	3.17	2.57E-02
R-HSA-216083	Integrin cell surface interactions	3.14	3.32E-02
R-HSA-912446	Meiotic recombination	3.13	3.29E-02
R-HSA-1221632	Meiotic synapsis	3.13	3.29E-02
R-HSA-1638091	Heparan sulfate/heparin (HS-GAG) metabolism	3.06	4.16E-02
R-HSA-5250941	Negative epigenetic regulation of rRNA expression	3.05	3.78E-02
R-HSA-157579	Telomere Maintenance	3.04	3.83E-02
R-HSA-9018519	Estrogen-dependent gene expression	3.01	4.07E-02
R-HSA-211000	Gene Silencing by RNA	3.00	4.09E-02
R-HSA-9716542	Signaling by Rho GTPases, Miro GTPases and RHOBTB3	2.97	4.14E-02
R-HSA-3781865	Diseases of glycosylation	2.96	4.37E-02
R-HSA-73886	Chromosome Maintenance	2.91	4.97E-02
R-HSA-71387	Metabolism of carbohydrates	2.90	4.97E-02
R-HSA-927802	Nonsense-Mediated Decay (NMD)	-3.05	4.73E-02
R-HSA-9707564	Cytoprotection by HMOX1	-3.09	4.08E-02
R-HSA-983169	Class I MHC mediated antigen processing & presentation	-3.11	3.85E-02
R-HSA-71291	Metabolism of amino acids and derivatives	-3.11	3.85E-02
R-HSA-69615	G1/S DNA Damage Checkpoints	-3.14	3.85E-02
R-HSA-9020702	Interleukin-1 signaling	-3.15	3.85E-02
R-HSA-187577	SCF(Skp2)-mediated degradation of p27/p21	-3.15	3.85E-02
R-HSA-8948751	Regulation of PTEN stability and activity	-3.16	3.85E-02
R-HSA-983705	Signaling by the B Cell Receptor (BCR)	-3.17	3.85E-02

R-HSA-166658	Complement cascade	-3.19	3.96E-02
R-HSA-5607764	CLEC7A (Dectin-1) signaling	-3.21	3.58E-02
R-HSA-1168372	Downstream signaling events of B Cell Receptor (BCR)	-3.21	3.58E-02
R-HSA-8939902	Regulation of RUNX2 expression and activity	-3.24	3.58E-02
R-HSA-9013694	Signaling by NOTCH4	-3.27	3.39E-02
R-HSA-5358346	Hedgehog ligand biogenesis	-3.28	3.39E-02
R-HSA-2454202	Fc epsilon receptor (FCERI) signaling	-3.29	3.23E-02
R-HSA-5668541	TNFR2 non-canonical NF-kB pathway	-3.35	2.87E-02
R-HSA-174577	Activation of C3 and C5	-3.41	3.58E-02
R-HSA-162909	Host Interactions of HIV factors	-3.42	2.29E-02
R-HSA-9707587	Regulation of HMOX1 expression and activity	-3.43	2.29E-02
R-HSA-382556	ABC-family proteins mediated transport	-3.48	2.08E-02
R-HSA-351202	Metabolism of polyamines	-3.49	2.13E-02
R-HSA-5619084	ABC transporter disorders	-3.54	1.87E-02
R-HSA-9604323	Negative regulation of NOTCH4 signaling	-3.55	1.87E-02
R-HSA-202403	TCR signaling	-3.56	1.87E-02
R-HSA-1236978	Cross-presentation of soluble exogenous antigens (endosomes)	-3.59	1.87E-02
R-HSA-8941858	Regulation of RUNX3 expression and activity	-3.60	1.87E-02
R-HSA-877300	Interferon gamma signaling	-3.60	1.87E-02
R-HSA-1169410	Antiviral mechanism by IFN-stimulated genes	-3.60	1.87E-02
R-HSA-2871837	FCERI mediated NF-kB activation	-3.61	1.87E-02
R-HSA-4641258	Degradation of DVL	-3.64	1.87E-02
R-HSA-4641257	Degradation of AXIN	-3.65	1.87E-02
R-HSA-5658442	Regulation of RAS by GAPs	-3.66	1.87E-02
R-HSA-5678895	Defective CFTR causes cystic fibrosis	-3.66	1.87E-02
R-HSA-5607761	Dectin-1 mediated noncanonical NF-kB signaling	-3.69	1.87E-02
R-HSA-376176	Signaling by ROBO receptors	-3.86	1.49E-02
R-HSA-5610780	Degradation of GLI1 by the proteasome	-3.87	1.62E-02
R-HSA-69541	Stabilization of p53	-3.94	1.49E-02
R-HSA-1236975	Antigen processing-Cross presentation	-4.43	2.08E-03
R-HSA-1280215	Cytokine Signaling in Immune system	-4.66	6.78E-04
R-HSA-9010553	Regulation of expression of SLITs and ROBOs	-4.78	6.78E-04
R-HSA-909733	Interferon alpha/beta signaling	-5.75	1.67E-05
R-HSA-913531	Interferon Signaling	-6.23	8.79E-07
R-HSA-173736	Alternative complement activation	-6.24	1.87E-02

[159]

Appendix G: Aquaporin-9 immunostaining of chondrogenic pellet micromasses with and without over-expression of miR-181a/b-1 cluster.

CPC cartilage progenitor cell, NT non-transduced, LV-NS transduced with a lentivirus containing a non-silencing sequence, LV-181 transduced with a lentivirus containing the sequence for pre-miR-181a/b-1. Scale bar: 1 mm.